

TERRESTRIAL GAMMA-RAY FLASH
PRODUCTION BY LIGHTNING

A DISSERTATION
SUBMITTED TO THE DEPARTMENT OF PHYSICS
AND THE COMMITTEE ON GRADUATE STUDIES
OF STANFORD UNIVERSITY
IN PARTIAL FULFILLMENT OF THE REQUIREMENTS
FOR THE DEGREE OF
DOCTOR OF PHILOSOPHY

Brant E. Carlson

October 2009

© Copyright by Brant E. Carlson 2010

All Rights Reserved

I certify that I have read this dissertation and that, in my opinion, it is fully adequate in scope and quality as a dissertation for the degree of Doctor of Philosophy.

(Umran S. Inan) Principal Adviser

I certify that I have read this dissertation and that, in my opinion, it is fully adequate in scope and quality as a dissertation for the degree of Doctor of Philosophy.

(Peter F. Michelson) Co-Adviser

I certify that I have read this dissertation and that, in my opinion, it is fully adequate in scope and quality as a dissertation for the degree of Doctor of Philosophy.

(Elliott D. Bloom)

I certify that I have read this dissertation and that, in my opinion, it is fully adequate in scope and quality as a dissertation for the degree of Doctor of Philosophy.

(Nikolai G. Lehtinen)

Approved for the University Committee on Graduate Studies.

Abstract

Terrestrial gamma-ray flashes (TGFs) are brief flashes of gamma-rays originating in the Earth's atmosphere and observed by satellites. First observed in 1994 by the Burst And Transient Source Experiment on board the Compton Gamma-Ray Observatory, TGFs consist of one or more ~ 1 ms pulses of gamma-rays with a total fluence of $\sim 1/\text{cm}^2$, typically observed when the satellite is near active thunderstorms. TGFs have subsequently been observed by other satellites to have a very hard spectrum (harder than $dN/d\mathcal{E} \propto 1/\mathcal{E}$) that extends from below 25 keV to above 20 MeV. When good lightning data exists, TGFs are closely associated with measurable lightning discharge. Such discharges are typically observed to occur within 300 km of the sub-satellite point and within several milliseconds of the TGF observation. The production of these intense energetic bursts of photons is the puzzle addressed herein.

The presence of high-energy photons implies a source of bremsstrahlung, while bremsstrahlung implies a source of energetic electrons. As TGFs are associated with lightning, fields produced by lightning are naturally suggested to accelerate these electrons. Initial ideas about TGF production involved electric fields high above thunderstorms as suggested by upper atmospheric lightning research and the extreme energies required for lower-altitude sources. These fields, produced either quasi-statically by charges in the cloud and ionosphere or dynamically by radiation from lightning

strokes, can indeed drive TGF production, but the requirements on the source lightning are too extreme and therefore not common enough to account for all existing observations.

In this work, studies of satellite data, the physics of energetic electron and photon production, and consideration of lightning physics motivate a new mechanism for TGF production by lightning current pulses. This mechanism is then developed and used to make testable predictions.

TGF data from satellite observations are compared to the results of Monte Carlo simulations of the physics of energetic photon production and propagation in air. These comparisons are used to constrain the TGF source altitude, energy, and directional distribution, and indicate a broadly-beamed low-altitude source inconsistent with production far above thunderstorms as previously suggested.

The details of energetic electron production by electric fields in air are then examined. In particular, the source of initial high-energy electrons that are accelerated and undergo avalanche multiplication to produce bremsstrahlung is studied and the properties of these initial seed particles as produced by cosmic rays are determined. The number of seed particles available indicates either extremely large amplification of the number of seed particles or an alternate source of seeds.

The low-altitude photon source and alternate source of seed particles required by these studies suggest a production mechanism closely-associated with lightning. A survey of lightning physics in the context of TGF emission indicates that current pulses along lightning channels may trigger TGF production by both producing strong electric fields and a large population of candidate seed electrons. The constraints on lightning physics, thunderstorm physics, and TGF physics all allow production by this mechanism.

A computational model of this mechanism is then presented on the basis of a

method of moments simulation of charge and current on a lightning channel. Calculation of the nearby electric fields then drives Monte Carlo simulations of energetic electron dynamics which determine the properties of the resulting bremsstrahlung. The results of this model compare quite well with satellite observations of TGFs subject to requirements on the ambient electric field and the current pulse magnitude and duration. The model makes quantitative predictions about the TGF source altitude, directional distribution, and lightning association that are in overall agreement with existing TGF observations and may be tested in more detail in future experiments.

Acknowledgments

Despite the Hollywood image of the mad scientist, science is not a solitary process; this dissertation would never have been possible without the help of many people. First, I wish to thank my principle adviser, Umran Inan for not only agreeing to take me on as a student with little more than an emailed request, but also for never wavering in his support of his students. Secondly, I must thank Nikolai Lehtinen, for careful guidance on everything from getting his programs to run to managing summer research students.

I also wish to thank Peter Michelson, my co-advisor in the physics department, who was always able to help and provide useful advice and guidance. Thanks also to Elliott Bloom for helping greatly with other data analysis projects and for serving on my reading committee. I must also thank Parviz Moin for serving as the chair of my oral examination committee on very short notice, and Martin Walt for help editing this dissertation.

Thanks are also due for my current and former office- and lab-mates who kept my spirits up for the past four years. Forrest Foust, Robert Newsome, Dan Golden, Morris Cohen, Kevin Graf, Ryan Said, Bob Marshall, Marek Gołkowski, Nader Moussa, Ben Cotts, Andrew Gibby, Denys Piddyachiy, Sheila Bijour, Naoshin Haque, George Jin, Rob Moore, and all the rest, it's been fun.

I must also especially thank Shaolan Min and Helen Niu for keeping STAR Lab running, making sure I got paid on time, and for never turning me away, no matter

how odd or ill-timed my request may have been.

Nikolai Østgaard, Thomas Gjesteland, David Smith, Brian Grefenstette, Bryna Hazelton, and Joe Dwyer also deserve thanks for very useful discussions at conferences and meetings over the years.

Finally, I want to thank my parents for supporting me in all my endeavors, from building a kayak to going off to grad school, even putting up with less than monthly email contact along the way. I have no idea how I got away with that. I am also very grateful to my good friend Qinzi Ji for being there throughout the trials and tribulations of grad school.

Many thanks!

Brant Carlson

October 26, 2009

This work was supported in part by the Stanford Benchmark Fellowship program and National Science Foundation grant ATM-0535461.

Contents

Abstract	iv
Acknowledgments	vii
1 Introduction	1
1.1 History of terrestrial gamma-ray flashes	2
1.2 Terrestrial gamma-ray flash observations	4
1.3 Motivation	13
1.4 Contributions	14
2 Theoretical background	16
2.1 Energetic particle dynamics	17
2.2 Electric field effects	26
2.3 Spark physics	32
2.4 TGF production theories	42
3 Constraints on source mechanisms	50
3.1 Monte Carlo simulations	51
3.2 Satellite data comparison	55
3.3 Caveats	60
3.4 Summary of TGF source properties	61

4	Electron avalanche seeding	62
4.1	Cosmic rays	62
4.2	Runaway relativistic electron avalanche seeding efficiency	69
4.3	Overall seed population	72
4.4	Implications	73
5	Lightning and TGF production	76
5.1	Leaders as a RREA seed source	78
5.2	Leaders as an electric field source	79
5.3	TGF production by lightning current pulses	82
5.4	Lightning current pulse mechanism predictions	86
5.5	Comparison to relativistic feedback TGF production	90
5.6	Summary	95
6	Lightning TGF production model	96
6.1	Lightning electric field model	97
6.2	RREA in realistic lightning electric fields	106
6.3	TGF production requirements	109
7	Conclusions	115
7.1	Suggestions for future work	116

List of Tables

2.1	Discharge process parameters	43
5.1	Typical lightning process timescales	85

List of Figures

1.1	A schematic of the Compton Gamma-Ray Observatory	4
1.2	Sample BATSE TGFs	5
1.3	RHESSI TGF and LIS lightning map	9
1.4	Average RHESSI TGF spectra	10
2.1	Photon interaction cross sections in nitrogen	17
2.2	Feynman diagrams of pair production and bremsstrahlung	20
2.3	Friction on electrons in air at sea level	21
2.4	Positive streamer discharge growth	34
2.5	Atmospheric density vs. altitude	35
2.6	Typical thunderstorm charges and discharges	36
2.7	Leader extension process	38
2.8	Lightning and return stroke voltage	39
2.9	Outline of TGF physics	44
2.10	Quasi-electrostatic TGF production mechanism	46
2.11	Electromagnetic pulse geometry	47
2.12	Electromagnetic pulse TGF production mechanism	48
3.1	Lehtinen Monte Carlo validation	53
3.2	Simulated and observed spectra	56
3.3	Source energy requirements	58

3.4	Simulated lateral extent of TGF emissions	59
4.1	Sample cosmic ray air shower	64
4.2	Sample air shower secondary distributions	65
4.3	Sample overall secondary distributions in region of interest	69
4.4	Sample RREA seed production	71
4.5	Seeding efficiency	72
4.6	Effective seed flux	73
5.1	Line charge radius limits	81
5.2	RREA growth factor in a limited line charge field	82
5.3	Lightning and TGF electric field and voltage constraints	84
5.4	Relativistic feedback constraints	91
5.5	Relativistic feedback in limited line-charge fields	93
5.6	Photon feedback and charge polarity	94
6.1	Method of moments discretization scheme	101
6.2	Current pulse simulation for straight antenna	104
6.3	Current pulse simulation comparison to NEC2, TWTD	104
6.4	Realistic lightning channel simulation	106
6.5	Electric field intensification	107
6.6	Directional distribution of emissions from current pulse model	108
6.7	Photon energy spectra intensification from current pulse model	109
6.8	Charge density on a conducting wire in an electric field	111
6.9	Channel current and resulting charge enhancement	111

Chapter 1

Introduction

This dissertation examines the production of brief bursts of energetic photons by lightning, the so-called terrestrial gamma-ray flashes. Terrestrial gamma-ray flashes (TGFs) are observed by satellites to typically last less than a millisecond and can have photons with energies exceeding 20 MeV (*Fishman et al.*, 1994b; *Smith et al.*, 2005). The process by which lightning produces such intense bursts of photons with such high energies is a puzzle that stretches existing ideas about the physics of thunderstorms and lightning. Though such extreme physics was first suggested by *Wilson* (1924) over 80 years ago, our understanding of such processes and their causes and effects in the thunderstorm environment are still open questions.

This dissertation describes the history of TGF observations, places these observations in context, and describes existing understanding of TGF physics and its limitations. The contributions of this dissertation to the field are then given. Specifically, this dissertation constrains the TGF photon source, determines the properties of the seed particles which initiate of TGFs, suggests and models a new mechanism of lightning-driven TGF production, and gives the results of the model, inviting experimental study. These studies continue a line of theoretical and experimental research dating back to the early twentieth century.

1.1 History of terrestrial gamma-ray flashes

In 1924, C. T. R. Wilson,¹ predicted an interesting phenomenon on the basis of the behavior of energetic electrons in electric fields. Because more energetic electrons experience lower frictional forces and electric fields may produce forces that exceed the frictional force, an energetic electron in a thunderstorm may encounter such a field and would consequently be accelerated to great energies and produce radiation (*Wilson*, 1924). This prediction was the first hint that energetic physics could play a role in thunderstorms. Wilson further noted that the minimum electric field strength to induce sparking decreases more rapidly above a thundercloud than the electric field of the thundercloud. Consequently, an electric field too small to induce sparking just above the cloud may still induce sparking high above the cloud. This possibility of high-altitude discharge preceded the formal discovery of such discharges, now called “sprites,” by over 60 years (*Franz et al.*, 1990). The discovery of radiation produced by energetic electrons in thunderclouds would have to wait slightly longer and required a little luck.

At the height of the Cold War in the early 1960s, atmospheric nuclear bomb testing was finally being phased out in favor of underground nuclear tests because such tests are relatively free of radioactive fallout. In this context, the partial test ban treaty was signed in 1963, prohibiting atmospheric and space-based nuclear detonations. As part of an effort to monitor such nuclear tests, both to monitor compliance with the partial test ban treaty and to confirm that the Soviet Union was not gaining a lead in the Cold War arms race, the United States launched the Vela constellation of satellites. The Vela satellites contained instruments to detect the effects of nuclear detonations (bursts of neutrons, gamma-rays, x-rays, visible light, and radio waves) and were placed in unusual high-altitude orbits from which they would even be able

¹Best known as the inventor of the cloud chamber, for which he received the Nobel Prize in 1927.

to detect nuclear tests on the far side of the Moon. Though the satellites did not detect any nuclear tests,² they did detect bursts of gamma-rays originating outside the solar system. These observations are now recognized as the discovery of cosmic gamma-ray bursts, first published by *Klebesadel et al.* (1973).

These cosmic gamma-ray bursts, being some of the most energetic explosions in the entire universe, then became the subject of intense study. Though a wide range of behaviors are observed, a typical gamma-ray burst lasts a few seconds and in those seconds releases more energy than a typical star in its entire lifetime. Many theories have been developed to explain these intense bursts, ranging from the collapse of massive stars to star-quakes on highly-magnetized neutron stars (magnetars). A review can be found in *Fishman and Meegan* (1995).

Other satellites were launched to study cosmic gamma-ray bursts, including the Compton Gamma-ray Observatory (CGRO) in 1991, shown in Figure 1.1. One of the instruments on CGRO, specialized to study cosmic gamma-ray bursts, was the Burst and Transient Source Experiment (BATSE, see *Fishman et al.*, 1994a).

BATSE consisted primarily of eight scintillator panels, each with effective area $\sim 2000 \text{ cm}^2$, sensitive to energies from 25 keV to above 1 MeV, mounted on the corners of CGRO facing outward as on the corners of a cube. As such, BATSE could determine the approximate direction toward the source of a gamma-ray burst by comparison of radiation levels at different detectors. BATSE was a wonderful success, detecting hundreds of cosmic gamma-ray bursts per year and mapping their locations on the sky (*Fishman et al.*, 1994a).

It came as a surprise, however, when anomalous bursts of radiation were observed only by detectors facing the Earth. These bursts were much shorter than the typical gamma-ray burst, and were observed roughly monthly, too frequently to ignore.

²The possible exception is the “Vela incident” where a characteristic flash of light was observed over the South Atlantic (*Ruina et al.*, 1980).

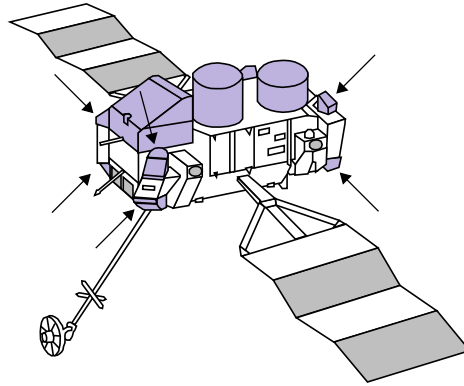


Figure 1.1: **A schematic of the Compton Gamma-Ray Observatory.** The Burst And Transient Source Experiment (BATSE) modules are mounted near the corners of the main body of the spacecraft. The six visible modules of eight are indicated with arrows. Figure credit: NASA, GSFC, P.J.T. Leonard.

These observations are now recognized as the discovery of a new class of phenomena known as terrestrial gamma-ray flashes (TGFs, *Fishman et al.*, 1994b). Though unexpected, these bursts of energetic radiation appeared to be the confirmation of Wilson’s predictions 70 years earlier that energetic radiation would be emitted above thunderstorms. Despite the prescience of Wilson’s basic predictions, the physical picture of TGFs as short bursts of energetic photons was incomplete and required further study.

1.2 Terrestrial gamma-ray flash observations

1.2.1 BATSE TGF observations

BATSE’s large detectors, limited storage space and limited telemetry bandwidth required a triggering scheme to limit data collection to just the most interesting events. As such, the BATSE data focuses on events with intensities far above the background noise. Such events would trigger the data acquisition system which would then store

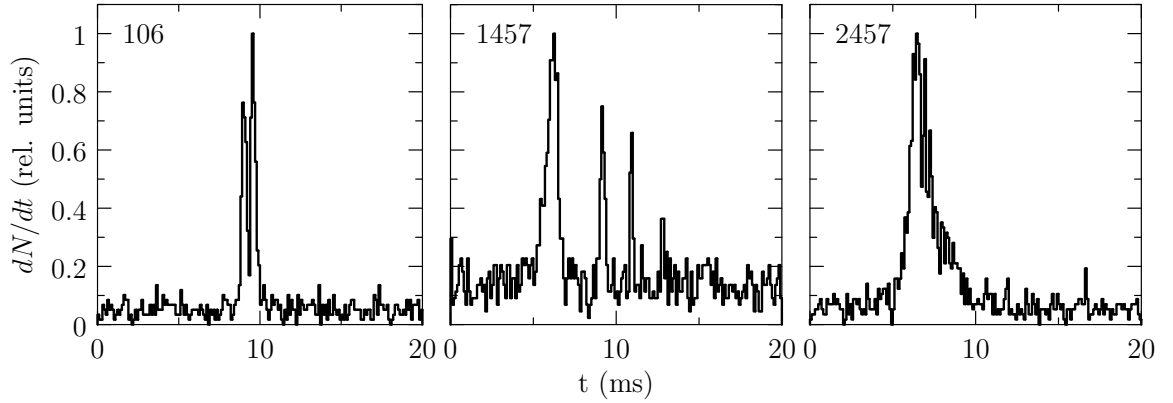


Figure 1.2: **Sample BATSE TGFs.** The y axis represents count rate of 25–1000 keV photons, while the x axis is time in milliseconds. The trigger number from the BATSE catalog is shown in the upper left. Data from the Compton Observatory Science Support Center (COSSC) data archive at <http://cosscc.gsfc.nasa.gov>.

every photon detected by the instrument as an arrival time and an energy in one of four energy bins (25–50, 50–100, 100–300, and >300 keV with sensitivity decreasing above 1 MeV). BATSE data thus shows TGFs as short bursts of up to 1000 photons with energies ranging from 25 keV up to above 1 MeV. BATSE observed 76 TGFs over its 9-year lifetime.³

Several BATSE TGFs are shown in Figure 1.2. Even in just three events, a wide range of behavior can be seen, with bursts ranging from less than one to greater than five milliseconds. The observed fluence ranges from 0.1–0.5 photons/cm². Typically, a single pulse is seen, but groups of seven or more pulses separated by a few milliseconds have also been observed.

This wide range of behavior is difficult to explain with any one physical mechanism. Any postulated source mechanism must be able to explain both bursts less than 1 ms and bursts longer than 8 ms. The question of how multiple pulses may be produced in a short time is also a puzzle.

³A complete list of BATSE TGF observations can be found at <http://www.batse.msfc.nasa.gov/batse/tgf/>.

Though the initial BATSE TGF data provide little more than a picture of TGFs as rare, short, and atmospheric, several useful inferences can be made. Analysis of the shape of the light curves shows that the minimum variability timescale associated with the emissions requires a source region smaller than 7 km to account for the rapid variations in intensity in some especially short-duration cases (*Nemiroff et al.*, 1997). The BATSE data also shows significant numbers of photons with energy < 50 keV. As photons with energy < 50 keV are heavily attenuated in air, these photons must come from at least 30 km altitude, suggesting a high-altitude source (*Fishman et al.*, 1994b). Though the four channel spectral information in the BATSE data is crude, the spectra recorded are consistent with photons produced by energetic electrons, leading *Fishman et al.* (1994b) to suggest production associated with high-altitude lightning.

1.2.2 BATSE TGFs and coincident lightning observations

The suggestion that lightning may be associated with TGFs was subsequently supported by lightning observations. As discussed in Section 2.3.4, cloud-to-ground lightning activity emits radio waves primarily in the very low frequency (VLF) band from 3 to 30 kHz (*Rakov and Uman*, 2003, p. 443). These signals propagate very efficiently in a waveguide formed between the Earth and the conducting upper atmosphere (the ionosphere), and can be detected thousands of kilometers from the source lightning. The direction from receiver to source and the relative arrival time of the signal at multiple receivers can be used to determine the location of the source lightning. Examination of radio recordings taken during time periods when TGFs were observed therefore provides a way to examine cloud-to-ground lightning activity possibly associated with TGF production. *Inan et al.* (1996) made such observations and found active thunderstorm systems near CGRO for two TGFs. In one case, a radio signal from lightning (a radio atmospheric or “sferic”) was observed within ± 1.5 ms of the

TGF observed by BATSE.

Later analysis of BATSE TGFs with coincident radio data available solidified the association between TGFs and lightning (*Cohen et al.*, 2006). Specifically, coincident lightning was clearly detected in three of six cases. There are even cases where TGFs with multiple bursts of photons are observed coincident with multiple bursts of radio activity, though multiple bursts of radio activity are also observed coincident with lone gamma-ray pulses. Though no coincident lightning activity was detected in the remaining cases, active thunderstorms were present.

Unfortunately, not all lightning efficiently produces sferics that are detectable at long distances. Intra-cloud lightning, accounting for roughly of 90% of all lightning, may not radiate significant VLF to long distances (see Section 2.3.4). Therefore the lack of coincident lightning in some cases may suggest a source involving lightning that does not efficiently radiate sferics to long distances, though a photon production mechanism that does not require close association with lightning is also possible.

1.2.3 RHESSI TGF observations

TGF science took a major leap forward in 2005 when it was announced that the Reuven Ramaty High-Energy Solar Spectroscopy Imager (RHESSI) spacecraft had also observed TGFs (*Smith et al.*, 2005). The RHESSI spacecraft is a spin-stabilized small explorer⁴ designed to detect x-rays and gamma-rays from the sun. Its main instrument for TGF observations is a set of germanium solid-state detectors housed in the tail of the spacecraft. Though these detectors are intended to look only in one direction along the main axis of the spacecraft, the large sensitive volume of the detectors in an otherwise small spacecraft allows RHESSI to also detect energetic photons entering the detector from the back and sides. The average effective area

⁴The NASA Small Explorer program funds small satellites for focused science missions with relatively low budgets less than \$120 million.

for such detection of photons with energies above 50 keV is $\sim 242 \text{ cm}^2$ (*Smith, 2006*). Unlike BATSE, all photons detected are stored and transmitted to ground without need for a trigger.

RHESSI provides a novel view of TGFs. Without the requirement of a trigger, RHESSI collects a large data set to be mined for TGFs. RHESSI is thus found to observe TGFs much more frequently than BATSE, detecting one every several days, compared with BATSE observations of approximately one per month.⁵ RHESSI also collects higher resolution photon energy information than the four-channel spectra produced by BATSE. RHESSI does not provide directional information, only identifying TGFs on the basis of duration; 1 ms TGFs are much shorter than typical gamma-ray bursts. Though gamma-ray bursts are occasionally as short as 1 ms (see for instance Figure 1 of *Lee et al. (2000)*) and RHESSI does occasionally trigger on short pulses from soft gamma-ray repeaters, such events as identified by other satellites are removed from the set of TGFs (*Smith, 2009*). RHESSI also has a much smaller effective area than BATSE so it does not collect as many photons, typically < 100 photons per TGF. Such small numbers of photons limit analysis of RHESSI spectra to averages over many TGFs.

The greater frequency of RHESSI TGF observations requires a global frequency of at least 50 /day given the optimistic assumption that TGFs are detectable if produced less than 1000 km from the subsatellite point (*Smith et al., 2005*). The more realistic assumption that TGFs are only detectable if produced less than 300 km from the subsatellite point gives a global frequency of approximately 500 /day. Compared to the global lightning frequency of ~ 40 /second, it can therefore be estimated that 1 in approximately 10^4 lightning discharges produces a TGF. The better statistics also allow for studies of the geographic distribution of TGFs, shown in the upper panel of Figure 1.3. TGFs nicely cluster in regions of the globe with high lightning activity

⁵RHESSI's detection efficiency has unfortunately decreased since 2006 due to radiation damage.

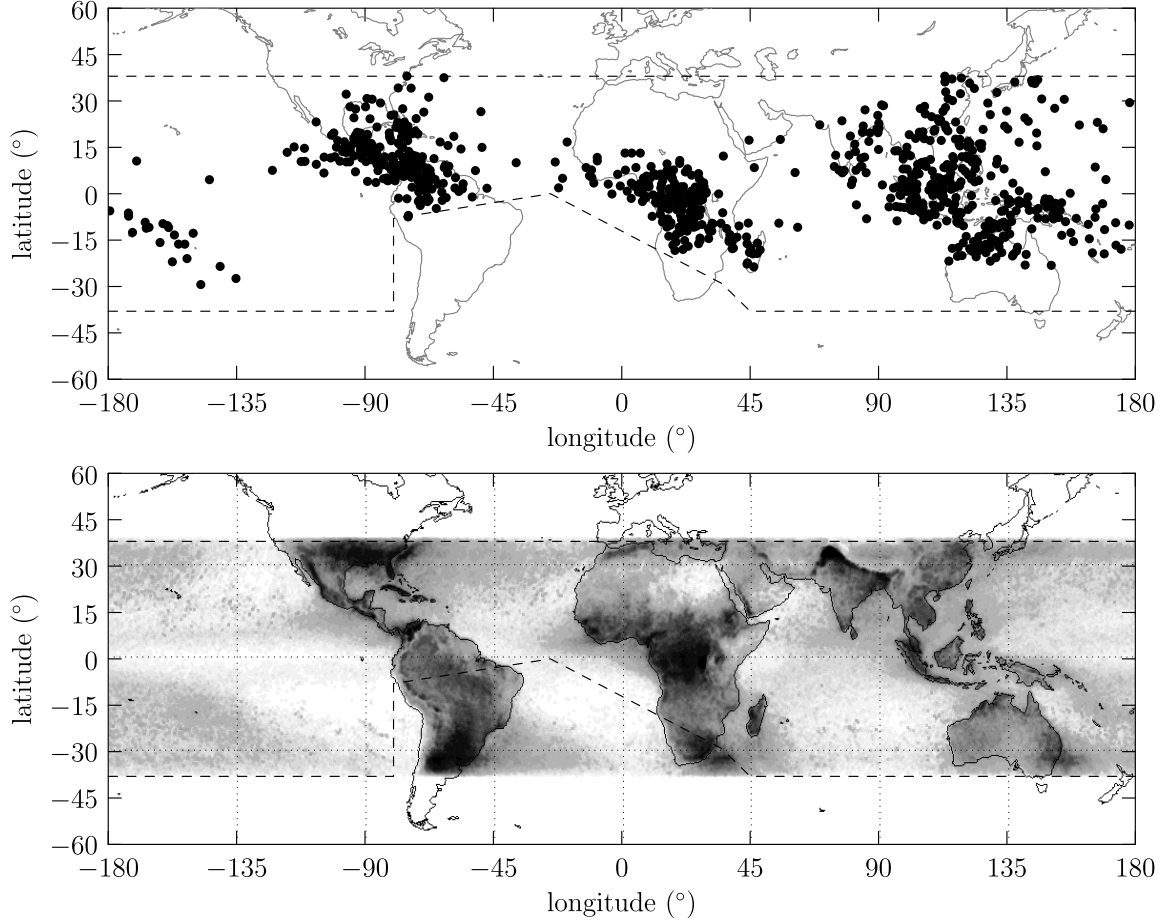


Figure 1.3: **RHESSI TGF and LIS lightning map.** Upper panel: map showing the location of the RHESSI satellite when TGFs were observed. The dashed lines indicate the typical regions of coverage limited by the 38° orbital inclination and the radiation conditions in the South Atlantic Anomaly. Lower panel: global lightning distribution as seen by the Lightning Imaging Sensor. Darker colors indicate higher flash density. Clusters of TGFs are seen in regions of high lightning activity: Central and South America, Central Africa, Southeast Asia, and Oceania. Data courtesy of D. Smith taken from the RHESSI TGF data archive at http://scipp.ucsc.edu/~dsmith/tgflib_public/ and the Lightning Imaging Sensor data server at <http://thunder.msfc.nasa.gov/data/>.

as seen by the Lightning Imaging Sensor (*Christian et al.*, 1999), shown in the lower panel of Figure 1.3.

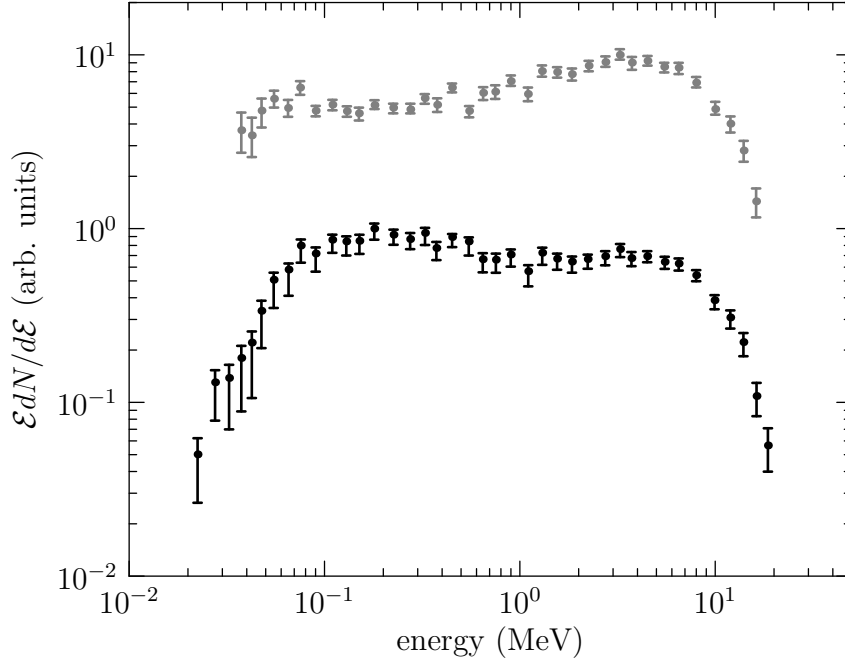


Figure 1.4: **Average RHESSI TGF spectra.** The lower black points show the spectrum of measured photon energy as detected by RHESSI, plotted as $\mathcal{E}dN/d\mathcal{E}$. Note that this data set is the spectrum of counts observed by the satellite. An estimate of the true photon spectrum assuming a $dN/d\mathcal{E} \propto 1/\mathcal{E}$ is shown above in grey and shows slight differences as the detector response matrix is not perfect. In both curves, the decrease at low energies is due to atmospheric absorption and a decrease in detection efficiency, while the decrease at high energies is largely due to a natural cutoff in the spectrum (See Chapter 3). Data for both curves taken from *Smith et al.* (2005).

The average TGF photon spectrum measured with RHESSI is shown in Figure 1.4. One startling result from this energy spectrum is that it continues up to 20 MeV. It is surprising that such high-energy photons can be produced in such great numbers in TGFs. Such a hard spectrum can only be produced by bremsstrahlung, a fact discussed further in Section 2.1.2.

1.2.4 RHESSI TGFs and coincident lightning observations

Lightning associated with RHESSI TGFs has been studied very successfully due to the large number of TGFs detected. Extension of the studies of *Inan et al.* (1996) and *Cohen et al.* (2006) to RHESSI TGFs for which lightning data is available show coincident lightning activity within several milliseconds for 76% of TGFs, much higher than the $\sim 2\%$ expected by random chance (*Inan et al.*, 2006). The coincident radio signals detected in *Inan et al.* (2006) indicate that the associated lightning discharge often has unusually high peak current, especially for TGFs observed over the ocean, but the association is not perfect. This result suggests relatively intense discharges, though a complete picture of lightning activity is not provided by distant VLF measurements. In particular, the role of intra-cloud discharges is not resolved and may be relevant to TGF production. Though the timing of coincident lightning relative to satellite observation is difficult to determine due to timing uncertainty in the RHESSI spacecraft, the relative timing is consistent with geometric effects and measurement error provided that an additional 2 ms variance is allowed for other effects. Further analysis involving accurate geolocations of lightning associated with 34 TGFs (described in *Cohen et al.*, 2009) indicates that the distance between lightning and the subsatellite point is typically < 300 km, consistent with similar analyses by *Cummer et al.* (2005). The timing coincidence between TGF and associated lightning is also much closer when the geometric uncertainty can be resolved with known lightning locations. The remaining timing spread is consistent with poor timing on the RHESSI satellite and the additional 2 ms variance mentioned above. Note that the additional 2 ms variance observed between the time of TGF production and the time of sferic emission does not result from measurement error, and thus implies some displacement in time and/or space between the sferic and TGF sources.

Some light was shed on the question of the specific lightning processes possibly associated with TGFs by *Stanley et al.* (2006). Though their sample of 6 geolocated

lightning discharges associated with TGFs is smaller and therefore less useful than those described in *Cohen et al.* (2009), the radio signals received for two of the cases reported by *Stanley et al.* (2006) came from lightning that was close enough to their receiver and rapid enough to show ionospheric reflections. In such cases, the relative timing of the direct and reflected signals can be used to infer the altitude of the source of the radio signal. The altitudes were measured to be 13.6 km and 11.5 km. These altitudes are too high to be produced by cloud-to-ground lightning, strongly suggesting that these two cases were associated with intra-cloud discharge.

1.2.5 Summary of TGF observations

These satellite observations of TGFs and analysis of coincident lightning activity seen in radio observations provide a reasonably clear picture of the phenomenon of terrestrial gamma-ray flashes. TGFs as observed on satellites are short, ranging from less than one to several milliseconds with one or more pulses observed separated by a few milliseconds. The photons themselves have a very hard spectrum with a maximum energy at or above 20 MeV, strongly suggesting a bremsstrahlung source. The overall fluence observed is approximately 1 photon/cm². Radio observations coincident with satellite TGF detections typically show lightning activity within several milliseconds. When the lightning activity can be geolocated, it is typically less than 300 km from the subsatellite point. Not all TGFs are associated with detectable VLF radio activity, which together with the observations of source heights above 10 km by *Stanley et al.* (2006) suggests intra-cloud lightning as the source of some TGFs. Closer scrutiny of the radio emissions associated with TGFs shows a slight tendency toward discharges with high peak current (*Inan et al.*, 2006).

1.3 Motivation

TGFs have attracted a great deal of attention since their discovery. This attention stems from the novelty of the subject and the implications of energetic processes for such common phenomena as thunderstorms and lightning.

The presence of 20 MeV photons in a TGF is quite remarkable. Such energetic photons cannot be produced by radioactive decay, and therefore require a physical process akin to a natural particle accelerator. That such a particle accelerator may exist in or above thunderstorms is a fascinating development and poses an irresistible puzzle for atmospheric physics.

Even given such a particle accelerator, the production of sufficient numbers of energetic photons to produce an observable TGF is by no means an obvious consequence. How much energy is required, and where and how that energy must be produced are also interesting questions.

The timing of TGFs also poses an interesting puzzle. If a typical TGF lasts 1 ms, the source process must also last approximately 1 ms. A typical lightning discharge, by contrast, has a total duration from initiation to quiescence of several hundred milliseconds, while the relaxation timescale for electric fields in air ranges from 0.1–10 s. TGFs must therefore be associated with very dynamic processes occurring as small portions of the lightning discharge as a whole. The precise nature of these processes and how they are associated with TGF production is an essential unanswered question that motivates TGF research.

The energetic processes that must occur in a TGF have direct implications for many processes in the Earth's atmosphere. Lightning, clearly associated with TGFs, itself is poorly-understood. Present understanding of lightning physics does not include the processes necessary for TGF production, so studies of TGF physics may help advance the understanding of lightning. The unknown mechanism of lightning

initiation, one of the main open questions in thunderstorm dynamics, may also be influenced by processes involved in TGF production. The contribution of TGFs to the atmosphere and space radiation environment and the chemical effects of energetic processes in the atmosphere are also of great interest. The possibility of addressing these open questions motivates the studies of TGFs described herein.

1.4 Contributions

This dissertation addresses several of the open questions listed above and attempts to explain relevant aspects of TGF physics. The investigations described in the subsequent chapters follow from the theory of the physics involved in TGF production as described in Chapter 2. In particular, the physics of relativistic electrons driven by electric fields in materials (i.e., air) is central to the studies described in this work. Existing theoretical mechanisms of TGF production are also discussed in Chapter 2. The fact that these theories are unable to explain TGF observations directly motivates our investigations.

The specific contributions of this dissertation are:

1. Development of constraints on properties of the TGF photon source by comparison of Monte Carlo simulation results with satellite data. These results constrain the TGF source altitude, energy, and directional distribution (Chapter 3).
2. Determination of the production and properties of energetic electrons by cosmic rays in the Earth's atmosphere and simulate the behavior of such electrons in electric fields by Monte Carlo techniques. These results set further requirements on the source of TGF photons (Chapter 4).
3. Conception and development of a new mechanism for TGF production driven

directly by lightning current pulses. This mechanism meets the requirements described by the previous two contributions, and allows construction of testable predictions (Chapter 5).

4. Modeling of the mechanism of TGF production by lightning current pulses by use of the method of moments and Monte Carlo simulations. This model is then used to derive requirements on TGF-associated lightning (Chapter 6).

This dissertation as a whole therefore provides a set of clear requirements on TGF production mechanisms, provides a mechanism that attempts to meet these requirements, and presents a model of this mechanism that determines the conditions under which it can successfully reproduce TGF observations.

Chapter 2

Theoretical background

Though terrestrial gamma-ray flashes pose an interesting puzzle, the physical phenomena involved in TGF production have been well-studied both experimentally and theoretically. A broad understanding of TGF production can be derived from the presence of 20 MeV photons. The behavior of energetic photons in a TGF as they propagate through the atmosphere is governed by three processes: photoelectric absorption, Compton scattering, and pair production. Such photons can only be produced by acceleration of energetic electrons undergoing collisions, a process known as bremsstrahlung.¹ The behavior of the energetic electrons necessary for bremsstrahlung depends on the electron energy but largely reduces to simple collisional processes. The electric field necessary to accelerate electrons to high energies allows for additional interesting phenomena which draw energy from the electric field. The electric fields come from thunderstorms and lightning, phenomena that are crucial to the production of TGFs. These processes are described in detail in this chapter.

¹“Braking radiation” in German.

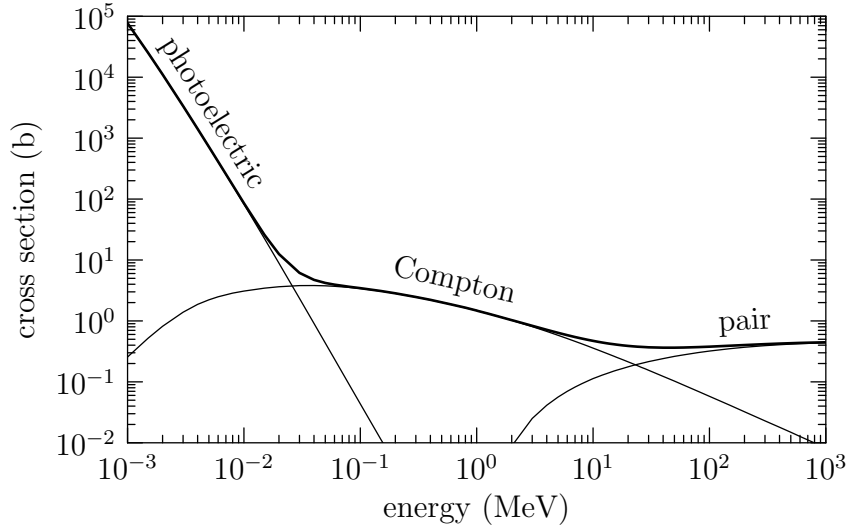


Figure 2.1: **Photon interaction cross sections in nitrogen.** Interaction cross sections in barns/atom shown for photon energies from 1 keV to 1 GeV. Bold curve represents the total cross section, narrow curves indicate photoelectric, Compton scattering, and pair production cross sections as labeled where the process in question is dominant. Data taken from *Berger et al.* (1998).

2.1 Energetic particle dynamics

2.1.1 Photon interactions

The energetic photons observed in TGFs can undergo several processes as they travel through the atmosphere: photoelectric absorption, Compton scattering, and pair production. The relative likelihood of these processes for photons in nitrogen is shown as a function of photon energy in Figure 2.1.

Photoelectric absorption occurs when a photon is absorbed by an atom, ejecting an atomic electron in the process. The electron loses energy as it escapes from its bound state and travels away with the remaining energy leaving behind an ion. The total cross section for photoelectric absorption is difficult to calculate from first principles due to the complicated structure of atomic electron wave-functions, but can be

approximated for photon energies above the binding energy of the K-shell electrons but below the electron rest energy as:

$$\sigma_{\text{photo}} = \frac{32\sqrt{2}\alpha^4 r_e^2 Z^5}{3} \left(\frac{m_e c^2}{h\nu} \right)^{7/2} \quad (2.1)$$

where α is the fine structure constant, r_e is the classical electron radius, Z is the atomic number, m_e is the electron rest mass, c is the speed of light, h is Planck's constant, and ν is the frequency of the incident photon (*Leo*, 1994, p. 54–55). As photon energy $h\nu$ increases, the cross section decreases rapidly as $(h\nu)^{-7/2}$.

As can be seen in Figure 2.1, for energies above ~ 30 keV Compton scattering becomes the dominant process for energetic photons in nitrogen.² Compton scattering occurs when an incident photon scatters off and imparts some of its energy to an electron. Both the scattered photon and the recoil electron emerge from the collision. The final energy of the photon $h\nu'$ depends on the scattering angle θ and can be calculated as a homework problem in special relativity:

$$h\nu' = \frac{h\nu}{1 + \gamma(1 - \cos \theta)} \quad (2.2)$$

where $\gamma = h\nu/m_e c^2$. This collision leaves the recoil electron with a kinetic energy T given by

$$T = h\nu - h\nu' = h\nu \frac{\gamma(1 - \cos \theta)}{1 + \gamma(1 - \cos \theta)} \quad (2.3)$$

The cross section for Compton scattering can be calculated to lowest order from elementary quantum electrodynamics and is referred to as the Klein-Nishina cross section:

$$\frac{d\sigma}{d\Omega} = \frac{r_e^2}{2} \frac{1}{[1 + \gamma(1 - \cos \theta)]^2} \left[1 + \cos^2 \theta + \frac{\gamma^2(1 - \cos \theta)^2}{1 + \gamma(1 - \cos \theta)^2} \right] \quad (2.4)$$

²Note the very strong Z dependence in Equation 2.1 Elements with higher atomic number have much greater photoelectric absorption cross sections and therefore Compton scattering only becomes important for relatively larger energies.

where the cross section is given as a differential in solid angle Ω . For a detailed derivation, see *Peskin and Schroeder* (1995, pp 158–167). The total cross section can be obtained by integrating over solid angle to yield

$$\sigma_c = 2\pi r_e^2 \left\{ \frac{1+\gamma}{\gamma^2} \left[\frac{2(1+\gamma)}{1+2\gamma} - \frac{\ln(1+2\gamma)}{\gamma} \right] + \frac{\ln(1+2\gamma)}{2\gamma} - \frac{1+3\gamma}{(1+2\gamma)^2} \right\} \quad (2.5)$$

For large photon energy, the terms in Equation 2.5 have roughly $1/\gamma$ dependence, leading the Compton scattering cross section to drop off at relativistic energies.

Pair production is the remaining relevant process for energetic photons. In pair production, an incident photon with energy $h\nu > 2m_e c^2 = 1.022 \text{ MeV}$ produces a positron and an electron through interaction with a particle, typically an atomic nucleus. A Feynman diagram of pair production is shown at left in Figure 2.2. The positron and electron split the remaining energy of the photon.

Pair production cross sections can be calculated from quantum electrodynamics in various approximations. In particular, as pair production most often happens in the field of an atomic nucleus, the screening of the nuclear field by atomic electrons affects the calculation. Some simplifications are possible if the incident photon energy falls in a certain range, e.g., $h\nu \gg m_e c^2$. The resulting formulas for differential cross sections are quite complicated and often must be treated numerically. A detailed review is given in *Motz et al.* (1969). For the approximate complete screening case where $h\nu \gg 137m_e c^2 Z^{-1/3}$, the total pair production cross section is

$$\sigma_{\text{pair}} \simeq 4Z^2 \alpha r_e^2 \left\{ \frac{7}{9} [\ln(183Z^{-1/3}) - f(Z)] - \frac{1}{54} \right\} \quad (2.6)$$

where $f(Z)$ is a correction factor due to Coulomb interaction of the produced particles with the nucleus (*Leo*, 1994, p. 39).

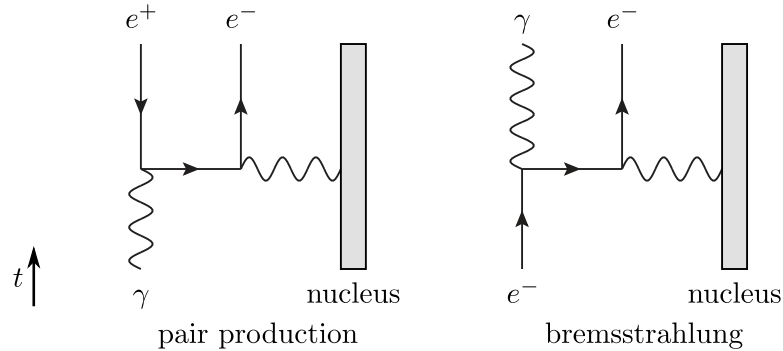


Figure 2.2: **Feynman diagrams of pair production and bremsstrahlung.** Sample low-order Feynman diagrams are shown for pair production and bremsstrahlung as indicated. Other diagrams are also possible. Time increases in the vertical direction. Note that pair production and bremsstrahlung differ only by exchange of the left-most photon and electron.

2.1.2 Electron interactions

The photons in a TGF must be produced by energetic electrons. Other than energetic nuclear transitions, energetic electron bremsstrahlung is the only feasible way to produce energetic photons in the Earth’s atmosphere.³

These energetic electron interactions display a wide variety of behavior. One way to represent the net effect of these interactions is to consider the frictional force experienced by an energetic electron. This frictional force is shown as a function of electron energy in Figure 2.3. Though the fundamental mechanism behind these energy loss processes is electron-electron and electron-nucleus collisions, the behavior changes as a function of energy. At the highest energies, radiation produced by charge accelerations in electron-nucleus collisions dominate the energy loss. This high-energy charge

³This raises a question of terminology. Though many people use “gamma-ray” to refer to photons with energy above 50–100 keV and “x-ray” for photons with lower energy, this is not correct. Technically speaking, the term “gamma-ray” refers solely to photons produced by nuclear processes, while the term “x-ray” refers to photons produced by electrons either by bound state energy level transitions or by collisions. As the photons in a TGF are not produced by nuclear processes, strictly speaking TGFs ought to be “terrestrial x-ray flashes,” but the initial name has stuck, probably because TGF is easier to pronounce than TXF.

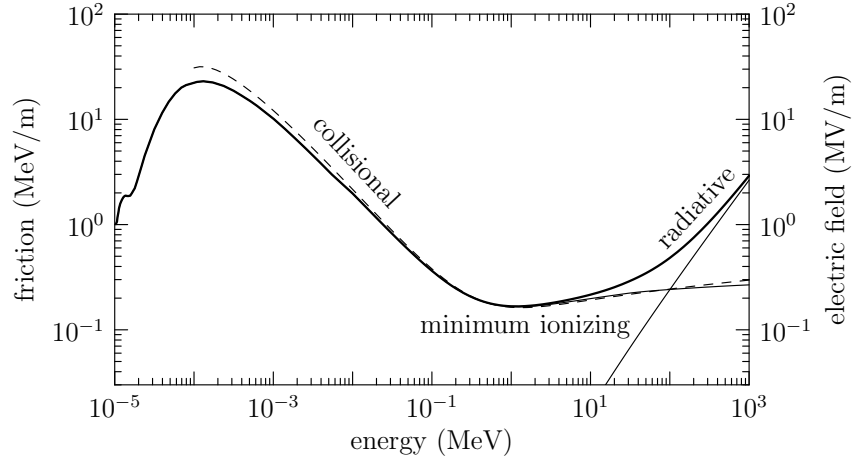


Figure 2.3: **Friction on electrons in air at sea level.** Shown as a function of electron energy. “collisional” and “radiative” labels indicate dominant process for energy range in question. The dashed curve is the Bethe-Bloch equation (Equation 2.14.) Data taken from *International Commission on Radiation Units and Measurements* (1984). The axis on the right indicates the electric field strength required to produce a force on an electron equal to the frictional force.

acceleration is the process that produces TGF photons. At lower energies, electron-electron collisions dominate the energy loss and can be well-described by consideration of the kinematics of collisions between energetic incident electrons and stationary atomic electrons. At the lowest energies, the velocity of the atomic electrons cannot be neglected, shielding of the incident electron charge becomes important, and the behavior again changes. The rest of this section considers these energetic electron interactions in detail: radiative processes, electron-electron collisions, and low-energy behavior.

The most common process where energetic photons are produced by energetic electrons is when the energetic electrons collide with atomic nuclei. Classically, the acceleration of the electron as it is deflected by Coulomb interaction with a nucleus results in the emission of electromagnetic waves. Quantum-mechanically, the interaction of the electron with the nucleus by exchange of a virtual photon allows for the

emission of a real photon with nonzero amplitude as calculated in quantum electrodynamics. A Feynman diagram of bremsstrahlung is shown at right in Figure 2.2. In the context of quantum electrodynamics, bremsstrahlung and pair production are related by rearrangements of particles in time. Pair production involves an outgoing positron and an incoming photon, while bremsstrahlung involves an incoming electron and an outgoing photon. The cross section formulas for bremsstrahlung are thus derived similarly to pair production formulas and are similarly complicated and depend on similar approximations. A detailed review is given in *Koch and Motz* (1959).

One such approximation is to assume photon energy $h\nu \gg m_e c^2$ (Formula 3BS in *Koch and Motz*, 1959):

$$\frac{d\sigma}{d\nu} \simeq \frac{4Z^2 r_e^2 \alpha}{\nu} \left\{ \left(1 + \frac{E^2}{E_0^2} \right) \left[\frac{\phi_1(\xi)}{4} - \frac{1}{3} \ln Z - f(Z) \right] - \frac{2}{3} \epsilon \left[\frac{\phi_2(\xi)}{4} - \frac{1}{3} \ln Z - f(Z) \right] \right\} \quad (2.7)$$

where E and E_0 are the final and initial total energy of the electron, the photon energy $h\nu = E_0 - E$, $\phi_1(\xi)$ and $\phi_2(\xi)$ are screening functions usually given numerically in terms of $\xi = 100m_e c^2 h\nu / (E_0 E Z^{1/3})$, and $f(Z)$ is the same as in the case of pair production. The leading $1/\nu$ dependence means more photons are produced at low energies than at high energies, while the energy radiated per unit photon energy remains roughly constant.⁴

The total energy loss per unit length due to bremsstrahlung for electrons for the complete screening case (i.e., the same conditions as Equation 2.6) is

$$-\left(\frac{dE}{dx} \right) \simeq 4N E_0 Z^2 r_e^2 \alpha \left[\ln(183Z^{-1/3}) + \frac{1}{18} - f(Z) \right] \quad (2.8)$$

⁴This suggests an infinite number of photons emitted at zero energy, an “infrared divergence.” This divergence is limited by so-called dielectric suppression, where the emitted photon may Compton scatter and interfere with its own emission. The Landau-Pomeranchuk-Migdal (LPM) effect where multiple scattering of the incident electron interferes with photon emission also plays a role. These effects are discussed in detail in *Anthony et al.* (1997).

where N is the number density of atoms of the material (*Leo*, 1994, pp. 38–40). Note the linear relation to E_0 ; the more energetic the incident electron is, the more energy it loses to bremsstrahlung. For high energy electrons, radiative processes are the dominant energy loss mechanism.

Relatively lower energy electrons, however, lose a larger fraction of their energy to collisional processes. These collision processes lead to a variety of products. If the collision excites an atom or molecule, either rotationally, vibrationally, or electronically, the energy loss process is dubbed collisional excitation. If the collision frees a low-energy electron, the process is dubbed ionization. If the collision produces a secondary electron with high enough energy to be considered an energetic particle in its own right, the process is called δ -ray production.

A good understanding of the mechanics of these collisions can be derived from consideration of classical physics (*Jackson*, 1999, pp. 624–627). Consider electron-electron collisions. Coulomb interactions result in energy exchange, an effect that can be estimated by calculation of the impulse of the collision. Consider the Rutherford scattering cross section (as derived in, for example, *Goldstein et al.*, 2002, p. 109)

$$\frac{d\sigma}{d\Omega} = \left(\frac{q_e^2}{8\pi\epsilon_0 p v} \right)^2 \frac{1}{\sin^4 \frac{\theta}{2}} \quad (2.9)$$

where θ is the deflection between incident and outgoing electron directions, q_e is the electron charge, ϵ_0 is the permittivity of free space, p is the incoming electron momentum, and v is the incoming electron velocity. As the relevant quantity is the impulse of the collision, it is useful to re-express Equation 2.9 in terms of the momentum exchanged, $Q = p' - p$. In the elastic case, Q can be expressed as

$$Q^2 = p'^2 + p^2 - 2pp' \cos \theta = 4p^2 \sin^2 \frac{\theta}{2} \quad (2.10)$$

which gives $dQ^2 = 4p^2 \sin \theta d\theta$. Combination of these results with $d\Omega = 2\pi \sin \theta d\theta$ gives

$$d\Omega = \frac{\pi}{p^2} dQ^2 \quad (2.11)$$

Substitution of Equations 2.11 and 2.10 into Equation 2.9 and recognition that the energy transferred in the collision $T = Q^2/2m$ gives

$$\frac{d\sigma}{dT} = \frac{q_e^4}{8\pi\epsilon_0^2 m_e v^2 T^2} \quad (2.12)$$

This equation can be integrated between suitable limits to find the total cross section for collisions with energies between the given limits. A suitable minimum energy limit is the typical binding energy of the electrons in the material, $T_{\min} = I$. The maximum energy limit here comes from the energy transmitted in a head-on electron-electron collision where the incident electron stops and the secondary electron acquires all the kinetic energy: $T_{\max} = (\gamma - 1)m_e c^2$ where here $\gamma = 1/\sqrt{1 - \beta^2}$, $\beta = v/c$.

As the right hand side of Equation 2.12 is proportional to $1/T^2$, low-energy collisions are much more likely than high-energy collisions. The numerous low-energy secondary particles produced in such collisions are typically classified as “ionization.” We can therefore focus our attention on the incident particle and treat the production of such low-energy secondaries simply as an effective energy loss per unit path length. This energy loss can be calculated from Equation 2.12, scaling by the density of electrons to give the effective number of collisions per unit length and multiplying by the energy loss in such collisions. Integrating over the energy loss between the limits given above,

$$-\frac{dE}{dx} = \int_{T_{\min}}^{T_{\max}} \frac{d\sigma}{dT} N Z T dT = \frac{q_e^4 N Z}{8\pi\epsilon_0^2 m_e v^2} \ln \left[\frac{(\gamma - 1)m_e c^2}{I} \right] \quad (2.13)$$

Examination of Equation 2.13 gives a broad understanding of behavior of the energy

loss of electrons. For non-relativistic electrons, the $1/v^2$ behavior dominates, and the energy loss per unit path length drops rapidly as the energy increases. Once the electrons become relativistic, their velocity stops increasing and the relatively weak logarithmic dependence on γ takes over and the energy loss gradually increases.

In reality, quantum mechanical effects are important, especially for low energy secondaries ($T < I$), though the overall form does not change significantly. The quantum mechanical result, known as the Bethe-Bloch formula,⁵ typically includes several correction factors (*Leo*, 1994, p. 24):

$$-\frac{dE}{dx} = \frac{q^4 N Z}{8\pi\epsilon_0^2 m_e v^2} \left[\ln \left(\frac{2(m_e c^2)^2 \beta^2 \gamma^2 (\gamma - 1)}{I^2} \right) - 2\beta^2 - \delta - 2\frac{C}{Z} \right] \quad (2.14)$$

where the $-2\beta^2$ term is a relativistic spin correction, δ is the “density correction” and C is the “shell correction.” The values of δ and C are usually given numerically.

For low energy incident electrons, the Bethe-Bloch formula breaks down as the velocity of the incident electron becomes comparable to the effective orbital velocity of the atomic electrons in the material. Such velocities allow for shielding of the incident electron charge which thus interacts less strongly. The stopping power therefore has a peak at the low energy end of the validity of the Bethe-Bloch formula and drops off for lower energies as shielding effects become progressively more important. No satisfactory theory exists to describe the interactions that occur for electron energies in this very-low-energy regime and empirical fits to experimentally-determined values are typically used *Eidelman et al.* (2004).

At energies < 10 eV, off the left end of the x -axis in Figure 2.3, the energy of the incident electron becomes comparable to the energy of atomic and molecular energy level transitions and very complex behavior results with many peaks and valleys in

⁵Simply the Bethe formula in some sources.

the stopping power. A good survey of these interactions, including detailed lists of the transitions, threshold energies, and final states is given in *Moss et al.* (2006).

2.2 Electric field effects

The physical processes described above govern the behavior of energetic electrons and photons. These processes often interact in complicated ways with unexpected consequences.

One example is the production of an electromagnetic shower. A population of electrons produces photons by bremsstrahlung, while a population of photons produces electrons by Compton scattering and pair production. A very energetic incoming electron therefore produces secondary electrons and photons which produce further electrons and photons in a cascade or shower of secondary particles. Considering one photon to produce two energetic secondaries in pair production, each of which contributes some of its energy to one energetic bremsstrahlung photon, each pair production and bremsstrahlung step multiplies the number of particles by four. This progressive multiplication leads to exponential growth of the number of particles until the particles no longer have enough energy to pair-produce or emit bremsstrahlung. This type of avalanche growth process hints at the rich behavior of energetic particle dynamics in materials.

The picture is further complicated by the presence of an electric field. The stopping power, as shown in Figure 2.3 can be thought of as a frictional force or an energy loss per unit path length. For charged particles such as electrons, an electric field also contributes a force or an energy gain per unit path length shown as the right axis in Figure 2.3. If the frictional force exceeds the electric force, the particle slows down, while if the electric field is stronger than friction the particle accelerates. This behavior depends on the energy of the electron. Consider a 1 keV electron in a 1 MV/m

electric field in air at sea level. Figure 2.3 shows that for this electron, the frictional force exceeds the electric field force, and the particle will lose energy. A 1 MeV electron, by contrast, experiences much less friction and the electric force due to a 1 MV/m electric field exceeds the friction force and the particle will accelerate to become what is called a “runaway” electron. The production of such runaway electrons above thunderstorms was predicted by *Wilson* (1924) as mentioned in Section 1.1.

2.2.1 Runaway relativistic electron avalanche (RREA)

These runaway electrons continue to interact with the material as they accelerate, and occasionally will undergo hard electron-electron collisions. These collisions may impart a significant amount of energy to the secondary electron. If the secondary electron has enough energy, it too may experience a sufficiently low frictional force to be accelerated by the electric field and can also be considered a runaway. This multiplication in the number of runaway electrons leads to avalanche growth in the population of energetic electrons, a process called runaway relativistic electron avalanche (RREA). This possibility of avalanche growth was first predicted by *Gurevich et al.* (1992).

Several properties of RREA are evident from Figure 2.3. First, there is a minimum energy of runaway electrons given by the point where the electric force equals the frictional force. For the 1 MV/m electric field mentioned above, this minimum energy is approximately 30 keV. Second, note that at a given electric field, there is also an upper limit on runaway electron energy, above which radiative losses dominate and the particle will lose energy. For instance, a 0.25 MV/m electric field can accelerate runaway electrons to energies no higher than 20 MeV. Third, electric forces below the minimum ionizing friction force cannot produce runaway electrons. This minimum electric field strength is $\simeq 0.2$ MV/m. Note that this minimum electric field strength is much lower than the minimum electric field necessary to produce sparking, a fact

considered in more detail in Section 2.3.3. Fourth, for electric forces stronger than the maximum frictional force on non-relativistic electrons, i.e., above $E_c \simeq 25 \text{ MV/m}$ for 100 eV electrons, there is no minimum energy of runaway electrons. Such a field can accelerate any free electron to relativistic energies, a process called cold runaway. Finally, note that for $E < E_c$, low-energy electrons cannot be accelerated to high energies. Seed energetic electrons are therefore needed to initiate RREA. In the Earth's atmosphere, these seed particles likely originate from cosmic rays, a topic treated in more detail in Chapter 4.

Since the prediction of runaway electrons (*Wilson*, 1924) and avalanche growth (*Gurevich et al.*, 1992), the properties of RREA have been studied in more detail. The distribution of electron velocities and energies and its time evolution can be studied by solution of the Boltzmann equation, which describes the time-evolution of the distribution function f , where f describes the number of electrons per phase space volume. One implementation of this, ignoring spatial variations and assuming cylindrical symmetry about the electric field is described in *Roussel-Dupré et al.* (1994):

$$\frac{\partial f}{\partial t} = \left[\frac{1 - \mu^2}{p} \frac{\partial f}{\partial \mu} + \mu \frac{\partial f}{\partial p} \right] eE + \frac{\partial_e f}{\partial t} \quad (2.15)$$

where $f = dN_e/d\mu dp$, $\mu = \cos \theta$, θ is the angle between the particle momentum and the electric field, p is the magnitude of the momentum, e is the electron charge, E is the electric field strength, and $\partial_e f / \partial t$ describes the collision processes (both loss due to scattering and gain due to scattering products from other momenta) and can be derived from the physics behind the Bethe-Bloch equation (Equation 2.14), for instance as in *Gurevich et al.* (1998). One weakness of this approach is that the Boltzmann equation is difficult to solve in practice as it is a partial differential equation in principle involving 7 dimensions: space, momentum, and time. Symmetry arguments and approximations must be made to render this computationally tractable, as in

the cylindrical symmetry applied in Equation 2.15, but even then the equation must be approached with great care. *Roussel-Dupré et al.* (1994) for example accidentally used an unstable discretization scheme for Equation 2.15 and thus derived incorrect avalanche rates, an error only uncovered years later (*Symbalist et al.*, 1998).

Another approach is to further assume that all runaway electrons travel in the direction of the electric field and to simply treat the number of runaway electrons, neglecting their energy spectrum (*Bell et al.*, 1995):

$$\frac{\partial N}{\partial t} + v \frac{\partial N}{\partial z} = \frac{N}{\tau} + S \quad (2.16)$$

where N is the number density of relativistic electrons, v is the velocity of the avalanche, τ is the avalanche growth time constant, and S is a source of relativistic seed particles due to cosmic rays. Such simplifications allow for self-consistent simulations of avalanche growth, and can be used to calculate feedback effects such as the overall current produced (*Gurevich et al.*, 2004a) and the effects of this current on the avalanche itself (*Gurevich et al.*, 2006).

Another approach to the study of RREA is to use Monte Carlo simulations of the trajectories and interactions of individual particles. Such Monte Carlo simulations involve tracking individual particles and their interactions where the actual behavior is drawn at random from the distributions given by the physics describing the interactions. This approach, if repeated many times, gives the average behavior of the system in question.

Such simulations can be very useful for determining the properties of RREA. In particular, *Coleman and Dwyer* (2006) used Monte Carlo techniques to determine the avalanche growth rate and propagation speed. The avalanche growth length-scale λ and timescale τ cannot be determined analytically by Monte Carlo simulation, but the

simulation results can be very well fit by simple analytical forms for $E > 300 \text{ kV/m}$:

$$\lambda(z) = \frac{(7300 \pm 60) \text{ kV}}{E - \frac{n(z)}{n_0}(276 \pm 4) \text{ kV/m}} \quad (2.17)$$

$$\tau(z) = \frac{(27.3 \pm 0.1) \text{ kV } \mu\text{s/m}}{E - \frac{n(z)}{n_0}(277 \pm 2) \text{ kV/m}} \quad (2.18)$$

where E ($> 300 \text{ kV/m}$) is the electric field strength, n is the atmospheric density, z is the altitude, and $n_0 = n(0)$. As altitude increases, lower collision frequencies and therefore lower frictional losses result in scaling of the relevant electric fields with density, i.e., $E \propto n(z)/n_0$ while length and timescales scale as $\lambda, \tau \propto n_0/n(z)$. The avalanche propagation speed is found to be nearly constant at $v \simeq 2.65 \times 10^8 \text{ m/s}$. Another result from these studies is that the minimum electric field strength above which RREA can occur is $E_{\text{RREA}} = 286 \text{ kV/m}$, larger than the $\sim 200 \text{ kV/m}$ one might expect from examination of Figure 2.3 and the $\sim 276 \text{ keV/m}$ expected from consideration of Equations 2.17 and 2.18. Note that this value is comparable to the minimum electric field necessary to produce 20 MeV electrons mentioned in Section 2.2.1.

The Monte Carlo approach can be very accurate, but its accuracy is limited by the number of particles that can be simulated within the capacity and speed of computers. As the number of particles involved in the atmosphere is very large, Monte Carlo simulations typically assume the response of the system to an initial seed population to be purely linear. The results of a simulation of a manageable number of particles can then be scaled up to match more realistic conditions. This assumption requires that the electric fields produced during the RREA process does not in any way affect the development of the avalanche, an assumption that is violated for large avalanches which themselves generate an appreciable electric field.

One very interesting result uncovered by Monte Carlo studies of RREA is that for large electric fields and large field regions, the effects of photon production cannot be

ignored (*Dwyer*, 2003). Consider an avalanche initiated in the low-voltage portion of a region within which there is a strong electric field. Note that the dominant factor in the growth of a single avalanche is electron-electron collisions where secondary electrons from such interactions join the primary electrons as runaways. Such an avalanche grows as it propagates toward the high voltage region, but once it propagates out of the electric field region entirely, it rapidly decays away. However, there is an inherent instability in the system due to the production of photons. This instability is due to two effects: photon propagation and pair production. Photons produced by bremsstrahlung in an initial avalanche as it grows can scatter and propagate back toward the low voltage region. As such, these photons can produce energetic electrons and thus initiate a second avalanche which also grows as it propagates toward the high voltage region. Photons produced by bremsstrahlung may also pair-produce. The resulting positrons are driven in the opposite direction of the avalanche by the electric field. The positrons also therefore tend to travel back toward the low voltage region and are capable of initiating avalanches.

There are therefore two effective growth rates: the exponential growth rate of a single avalanche, and the exponential growth rate of the number of avalanches. The growth rate in the number of avalanches is determined by the geometry of the electric field as discussed in *Dwyer* (2003). This feedback effect can lead to “relativistic breakdown.” When the number of avalanches increases exponentially with time, the only effect that stops the overall exponential growth in the population of energetic particles is the decay of the electric field. This effect is discussed in detail in *Dwyer* (2007). Relativistic feedback and the likelihood of relativistic breakdown are discussed further in Section 5.5.

2.3 Spark physics

TGF photons, produced by bremsstrahlung from energetic electrons in the context of lightning imply the presence of energetic electrons in electric fields. RREA, the avalanche growth of a population of energetic electrons driven by an electric field, is naturally suggested as relevant to TGF production. However, the electric field necessary to drive RREA as produced by lightning requires an understanding of the behavior of low-energy electrons. Such electrons undergo similar processes to high-energy electrons but the resulting physics is that of dielectric breakdown instead of relativistic breakdown.

2.3.1 Low-energy electron behavior

Electrons with energy below 100 eV are not able to become relativistic except in the case of cold runaway driven by very strong electric fields. From the perspective of RREA, such electrons are not relevant and simply drift under the influence of the electric field at energies ~ 10 eV.

Nevertheless, the behavior of these electrons is in many ways more rich than the behavior of relativistic electrons. Though a full discussion of their behavior is far beyond the scope of this dissertation, a summary is presented below. A more complete description can be found in *Raizer* (1997), Chapters 1–5.

Such low-energy electrons interact in two main ways: collisional ionization and attachment. Attachment occurs when an incident low-energy electron remains attached to an atom or molecule after a collision, producing a negative ion. Collisional ionization occurs when an incident low-energy electron strikes an atom and releases a secondary electron, leaving a positive ion. Without a driving electric field, the attachment rate is much greater than the ionization rate and free low-energy electrons are quickly lost to form ions.

The key feature of ionization and attachment in the context of this dissertation is that their overall rates depend on the strength of the applied electric field. Attachment rates slowly increase with electric field strength, while collisional ionization rates increase much more rapidly (*Raizer*, 1997, pp. 135–136). The ionization rate equals the attachment rate for electric field strengths $E_k \simeq 3 \text{ MV/m}$ in air at sea level. If the electric field is stronger than E_k , the ionization rate exceeds the attachment rate, and the population of free low-energy electrons increases exponentially in a low-energy avalanche growth process. Such avalanches grow rapidly over length scales typically less than 1 mm.

2.3.2 Streamers, sparks

Though small, such avalanches can move enough charge to affect their surroundings. This nonlinear feedback effect allows the production of “streamers,” self-sustaining discharges continually fed by avalanches near their tip as shown in Figure 2.4. Essentially, electric fields above E_k render air conducting. The conductivity leads to a decay in the electric field in some regions, but intensification of the electric field near the tip of the conducting region. This intensification allows the electric field to remain above E_k over a small region, the so-called streamer head. The streamer head constantly advances with the continual interplay of avalanche, field decay and field intensification near the head at a velocity $v_s \simeq 10^6 \text{ m/s}$ (for further detail, see *Raizer*, 1997, p. 334–338).

Under conditions of sustained high voltage applied to an electrode, streamers are continually produced and propagate away from the electrode resulting in a faint glow around the tip of the electrode called corona discharge. Streamers propagate until the electric field drops below a critical threshold value E_{cr} that depends on whether the streamer is positively or negatively charged. For negatively charged streamers, $E_{\text{cr}}^- \simeq 1.25 \text{ MV/m}$, while for positively charged streamers $E_{\text{cr}}^+ \simeq 0.44 \text{ MV/m}$.

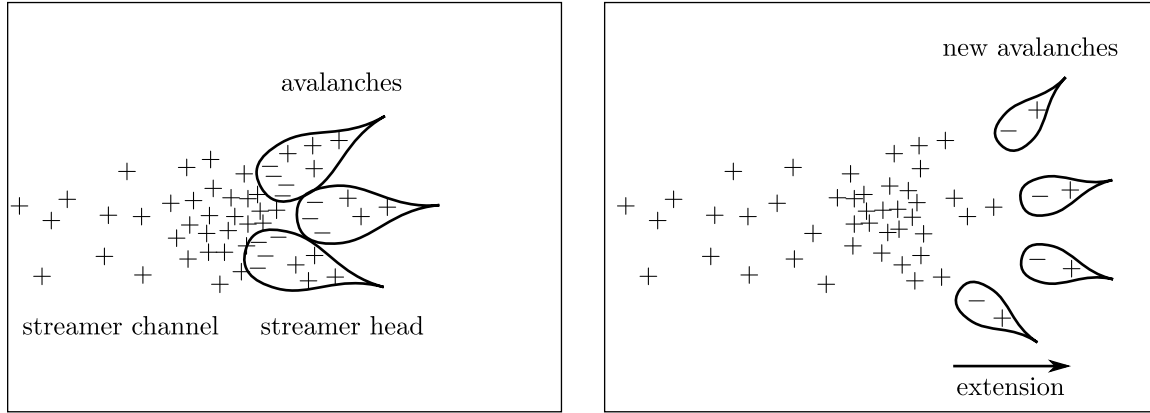


Figure 2.4: **Positive streamer discharge growth.** Avalanches induced by the local concentration of positive charge neutralize portions of this charge while leaving positive charge behind elsewhere. This leads to an overall migration of the charge region and growth of the streamer.

If the streamer production rate is high enough, the air near the core of the corona discharge will be heated to thousands of degrees Kelvin. With such heating, the ionization rate increases rapidly and the gas becomes a conducting plasma even without a strong applied electric field. This process results in the same general phenomenon as a streamer, only on a larger scale. The electric field in the hot conducting region decays away but is correspondingly intensified near the edges of the conducting region. If this intensification is sufficient, it will heat the gas in a new region to conducting, and the process will repeat. This growing discharge process leaves behind a conducting hot plasma channel through which a current flows to sustain the corona discharge near the tip of the channel. On small and medium scales, this conducting plasma channel is called a spark. Exactly how such discharges occur is still an open question, though the overall picture is as described above. A good overview of the process can be found in *Gallimberti et al.* (2002).

The processes described above depend on altitude (i.e., air density) in much the same way as RREA. Lower atmospheric densities result in lower collision frequencies

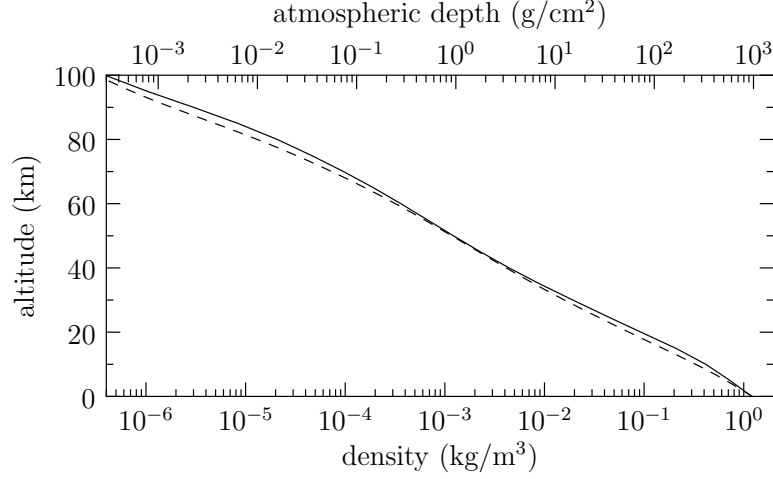


Figure 2.5: **Atmospheric density vs. altitude.** Atmospheric density and depth shown as a function of altitude above sea level. The dashed curve shows atmospheric depth measured from the top of the atmosphere on the upper x axis, while the solid curve shows density on the lower x axis. Data taken from the MSIS model (*Hedin, 1991*).

and longer mean free paths, allowing lower electric fields to provide comparable energy gains between collisions. Threshold electric fields therefore decrease with density, $E \propto n(z)/n_0$. The length scale of the streamer head increases as the mean free path, i.e. $\propto n_0/n(z)$. The charge density within the streamer head required to maintain the length and electric field scaling relationships therefore scales as $\rho \propto (n(z)/n_0)^2$. The atmospheric density decreases roughly exponentially with altitude with a scale height $\simeq 7$ km, as shown in Figure 2.5. As such, these scaling relationships determine the behavior of streamer and spark discharges at high altitudes.

2.3.3 Lightning and thunderstorms

The physics of lightning, though fundamentally a spark discharge on a large scale, is complicated and very diverse. An extensive discussion can be found in *Rakov and Uman* (2003, Chapters 1, 3–6, and 9). The essential results in the context of this

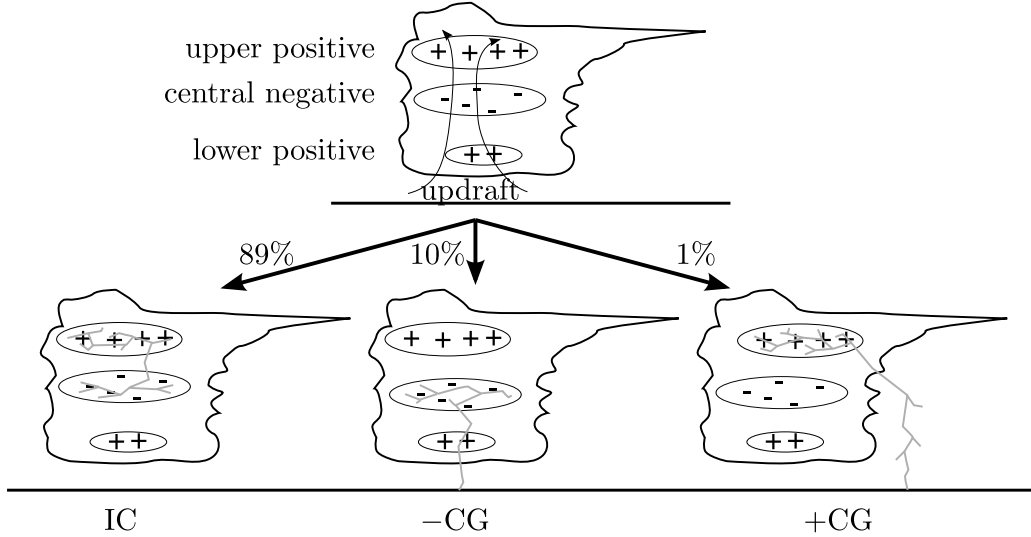


Figure 2.6: **Typical thunderstorm charges and discharges.** Typical thunderstorms have a large central negative charge region flanked by large upper positive and a smaller lower positive charges. The three main types of lightning are shown below: intra-cloud (IC), negative cloud-to-ground ($-CG$) and positive cloud-to-ground ($+CG$).

dissertation are discussed below.

A typical thunderstorm has an overall charge distribution as shown in Figure 2.6. Screening charges also collect on the outer regions of the cloud, and the presence of downdrafts further complicates the structure in some cases (*Stolzenburg and Marshall, 2008*). The process by which thunderstorms develop charge separation is poorly understood and likely involves a combination of mechanisms (for a short review, see *Yair, 2008*).

The electric field magnitudes measured locally by balloon-borne electric field meters are typically $50\text{--}100\text{ kV/m}$ (*Betz et al., 2009, p. 65*), giving a total thunderstorm potential of $U \simeq 100\text{ MV}$ (*Marshall and Stolzenburg, 2001*). Interestingly, the measured electric fields never approach E_k , the conventional breakdown threshold. This observation is one of the great puzzles of atmospheric electricity: lightning initiation.

If the electric fields never get large enough to cause a spark to occur, how does a discharge ever commence? If the electric field is only intensified over a region so small that experiments have not yet been lucky enough to measure it, what is the mechanism for such local enhancement of the field strength? While the measured electric field is never near E_k , it is sometimes measured to be just above E_{RREA} . In particular, measurements of $E \simeq E_{\text{RREA}}$ are often accompanied by lightning within a few seconds (*Marshall et al.*, 2005). This hint that lightning initiation may be associated with RREA is tantalizing.

Whatever the mechanism, however, lightning begins as a short conducting plasma channel called a lightning leader that gradually grows as the discharge develops over many kilometers over the course of ~ 0.5 s. The growth behavior of the leader channel depends on the polarity of the channel as shown in Figure 2.7. Positive leader channels grow relatively smoothly at 0.4×10^6 – 2.4×10^6 m/s by continuous heating and ionization near the tip by electron avalanches attracted to the positive charge in the tip (*Rakov and Uman*, 2003, p. 224). Negative leaders, by contrast, repel electron avalanches and thus do not focus the heating and ionization as sharply. As a consequence, negative leaders develop in a series of steps, each taking place when the heating and ionization in a region somewhat displaced from the leader tip becomes sufficient to initiate a second leader segment which then grows back to connect with the main channel (*Gallimberti et al.*, 2002). Average negative leader extension velocities are of order 0.06×10^6 – 1.1×10^6 m/s, with typical step lengths 10–200 m.

This complicated bidirectional leader development roughly follows the electric field, though the random nature of avalanche and streamer development, coupled with the feedback effects of heating produce a channel with many kinks and branches. The resulting channel either connects positive and negative parts of the cloud in intra-cloud (IC) lightning or connects the cloud to the ground. In cloud to ground (CG) lightning, either negative (–CG) or positive (+CG) charge is moved to ground. These

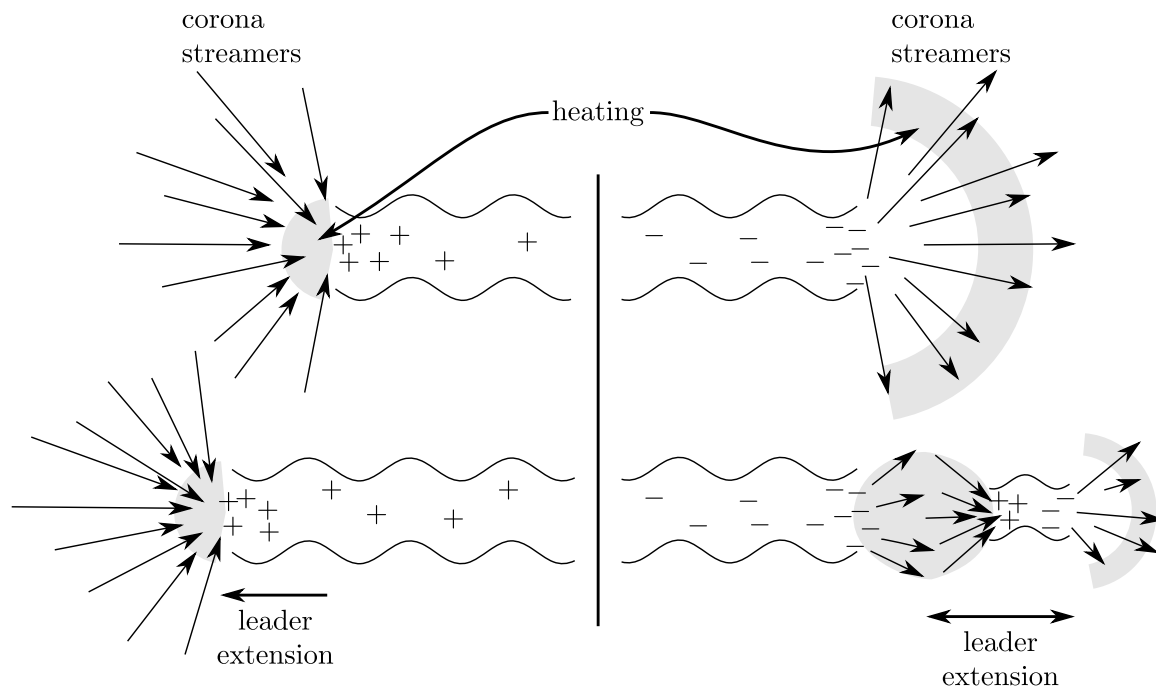


Figure 2.7: **Leader extension process.** The leader extension process for positive leaders (left) and negative leaders (right). Positive leaders grow through smooth extension of the heated region at the tip, while negative leaders grow discontinuously through the formation of new segments in the heated region away from the tip which grow back toward the main leader.

three types of lightning are shown in Figure 2.6. Overall, $\sim 89\%$ of all lightning is IC, $\sim 10\%$ is $-CG$, and the remaining $\sim 1\%$ is $+CG$.

CG lightning typically initiates somewhere in the cloud and develops from the central negative charge region toward the ground, possibly under the influence of the smaller lower positive charge region. This process is shown schematically in Figure 2.8. As the leader channel is conducting, the leader as a whole is roughly an equipotential. The development of the channel towards ground therefore carries the potential of the cloud towards the ground. This potential drives the accumulation of charge on the leader channel. Typical leader charge densities are $\sim 3 \text{ mC/m}$ (*Rakov and Uman*, 2003, pp. 123–126, 330–331). When the channel reaches ground, the discrepancy

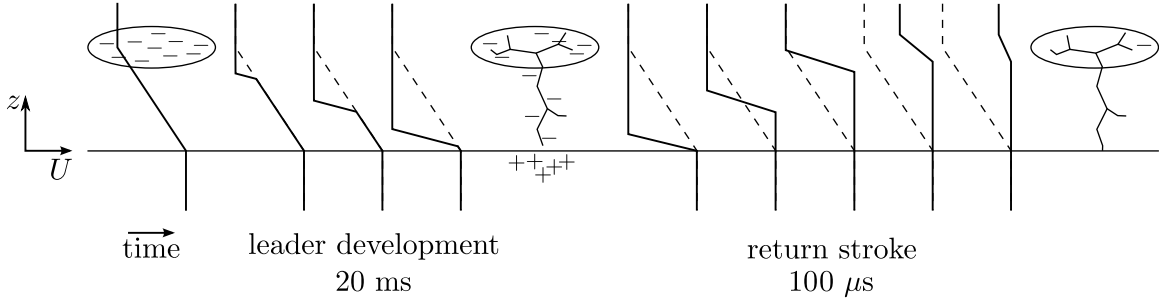


Figure 2.8: **Lightning and return stroke voltage.** Schematic of voltage changes involved in a typical $-CG$ lightning discharge. The leader carries cloud potential to ground, while the return stroke carries ground potential up to cloud and partially neutralizes the cloud charges. The solid line represents the voltage as a function of altitude in the phase in question. The dashed line represents the pre-discharge voltage as a function of altitude.

between cloud voltage and ground voltage is very rapidly neutralized in a large current pulse, the so-called return stroke. $-CG$ return stroke peak currents range from 10 to 100 kA and last from 30 to 200 μs , while $+CG$ return stroke currents range from 4 to 250 kA and last from 25 to 2000 μs (*Rakov and Uman*, 2003, pp. 146, 215). If sufficient charge remains in the cloud after the return stroke, further development of the channel in the cloud can lead to subsequent return strokes. Overall, from initiation to cessation of activity, such a lightning discharge may take place over a time period of order 1 s.

2.3.4 Radio emissions

Return stroke current pulses along effectively vertical leader channels between ground and cloud radiate electromagnetic waves with the bulk of the power emitted in the very-low frequency band (VLF, between 3 and 30 kHz) (*Rakov and Uman*, 2003, p. 443). Overlapping the audio frequency band, these signals can be heard if converted to sound waves as sharp clicks dubbed radio atmospherics or “sferics.” This frequency

band is also efficiently reflected by both the ground and the ionosphere and is therefore confined to and guided by the Earth-ionosphere waveguide. These signals can thus be detected from great distances, up to 10 Mm or more.

Such VLF radio emissions allow for remote detection of lightning, a fact mentioned in the context of TGF studies in Section 1.2.2. In particular, radio emissions can be used to determine the location of the source lightning. A review of lightning geolocation techniques can be found in *Rakov and Uman* (2003, pp. 555–587). The direction from which a signal arrives at a receiver can be determined by comparing the signals received by two orthogonal antennas (*Wood and Inan*, 2002). If the signal is received at three or more receivers, advanced arrival time determination techniques allow the location and time of the source lightning discharge to be determined very accurately (*Said*, 2009). The shape and duration of the radio pulse received allows the peak current and charge moment change parameters of the lightning to be determined (*Cummer and Inan*, 2000; *Wood*, 2004).

IC lightning, by contrast, does not connect to the ground and therefore does not show the rapid current pulses and voltage changes seen in return strokes. The current structures in IC lightning are therefore largely driven by the development of the channel into charge regions of varying density. Phenomena such as J- and K-processes (measured electric field changes during a lightning discharge not associated with a return stroke *Rakov and Uman*, 2003, pp. 183–188), and M-components (current surges observed in lightning channels *Rakov and Uman*, 2003, pp. 177–182) are likely due to such development and the resulting currents as charge densities on and near the leader channel are rearranged.

As typical IC lightning does not have the characteristic vertical channel seen in CG lightning, the lack of vertical currents prevents radio emissions from IC lightning from efficiently driving modes of the Earth-ionosphere waveguide. IC lightning therefore cannot typically be detected from large distances in VLF radio observations and is

therefore relatively difficult to study. This difficulty, together with the fact that IC lightning does not damage ground structures or start fires, has left study of IC discharge a low priority.

This picture changed with the development of 3-dimensional lightning mapping techniques such as those used by the New Mexico Tech Lightning Mapping Array (LMA, see *Rison et al.*, 1999). Such systems are limited to lightning no further than a few hundred kilometers from the receivers, but observe each lightning discharge as a sequence of high-frequency (HF, 60–66 MHz for the LMA) pulses, each associated with small bursts of activity associated with extension of the leader channel. Such HF pulses are emitted frequently by negative leaders due to the stepping process, but also appear weakly for positive leaders. These HF pulses (discussed in detail in *Thomas et al.*, 2001) are detected at an array of receivers, and their arrival times are used to triangulate the source location in three dimensions. The result is a map in space and time of HF radio activity which allows the approximate path of the leader channel in the cloud to be estimated. This window into IC activity can be used for example to study lightning initiation (*Betz et al.*, 2008), IC lightning currents, and chemical effects (*Betz et al.*, 2009, pp. 231–251).

The physics of lightning, though a complex process ranging from sub-millimeter electron avalanches and streamers to multi-kilometer leader channels, can be summarized as follows. Updrafts drive air currents which produce a charge structure as shown in Figure 2.6. Some unknown mechanism subsequently initiates lightning. Lightning then proceeds as the bidirectional development of a conducting leader channel which allows charge from the thunderstorm to rearrange. If the leader reaches the ground (CG lightning), the large and sudden voltage changes drive a powerful current (the return stroke), which neutralizes charges along the channel and efficiently radiates impulsive VLF radio waves that can be detected from great distances. If the leader channel does not reach ground (IC lightning), current pulses are driven by channel

extension and the resulting rearrangements of charge. These discharge processes are summarized in Table 2.1. How these processes may result in TGF production is the subject of the next section.

2.4 TGF production theories

As discussed at the beginning of this chapter, TGFs involve high-energy photons produced by bremsstrahlung. These bremsstrahlung photons come from energetic electrons accelerated by electric fields. The observed coincidence with lightning suggests that these electric fields are associated with lightning and thunderstorms. The consideration of energetic electron and photon physics (Sections 2.1.1 and 2.1.2) and their behavior in electric fields leads to predictions of the avalanche growth of populations of energetic electrons (RREA), facilitating the production of large bursts of bremsstrahlung photons. This outline of TGF physics is shown in Figure 2.9.

The main unknown in this picture is the mechanism of production of the electric field. Studies of thunderstorms and lightning do little more than suggest that such fields might exist, leaving their behavior and magnitude unknown. To attempt to provide a more complete picture, two main mechanisms have been proposed for electric field production and subsequent TGF generation: the quasi-electrostatic and electromagnetic pulse mechanisms.

2.4.1 Quasi-electrostatic mechanism

The quasi-electrostatic TGF production mechanism is a modernization of C. T. R. Wilson's observation that the electric field above a thundercloud decreases less quickly than the atmospheric density, first discussed here in Section 1.1. The rapidly-decreasing atmospheric density results in rapidly-decreasing threshold electric field strengths, both for sparking as noted by Wilson and for RREA. This realization

process		properties
streamers	tip	$q \simeq 10 \times 10^{-10} \text{ C}$ $E \simeq 10 \text{ MV/m}$ $r \simeq 0.2 \text{ mm}$ $U \simeq 10\text{--}100 \text{ kV}$
	+,− propagation	$E = 0.5 \text{ MV/m}, 1.5 \text{ MV/m}$
leaders	tip/step	$q \simeq 10\text{--}100 \text{ mC}$ $r \simeq 6 \text{ m}$ $l \simeq 10\text{--}100 \text{ m}$ $U \simeq 20\text{--}50 \text{ MV}$
	channel	$\Lambda \simeq 0.7\text{--}30 \text{ mC/m}$ $r \simeq 6 \text{ m}$ $l \simeq 1 \text{ km}$ $q_{\text{tot}} \simeq 10 \text{ C}$ $U \simeq 20\text{--}50 \text{ MV}$
	propagation	$E \simeq 0.1 \text{ MV/m}$
lightning	leader system	$q \simeq 10 \text{ C}$ $E \simeq 0.1 \text{ MV/m}$ $l \simeq 500 \text{ m}$ $U \simeq 10 \text{ MV}$
	return stroke	$q \simeq 10 \text{ C}$
	overall	$q \simeq 100 \text{ C}$ $E \simeq 0.1 \text{ MV/m}$ $l \simeq 5 \text{ km}$ $U \simeq 50 \text{ MV}$
storm	overall	$q \simeq 100 \text{ C}$ $E \simeq 0.1 \text{ MV/m}$ $l \simeq 3 \text{ km}$ $U \simeq 100 \text{ MV}$

Table 2.1: **Discharge process parameters.** Typical parameters of discharge and lightning processes. q : charge magnitude, E : electric field magnitude, r : radius, l : length-scale, U : potential difference, Λ : linear charge density. Propagation fields represent the ambient field required for the process in question to continue to develop after initiation. Information collected from *Cooray* (2004), *Rakov and Uman* (2003).

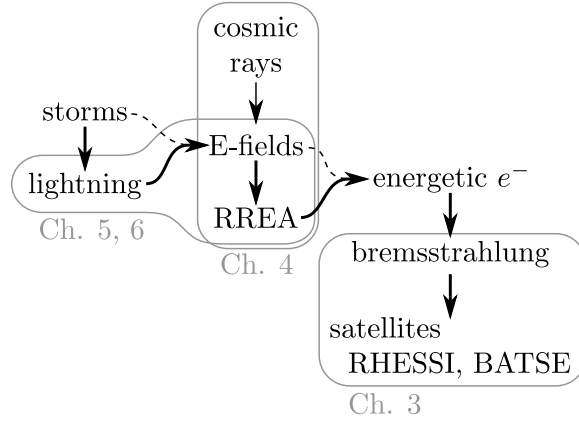


Figure 2.9: **Outline of TGF physics.** Thunderstorms produce lightning which produces an electric field. In the presence of seed particles from cosmic rays, this E-field drives RREA, which produces a large population of energetic electrons. These electrons produce bremsstrahlung, observable on satellites as a TGF. The dashed lines represent the possibility of thunderclouds directly producing electric fields and the possibility of electric field production of high-energy electrons without significant RREA. The grey labels indicate the aspects of TGF physics addressed by subsequent chapters.

raises the possibility that thundercloud electric fields or the transient fields in the aftermath of a lightning discharge may drive RREA and produce TGFs.

A full understanding of this mechanism requires consideration of the timescales involved in electric field production and decay. In the case of two parallel sheets of charge of density ρ_s , $E = \rho_s/\epsilon_0$, Ohm's law can be used to derive the relaxation time:

$$J = \sigma E = \sigma \frac{\rho_s}{\epsilon_0} = \frac{\partial \rho_s}{\partial t} \quad (2.19)$$

where σ is the conductivity and ϵ_0 is the permittivity of free space. This equation yields the decay behavior of the electric field:

$$E = E_0 e^{-t/\tau} \quad (2.20)$$

i.e., exponential decay with time constant $\tau = \epsilon_0/\sigma$. The conductivity of the atmosphere $\sigma(z, t, \dots)$ is dependent on composition and time of day but overall increases with altitude. For clear air above a cloud, the relaxation timescales range from 10 s at 20 km altitude to 100 ms at 50 km altitude (*MacGorman and Rust*, 1998, pp. 33–37). Since an active thunderstorm can produce a lightning flash every few seconds, the charging timescales are larger than the relaxation timescales above the cloud. This condition implies that for regions above the cloud, the thunderstorm’s electric field is effectively removed by the formation of screening charges.

The picture is very different just after a lightning discharge. Since the timescale of lightning discharge is ~ 100 ms, the discharge happens too quickly for relaxation to remove its effects on the electric field. A field is therefore produced above the cloud as would be produced if the charge added and removed by the lightning discharge were simply introduced in a system with no other charges. This quasi-electrostatic field decays away with the relaxation timescale, but during its existence may drive TGF production.

As noted in Section 2.2.1, electric fields can only drive RREA if energetic seed particles are present to initiate the avalanche. Here the seed particles are taken to come from cosmic rays. The complete schematic of TGF production by this quasi-electrostatic (QES) electric field is shown in Figure 2.10.

Detailed models of the QES mechanism of TGF production have been produced by various authors. *Pasko et al.* (1995) first suggested that such fields may be relevant to conventional discharge in upper atmospheric lightning, while *Bell et al.* (1995) suggested that RREA may occur and might contribute to such conventional discharges. In these papers, the electric field is constructed as a solution to the Poisson equation together with relaxation as governed by a realistic conductivity profile. The resulting electric field is used to drive a simple 1-dimensional kinetic model of RREA as given in Equation 2.16. *Lehtinen et al.* (1996) extends these results to include the angular

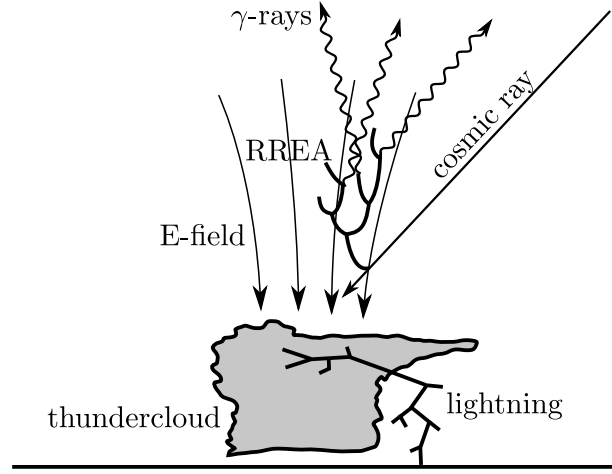


Figure 2.10: **Quasi-electrostatic TGF production mechanism.** A large +CG lightning discharge produces a large quasi-static electric field above the cloud. In the presence of energetic electrons, here provided by cosmic rays, RREA occurs, producing bremsstrahlung photons.

dependence described in *Roussel-Dupré et al. (1994)* and includes the bremsstrahlung emitted in the context of TGFs. *Lehtinen et al. (1997)* further extends the kinetic model to include radial dependence for the purpose of calculating optical emission and ionospheric effects. It was later discovered by *Symbalisty et al. (1998)* that many of the calculations in these results used avalanche growth rates too large by a factor of 10, affecting the validity of their results.⁶

Subsequent finite volume solutions to the Boltzmann equation (*Symbalisty et al., 1998*) and direct Monte Carlo simulations of RREA growth (*Lehtinen et al., 1999*) corrected the earlier results, while multi-group solutions to the Boltzmann equation reach similar conclusions (*Babich et al., 2004a,b*).

Overall, the corrected results listed above agree reasonably well. QES models for

⁶Beware instabilities: *Roussel-Dupré et al. (1994)* attempts to solve the Boltzmann equation with a scheme that is slightly unstable. The overall results remain stable due to diffusion and seem sensible, but the overall growth rates calculated were in error, effectively due to an extra source term originating in the instability.

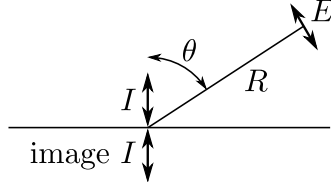


Figure 2.11: **Electromagnetic pulse geometry.** The geometry and parameters of Equation 2.21.

TGF production create emissions far above the thundercloud, at altitudes 30–50 km, as expected. However, the intensity of the emissions only agrees with satellite observations if the source lightning displaces at least 250 C by at least 10 km (as discussed in *Lehtinen et al.*, 2001). Such charge moment changes above 2500 C km are extremely large, a factor of 5 larger than even extremely intense observed lightning (for example, see *Cummer and Lyons*, 2004). Therefore, while some TGFs may be due to such intense lightning discharges, other mechanisms must also be possible.

2.4.2 Electromagnetic pulse mechanism

Another possible electric field production mechanism, first proposed by *Inan and Lehtinen* (2005), is the electromagnetic pulse (EMP) produced by a lightning return stroke. Here the electric field is radiated by the rapidly-moving vertical current pulse and has the form

$$E(t) = \frac{\mu_0 I(t - R/c)}{2\pi R} \frac{v_c \sin \theta}{1 - \beta^2 \cos^2 \theta} \quad (2.21)$$

where $I(t)$ is the current in the channel, v_c is the velocity of the current front, $\beta = v/c$, θ is the zenith angle, and R is the distance from the source to the observation point as shown in Figure 2.11. This formula assumes a vertical current pulse at and just above a perfectly conducting ground plane. Such an electric field may as before drive RREA and TGF production at high altitudes. A schematic is shown in Figure 2.12.

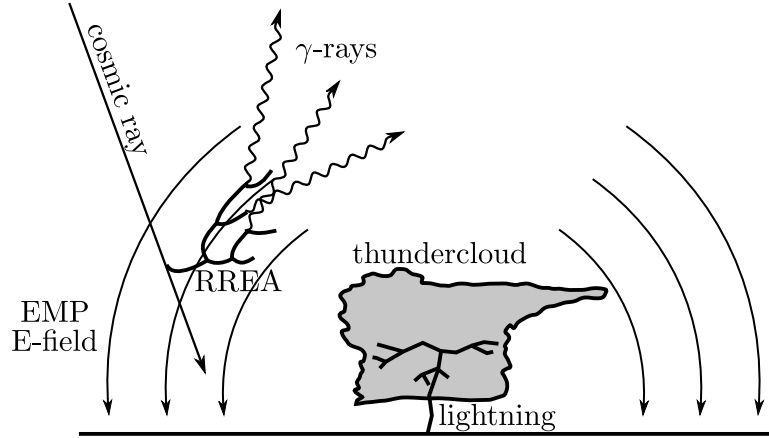


Figure 2.12: **Electromagnetic pulse TGF production mechanism.** An intense return stroke in a CG discharge radiates an electromagnetic pulse. In the presence of energetic electrons, here provided by cosmic rays, the radiated E-field drives RREA, producing bremsstrahlung photons.

The EMP mechanism of TGF production falls victim to much the same trouble as the QES mechanism. While the QES mechanism required extreme charge dipole moment changes, the EMP mechanism requires very high return stroke currents ($I_{\max} > 400 \text{ kA}$) and very high return stroke velocities ($v_c > 0.99c$) (*Inan and Lehtinen, 2005*). Typical return stroke velocities are $\sim 0.6c$; velocities much closer to the speed of light are very rare. *Inan and Lehtinen (2005)* also calculate the expected occurrence rate of high-current discharges regardless of velocity. They predict the global rate of discharges with sufficiently high current to be 6–12 per day. Though this is a nontrivial number and it is possible that some TGFs are produced by the EMP mechanism, the necessity of high return stroke velocity is not addressed and the mechanism still can only contribute a small fraction of the estimated global rate of 500 TGFs per day.

A related mechanism relying on the EMP produced by current pulses in intra-cloud discharges was suggested by *Milikh and Valdivia (1999)*, relying on fractal structures in intra-cloud discharge to amplify the effects of EMP. The authors argue that the

fractal structures should result in amplification of the electric field by a factor of ~ 5 by coherent summation of EMP emitted by different parts of the leader channel and claim that their mechanism produces TGFs with current pulses > 50 kA. While intriguing, the mechanism does not account for any realistic current structure in the lightning channel. Further, as described by *Inan and Lehtinen* (2005), *Milikh and Valdivia* (1999) neglected a factor of $4\pi^2$ in one of their equations, a correction which changes their current requirements from > 50 kA to > 2 MA, an unreasonably large value.

2.4.3 Summary of TGF production mechanisms

The two main theories of TGF production by quasi-electrostatic (QES) and electromagnetic pulse (EMP) electric fields rely on extreme source lightning processes to produce sufficiently strong electric fields. These mechanisms thus fall short of explaining the observed TGFs.

The mechanisms have additional problems that are examined in more detail in Chapters 3 and 4. First, both mechanisms predict emissions from high altitudes. As discussed in Section 3.2.1, this prediction does not match the average observations of TGFs, though this was not known when the mechanisms were constructed. The QES and EMP mechanisms also involve various assumptions about the nature of the source of RREA seed electrons. For instance, the EMP mechanism described in *Inan and Lehtinen* (2005) assumes seed electrons produced by showers of secondary particles from single primary cosmic rays with primary energies from 10^{16} – 10^{18} eV. As discussed in Section 4.4, this assumption is not reasonable and the seed flux becomes a limiting factor. These facts are explored in detail in the subsequent chapters.

Chapter 3

Constraints on source mechanisms

The terrestrial gamma-ray flash source poses a variety of questions. Fundamentally, the source and behavior of the driving electric field are the key questions. More practically, lower level questions are also posed, such as where the source is located and what is its initial energy.

However, even these more direct questions cannot be immediately answered. All that is known are the results of experiments, namely satellite observations of TGFs. In the context of the summary of TGF physics given in Figure 2.9, the satellite observations fall on the right end of the chain, while the most fundamental questions about the physics of TGF production fall on the left. Examination of satellite data to determine the properties of the TGF source therefore poses an inversion problem. Given enough information toward the left half of Figure 2.9, the process can be followed to the right to predict the satellite observations, but the satellite observations themselves do not immediately allow inference of the nature of the processes at the left in Figure 2.9.

This chapter describes a solution to this inversion problem by Monte Carlo simulation of the forward process. A source of photons is assumed and the resulting

satellite observations are simulated. Comparison of the simulation results to the actual satellite data allows assessment of the assumed photon source. Results that do not match the satellite observations can be used to rule out the particular assumptions used and thus constrain the TGF photon source. In particular, the results of this chapter constrain the average TGF production altitude, energy, and the initial angular distribution of TGF photons.

3.1 Monte Carlo simulations

The starting point for the simulations of TGF physics discussed in this chapter is taken to be the emission of photons. This removes the electric field production mechanism from consideration, greatly simplifying the inversion problem. Though this limits the results to constraint of the photon source, such results are very useful as they can be used to assess the validity of various photon production mechanisms.

As the goal is to study the photon source by comparing its effects to satellite data, the assumed photon source should be taken to vary over as wide a range as possible. Some overarching assumptions are necessary to limit the search, however. To render the number of possible photon sources tractable, only point sources are considered. This removes the complexity of the 3-dimensional shape of the photon source while complicated shapes can be built by superposition of such point sources if required. The altitude of the point source is taken to fall within 10–70 km. Sources lower than 10 km do not radiate significantly to satellite altitude, while the atmosphere above 70 km is too tenuous to produce a sufficient amount of bremsstrahlung.

Two initial photon energy spectra are considered. The first spectrum is that due to thin-target bremsstrahlung produced by RREA electrons with energy spectrum given in *Lehtinen et al.* (1999). The bremsstrahlung is generated by Monte Carlo simulation with the GEANT4 software package (*Agostinelli et al.*, 2003). This is the

most realistic case, referred to as the bremsstrahlung initial spectrum hereafter. The bremsstrahlung initial spectrum is similar to that used in *Dwyer and Smith (2005)* and allows for comparison of results. The second spectrum is divorced from the mechanics of photon emission and is the hardest spectrum producible by energetic electrons: $dN/d\mathcal{E} \propto 1/\mathcal{E}$, where $10 \text{ keV} < \mathcal{E} < 10 \text{ MeV}$. This limiting case is motivated by the fact that the observed TGF spectrum is quite hard and is referred to as the $1/\mathcal{E}$ case hereafter. Softer input spectra may be possible, but as the bremsstrahlung initial spectrum is characteristic of energetic electrons driven by electric fields in air, a substantially softer initial spectrum would likely require a mechanism inconsistent with the general physical principles discussed in Chapter 2.

The initial directional distribution of the photons is chosen to be uniform with zenith angle $\theta < \theta_m$. θ_m is taken to be either 1° , 25° , 45° , or 90° . $\theta_m = 1^\circ$ corresponds to the beam width of bremsstrahlung from unidirectional 35 MeV electrons, $\theta_m = 25^\circ$ is characteristic of bremsstrahlung from RREA in a uniform electric field, and $\theta_m = 45^\circ$ or 90° are broader beams that might result from nontrivial electric field structure.

The initial photons chosen from these distributions are then simulated as they propagate in the Earth's atmosphere. The Monte Carlo simulation tools used here were written by Nikolai Lehtinen and are described in *Lehtinen et al. (1999)* and *Lehtinen (2000)*. The atmosphere in which the photons propagate is taken to have constant composition as a function of altitude with density taken from the MSIS model (*Hedin, 1991*). Photoelectric absorption, Compton scattering, and pair production are included with cross sections formulas similar to those given in Section 2.1.1. Pair production is treated simplistically, with the produced positron immediately giving rise to two oppositely-directed 0.511 MeV photons. As positron annihilation at rest is more likely than annihilation in flight, this is a reasonable assumption.

This Monte Carlo code gives good results for the range of photon energies relevant to TGFs. This can be validated by comparison to GEANT4, the industry-standard

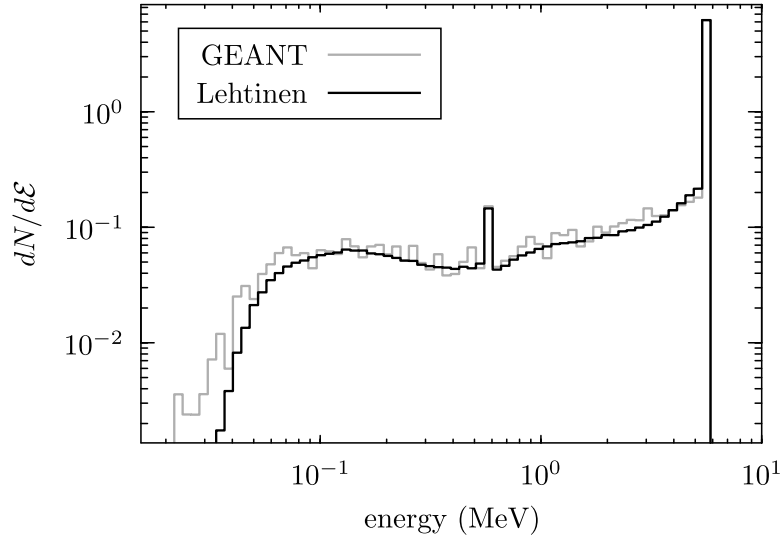


Figure 3.1: **Lehtinen Monte Carlo validation.** Comparison of photon energy spectra after interaction with 2 m of air in simulation of initial 5 MeV photons. GEANT4 shown in grey, *Lehtinen et al.* (1999) Monte Carlo shown in black. Overall fit is quite good with some deviation visible at low energies.

simulation package (*Agostinelli et al.*, 2003). A sample comparison plot of the energy distribution of photons produced after interaction of 5 MeV photons with 2 m of air at sea level density is shown in Figure 3.1. Plots of other distributions and other validation conditions give similar results.

The photons that escape the atmosphere are recorded and placed in bins by location in the horizontal plane at satellite orbital altitude (the “satellite plane”, here placed at 600 km altitude.) Sufficient statistics are ensured by simulating enough initial photons that at least 5×10^5 photons reach satellite altitude for each initial condition. The number of photons necessary to ensure this condition varies between 6×10^5 photons for high-altitude cases to 3×10^9 photons for low-altitude cases.

The resulting photons are then passed through the satellite detector response function to determine the spectrum of photons that would be observed. The detector response is stored as a matrix, with each row in the matrix representing the spectrum

that would be measured if a beam of photons of a particular energy was incident. This analysis is carried out both for RHESSI and for BATSE. The detector response matrices for BATSE are available in the Compton Observatory Science Support Center (COSSC) data archive (<http://cosscc.gsfc.nasa.gov>, `discsc_drm` files). The detector response matrices for RHESSI were provided by *Smith* (2006). The result is a set of possible observed spectra at various locations in the satellite plane.

The sensitivity of the satellite and the likelihood of detection of TGFs is then accounted for by consideration of the relative intensities observed, similar to the method used in *Dwyer and Smith* (2005). The most intense TGF observed by RHESSI is a factor of 5 more intense than the least intense TGFs observable by RHESSI. BATSE observes a similar ratio from most to least intense. Assuming that all TGFs have similar inherent brightness and that all variation in TGF observations is therefore due to observation of the TGF from various positions, the most intense TGF observations can be identified with the regions of the satellite plane where the spectra are most intense. Likewise, the least intense observed TGFs can be identified with the minimum sensitivity threshold for TGF detection. Those regions in the satellite plane where the simulated spectra are less than one fifth as bright as the most intense regions are therefore considered below the detection threshold and are discarded.

The remaining regions of the satellite plane, those with intensities within a factor of 5 of the most intense regions, are considered as possible TGF observations. These simulated observations contain spectra, relative intensity, and position information ready for comparison to satellite observations. The simulated spectra vary with position but are averaged together for comparison with the average spectra seen by the RHESSI and BATSE satellites. The number of photons simulated and the intensity of the simulated spectrum is also tracked for calculation of the total energy input necessary to produce simulated fluence that matches observations. The position associated with the simulated spectra and the resulting lateral displacement from the

photon source are also considered for comparison to the lateral displacements between lightning and sub-satellite point.

3.2 Satellite data comparison

3.2.1 Spectral comparison

Comparison of the simulated average spectra to the average TGF spectra observed by RHESSI and BATSE are shown in Figure 3.2.

The simulated spectra are very sensitive to the production altitude. The general trend is that the lower the initial altitude, the harder the observed spectrum. As such, the hardest possible input spectrum (the $1/\mathcal{E}$ case) should result in a strong upper limit to the average production altitude. The highest production altitude that results in a good fit for the $1/\mathcal{E}$ case is 20 km. This is in stark contrast to the existing theories discussed in Section 2.4 that resulted in higher production altitudes. One possible exception is the $\theta_m = 1^\circ$ case which seems to best fit at $\simeq 30$ km, but the overall fit for this case is poor so this case can be ruled out. The softer bremsstrahlung initial spectrum considered here conversely results in a slightly lower but not significantly different best fit altitude of 15–20 km. Overall, therefore, the best fit production altitude is 15–20 km. This is true for both the $1/\mathcal{E}$ and bremsstrahlung input spectra.

This production altitude range is consistent with *Dwyer and Smith (2005)*, who confined their analysis to the RHESSI data. The BATSE data show roughly the same picture, though the reduced spectral resolution (4 bins instead of 40) limits the usefulness of the BATSE data. The best fits for the BATSE data agree well with the best fits for the RHESSI data (low altitudes), but the best RHESSI fit is far better than the best BATSE fit. This is likely due to dead-time issues in the BATSE spacecraft, discussed further in Section 3.3.

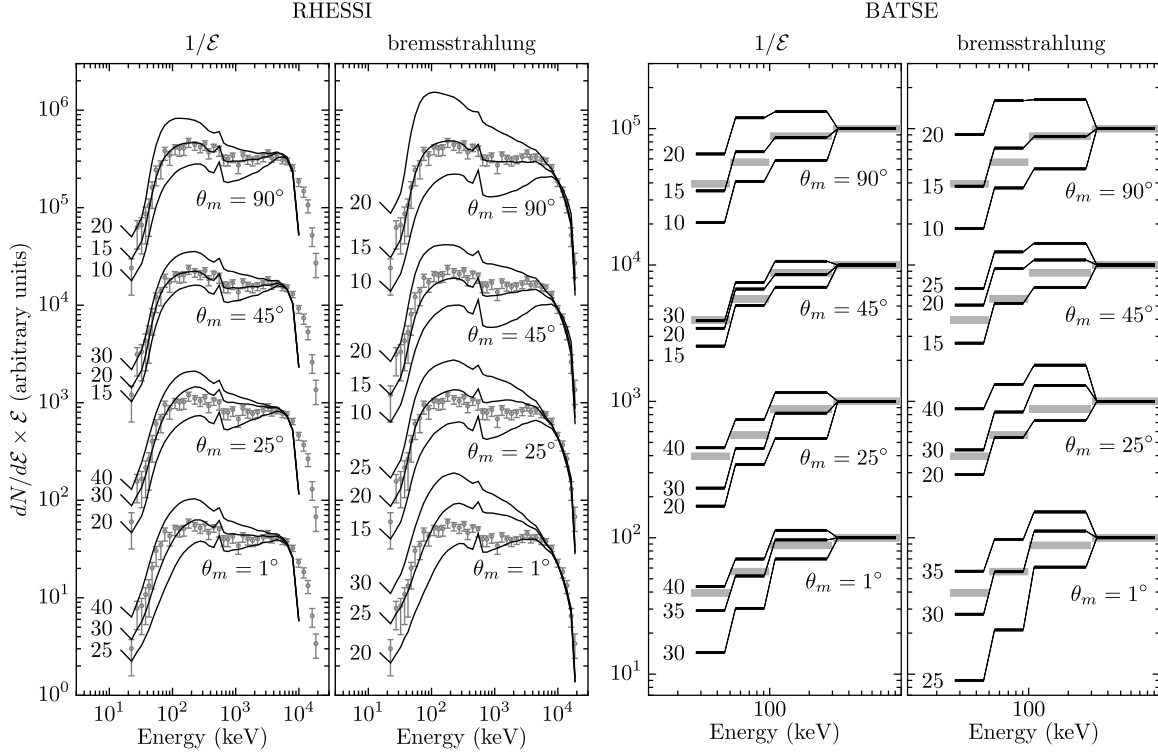


Figure 3.2: **Simulated and observed spectra.** Comparison of average spectra (grey) to simulation results (black curves) for various conditions for RHESSI (left) and BATSE (right). For each satellite, the left panel shows the $1/\mathcal{E}$ initial spectrum while the right panel shows the bremsstrahlung initial spectrum as indicated. For each spectrum, each group of curves is associated with a different initial directional distribution, labeled with θ_m . For each θ_m , the curves represent different initial altitudes, labeled at left in kilometers and are normalized to line up with the data near the high-energy end. The peak in the simulated RHESSI spectra at 511 keV is a feature of the detector response to high-energy photons due to pair production and positron annihilation in the satellite.

As mentioned above, the $\theta_m = 1^\circ$ case results in poor fits and can be discarded. $\theta_m = 25^\circ$ is also a relatively poor fit. The broader beams result in much better fits, with $\theta_m = 45^\circ$ best overall. The question of beaming is addressed further in Section 3.2.3.

The main visible difference between the $1/\mathcal{E}$ initial spectrum and the bremsstrahlung initial spectrum is the cutoff at high energies. As the $1/\mathcal{E}$ initial spectrum has an artificially sharp cutoff at 10 MeV this is not unexpected. The natural cutoff in the energy spectrum does fall near 10–15 MeV, however. This can be seen in additional simulations with a $1/\mathcal{E}$ initial spectrum with a cutoff at 20 MeV. These simulations show too many high-energy photons in the simulated spectra. The bremsstrahlung initial spectrum overall fits almost perfectly, including this high-energy cutoff, lending support to the expectation that TGF photons are produced by energetic electrons driven by electric fields in air.

The comparison of the spectral shape therefore constrains the average source altitude to 15–20 km, suggests $\theta_m \gtrsim 45^\circ$, and supports the idea of RREA and bremsstrahlung photon production.

3.2.2 Total source energy

The overall normalization of the simulated spectra provides information about the total energy required for the photon source. The most intense average spectra, passed through the detector response function, must be scaled by some factor in order to yield the number of photons observed in the most intense TGF (~ 100 for RHESSI, ~ 1000 for BATSE). The total energy of simulated photons, scaled by the same factor, gives the total energy required of the photon source. The same process can be repeated for the least intense simulated spectra and the least intense TGF.

The energy requirements depend on the altitude of the photon source and the initial directional distribution and are shown in Figure 3.3. The curves for RHESSI

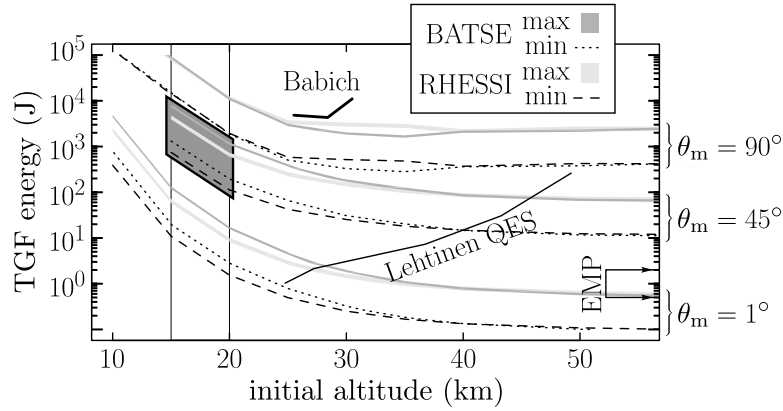


Figure 3.3: **Source energy requirements.** The source energy required to match satellite observations for various conditions is shown by the grey and black lines. The solid grey bars and black lines represent the energy required to match the most and least intense observed TGFs seen by the satellite as indicated in the key. Results are shown for different θ_m as indicated at right. The thin vertical lines and the dark grey box represent the best fit altitude from the spectral comparisons and the resulting energy requirements. The results of the QES mechanisms due to *Lehtinen et al.* (1999) and *Babich et al.* (2004b) and the EMP mechanism due to *Inan and Lehtinen* (2005) are indicated.

and BATSE overall agree quite well, though they do not exactly overlap due to the different detector response functions and the variability of the spectra with altitude and directional distribution.

The energy and altitude of peak production for the existing mechanisms discussed in Section 2.4 are also shown in this context. As mentioned above, though some of the existing mechanisms can produce observable emissions, this only occurs for unreasonably intense lightning and at altitudes higher than allowed by the spectral consideration in Section 3.2.1. As the best fit spectra indicate a source altitude of 15–20 km and $\theta_m \gtrsim 45^\circ$, the total energy required is at least 1–10 kJ, corresponding to a source population of 10^{15} – 10^{16} photons. Lower altitudes and broader beams require even higher energies.

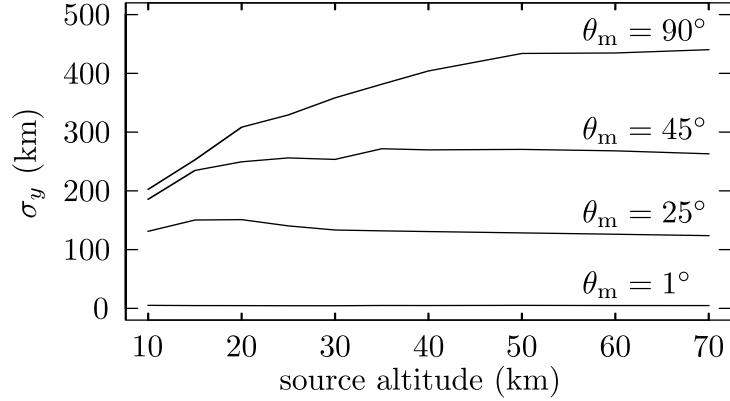


Figure 3.4: **Simulated lateral extent of TGF emissions.** The standard deviation σ_y of a lateral coordinate of the simulated observation locations vs. source altitude for various initial directional distributions labeled with θ_m .

3.2.3 Lateral spread

The lateral distribution of simulated satellite observations can be compared to the lateral deviation between subsatellite point and lightning as observed in the lightning studies described in Sections 1.2.2 and 1.2.4.

The typical lateral displacement in the satellite plane can be measured by the standard deviation of one of the coordinates associated with the above-threshold spectra in the satellite plane. This lateral standard deviation is shown in Figure 3.4.

The lateral distribution of measurements depends on the initial directional distribution and the source altitude but not significantly on the initial energy spectrum. For sources with large θ_m , the atmosphere effectively focuses the emissions into a narrower beam by attenuating photons emitted at large zenith angles as can be seen in the curves for $\theta_m = 45^\circ$ and 90° . For emissions with $\theta_m = 25^\circ$, the atmosphere partially scatters and partially focuses, depending on the altitude but the effect is not strong. The $\theta_m = 1^\circ$ case is so narrow that the peak intensity drops off very rapidly with distance from the peak, even for sources deep in the atmosphere.

The typical subsatellite-lightning distances observed in radio observations of lightning coincident to TGFs are typically < 300 km. For 15–20 km source altitudes as suggested by the spectral studies, this is consistent with the $\theta_m \gtrsim 45^\circ$, also in agreement with the spectral comparisons. Better statistics on subsatellite-lightning distance are required to further address this issue.

3.3 Caveats

The studies described above are only as good as the assumptions used. The most relevant assumptions are those that underlie the approximate treatment of the satellite detection threshold. The key assumption is that all TGFs have the same source properties and that all variation is due to the geometry of satellite observation. The natural variation in TGF intensities is unknown, and it may be the case that an observation of a TGF with relatively few photons is really an intrinsically dim TGF observed at its brightest as opposed to an intrinsically bright TGF observed from a relatively distant location. Studies involving nontrivial distributions in total initial photon energy would help understand this effect.

Similarly, it is unlikely that TGFs are produced at only one altitude or with only one effective θ_m . For instance, as mentioned in Section 2.4.2, it is possible that some TGFs are produced by the EMP mechanism at high altitudes. While this is true, the results here constrain the average TGF to be produced at relatively lower altitudes. Studies involving nontrivial distributions in initial conditions may be useful, but for the purposes of setting coarse constraints as is the goal here, the approach used should be sufficient.

One important limitation to the BATSE spectrum and intensity analysis is dead-time. The BATSE instrument was built with electronics that exhibit an energy-dependent paralyzable dead-time that is shown to significantly affect BATSE TGF

observations by *Grefenstette et al.* (2008). This dead-time can be quite significant ($> 50\%$) and contributes to an overall deficit in the total number of photons detected. As suggested in *Grefenstette et al.* (2008), the dead-time also contributes to a relative excess number of counts in the lowest-energy bin. As the most-energetic photons are unlikely to have been significantly scattered and thus tend to have more direct paths to the satellite and arrive sooner, the early photons at the peak brightness of the TGF tend to have higher energies while late photons tend to have lower energies. As a portion of the photons arriving during the peak brightness of the TGF are lost due to dead-time, relatively more low-energy photons are observed as seen in Figure 4 of *Grefenstette et al.* (2008). Consideration of this fact helps to explain the poor fits to BATSE spectra in Figure 3.2 but correspondingly limits the validity of the comparison.

3.4 Summary of TGF source properties

These results show good agreement with the coarse ideas of TGF production described in Chapter 2 if the photon source emits 1–10 kJ of energetic gamma-rays with a bremsstrahlung spectrum at 15–20 km altitude and the photons are emitted in a broad beam with effective half-angle $\theta_m \gtrsim 45^\circ$. These rough constraints are not dependent on the details of any particular production mechanism, though the requirement of photon emission by bremsstrahlung from electrons driven by electric fields is used to determine feasible initial spectra. These constraints suggest that though the QES and EMP production mechanisms may contribute some TGFs, the average behavior indicates a new mechanism is required. The results described in this chapter are available in the literature in *Carlson et al.* (2007).

Chapter 4

Electron avalanche seeding

The runaway relativistic electron avalanches suggested as crucial to TGF production require seed runaway electrons to start the process, a fact first discussed in Section 2.2.1. In the Earth's atmosphere, these seed particles likely come from cosmic rays. These statements raise more questions than they answer, however. For example, do populations of such RREA seeds arrive all at once due to single relatively energetic cosmic rays, or do they maintain a steady flux due to many lower-energy cosmic rays? How does the seed population vary from one moment to the next? Furthermore, how exactly do cosmic rays produce seeds? This chapter answers these questions by consideration of cosmic ray physics and studies of the detailed physics of RREA seeding.

4.1 Cosmic rays

Cosmic rays are the most energetic particles ever observed, with energies that sometimes exceed 10^{20} eV (*Nagano and Watson, 2000*), as much energy as a thrown baseball in a single atomic nucleus. Though little is known about their origins, results from the Pierre Auger observatory suggest exotic astrophysical phenomena such as

active galactic nuclei (*Abraham et al.*, 2008). An interesting subject in their own right, cosmic rays have been extensively studied since the early 20th century. A complete review of cosmic ray physics is beyond the scope of this dissertation. Reviews can be found in *Nagano and Watson* (2000) and *Sokolsky* (1989). Here it suffices to list the properties of cosmic rays and describe their interactions with the Earth’s atmosphere.

Cosmic ray particles themselves come in a wide range of energies. Overall, the energy distribution is approximately

$$\frac{dN}{d\mathcal{E}} \propto \frac{1}{\mathcal{E}^3} \quad (4.1)$$

where N is the number of cosmic rays and \mathcal{E} is the energy. This power law proportionality holds reasonably closely from $\mathcal{E} = 10^{10}$ eV to 10^{20} eV with slight changes in slope at $10^{15.5}$ eV (the “knee”) and 10^{19} eV (the “ankle”). In the energy range where cosmic rays are numerous enough to directly detect, the particles are almost always protons, with approximately 10% helium nuclei and a small fraction ($\lesssim 10^{-3}$) heavier nuclei. Despite much effort to show the contrary, energetic cosmic rays seem to bombard the Earth completely uniformly in time, space, and direction.¹ Lower-energy cosmic rays ($\mathcal{E} \lesssim 10^9$ – 10^{10} eV) are deflected by the geomagnetic field and do not reach the Earth, the so-called geomagnetic cutoff.

Cosmic rays with enough energy to reach the Earth collide with atoms in the atmosphere and produce a cascade of secondary particles called an air shower. A sample cosmic ray shower is shown in Figure 4.1. This shower of secondary cosmic rays grows in part by the electromagnetic shower process described at the beginning of Section 2.2 and in part by similar processes involving hadronic interactions, the hadronic shower. At the start of an air shower, the hadronic shower contains the

¹Much cosmic ray literature is devoted to such anisotropy and correlation studies, including, shamelessly, *Carlson et al.* (2005), the author’s first paper.



Figure 4.1: **Sample cosmic ray air shower.** The primary cosmic ray proton enters from the top and collides with particles in the atmosphere to produce a shower of secondary particles that grows exponentially until their energy decreases and they can produce no more energetic secondaries. Plot shows simulation results from AIRES.

bulk of the energy but then gradually fuels the electromagnetic shower. The numerical majority of the secondary particles are particles in the electromagnetic shower and long-lived remnants of the hadronic shower: photons, electrons, positrons, and muons.² Sample distributions of cosmic ray secondaries are shown in Figure 4.2.

4.1.1 Cosmic ray air shower simulations

The physics of the energetic particle interactions in a cosmic ray air shower are complex. Though crude analytical treatments exist, Monte Carlo simulations on the basis

²Muons are a relatively long-lived product of the decay of short-lived pions produced in the hadronic shower ($\pi^- \rightarrow \mu^- + \nu_\mu$).

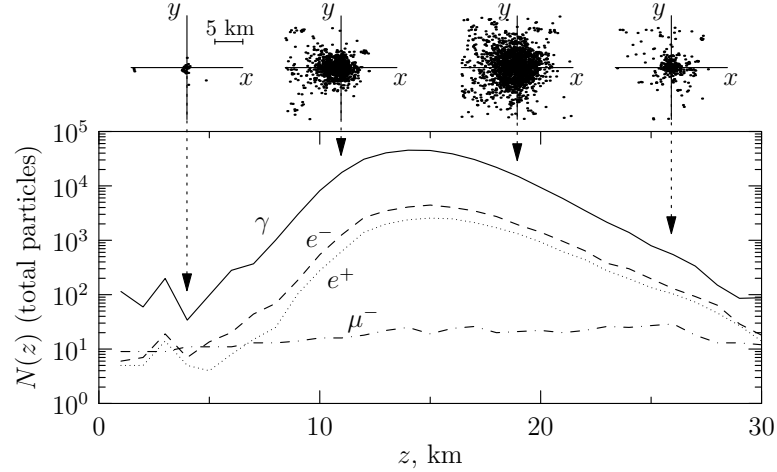


Figure 4.2: **Sample air shower secondary distributions.** The number of photons, electrons, positrons, and muons is shown as a function of altitude in the main panel. Sample secondary particle lateral position distributions are shown above on a ± 10 km scale for 4, 11, 19, and 26 km altitudes. Data shown are AIRES simulation results for an air shower produced by a 10^{13} eV proton incident on the Earth’s atmosphere with a zenith angle $\theta \simeq 70^\circ$ ($\cos \theta = 0.35$).

of descriptions of individual particle interactions are commonly used. There is unfortunately some uncertainty in the models used to drive such Monte Carlo calculations, especially in the hadronic shower, but overall it is well-accepted that such models agree well with observations.

The simulations described in this chapter use the AIRES software package (*Sciutto*, 2002). AIRES is an advanced cosmic ray air shower simulation tool developed by the Universidad Nacional de La Plata in Argentina. The version of AIRES used here uses SIBYLL (a minijet model of hadronic processes) for simulation of hadronic interactions, though AIRES also includes QGSJET and QGSJET-II (quark-gluon string models.)

As cosmic ray air showers often contain too many secondary particles to feasibly run simulations, AIRES implements a “thinning” algorithm whereby some low-energy products of an interaction are ignored and the remaining low-energy products are

propagated as usual but with increased statistical weight. Fortunately, as discussed later in this section, the highest-energy cosmic ray air showers for which computation is prohibitively slow are not required here, so all simulation results reported are “unthinned.”

4.1.2 Overall cosmic ray secondary distributions

From the perspective of seeding RREA, the interesting question is what are the distributions of cosmic ray secondaries in the electric field region? This reduces to a determination of what cosmic ray primary particles are relevant, the properties of these primary particles, and the properties of the secondary particles they contribute.

The starting point, however, is to consider a region of interest. The electric fields relevant to TGF production must be roughly vertical and cover a large potential difference and therefore must have significant vertical extent. The horizontal extent is in principle unconstrained but here is assumed to be the same as the vertical extent. The regions of interest considered are therefore spheres with radius chosen to range from 100 m to 3 km. Also relevant is the timescale over which the electric field exists. The light travel time over the region of interest is used here to focus on the initiation of the avalanche before significant growth occurs. These regions of interest are taken to fall at altitudes from 0 to 30 km, including the range of TGF production altitudes allowed by the constraints discussed in Chapter 3.

The energies of cosmic ray primaries relevant to these regions of interest can then be determined. The largest cross sectional area and timescale under consideration are $28 \times 10^6 \text{ m}^2$ and $10 \mu\text{s}$. As the flux of cosmic rays with energies above 10^{15} eV is $\simeq 1 \text{ m}^{-2} \text{ year}^{-1}$, the expected number of such cosmic rays incident on the largest region of interest within the timescale in question is $\simeq 10^{-5}$. This therefore represents a reasonable upper limit on the highest energy cosmic ray primary expected to be relevant to the regions of interest considered. As mentioned above, cosmic rays with

energies below 1–10 GeV are deflected by the geomagnetic field. Such cosmic rays also do not produce sufficiently large air showers to significantly affect the altitude range in question. The energy range of cosmic ray primaries considered here is therefore 10^9 – 10^{15} eV.

The question then becomes what sort of secondaries do these cosmic ray primaries contribute? This depends on the direction from which the cosmic ray primary arrives (the zenith angle) and where the cosmic ray air shower intersects the region of interest. As there are many possible ways these interactions can occur, it is useful to construct a library of such interactions in place of direct computation of the full air shower process every time secondary particle information is needed.

The library of cosmic ray air showers used spans $10^9 \leq \mathcal{E} \leq 10^{15}$ eV energies, uniformly in $\log \mathcal{E}$, with 4 steps per decade (25 distinct energies). Simulations are carried out at zenith angles uniformly spaced in $\cos \theta$ from $\cos \theta = 0.05$ to $\cos \theta = 0.95$ in steps of 0.1 (10 distinct angles). At each of these conditions, at least 5 cosmic ray air showers are simulated, with up to 20 simulations carried out for the more common lower energy showers. The results of these simulations are stored as multidimensional histograms in secondary particle type, energy, direction, and position. These distributions thus catalog the secondary particles produced by the primary energies and zenith angles relevant to the regions of interest under consideration.

The secondary particles contributed to the region of interest can then be calculated. This is done with a small Monte Carlo simulation where random cosmic ray primary energies are drawn from the known cosmic ray primary energy distribution taken from *Wolfendale* (1973) and *Nagano and Watson* (2000). The zenith angles are drawn uniformly in solid angle (i.e., uniformly in $\cos \theta$). The locations of the shower cores with respect to the region of interest is drawn uniformly over an external region 5 km larger in radius than the region of interest. This external region allows the edges of air showers whose cores miss the central region of interest to contribute particles

to the central region. As even very energetic cosmic ray air showers do not contribute significantly many particles more than 5 km from the shower core, this external region is sufficiently large. The number of primary particles to draw is itself drawn from a Poisson distribution with mean given by the total cosmic ray primary flux integrated over the area of the external region, the energy and solid angle range spanned by the library, and the timescale in question. The air shower secondary distributions associated with these random primary particles are then retrieved from the library by choosing a random simulation result for the nearest primary energy and zenith angle. The secondary particle distributions are then integrated over the region of interest accounting for the randomly-chosen displacement of the shower core to give the overall distribution in particle type, energy, and direction of cosmic ray secondaries that intersect the region of interest within the timescale in question. If this process is repeated, the results will vary due to the random choice of number of primaries, primary energies, zenith angles, core locations, and specific simulation results. Repeating this process many times therefore gives the distribution of distributions of secondaries.

Sample results for the overall distribution of cosmic ray secondaries incident on the region of interest are shown in Figure 4.3. In particular note the distribution over many trials of the total number of particles at a given altitude. The distribution is fairly sharply peaked but has a tail to large particle counts. This indicates the occasional incidence of a relatively high-energy cosmic ray directly in the region of interest.

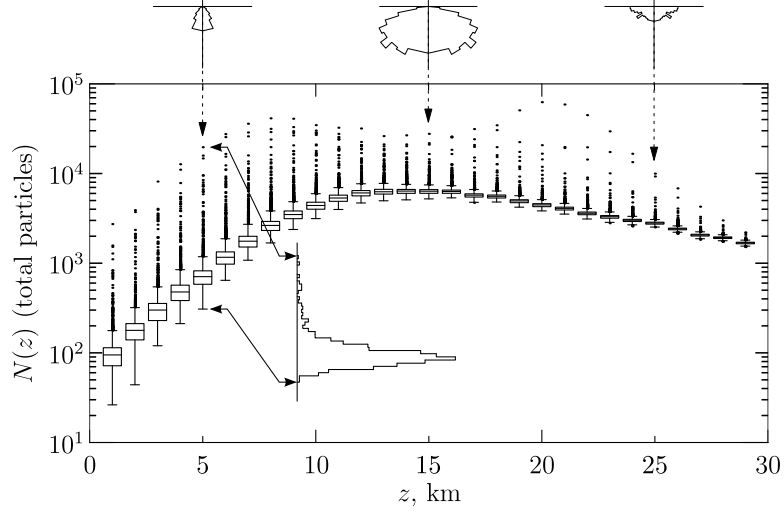


Figure 4.3: **Sample overall secondary distributions in region of interest.** The total number of particles integrated over energy, direction, and particle type is shown vs. altitude of the center of a 300 m radius region of interest. The distributions over 1000 trials are shown with box-whisker plots with outliers shown as dots. The actual distribution over trials for a region of interest at 5 km is shown in the inset. Sample directional distributions for 5, 15, and 25 km are shown above in polar form (radius represents $dN/d\Omega$). Box-whisker plots are standard with minimum/ Q_1 /median/ Q_3 /maximum represented by the box and whiskers where Q_1 and Q_3 are the first and third quartiles. Outliers are shown with dots and are defined as falling more than $1.5(Q_3 - Q_1)$ from the median and are excluded from identification of the maximum and minimum.

4.2 Runaway relativistic electron avalanche seeding efficiency

Knowing the distribution of cosmic ray secondary particles in the region of interest, the efficiency of those secondaries at seeding RREA can be calculated. This is done with Monte Carlo simulations of the initial phases of avalanche growth and comparison of the results to standard conditions.

The incidence of an energetic particle on a region with an electric field may not produce RREA or may produce varying degrees of RREA depending on the energy,

direction, and type of the incoming particle. For instance, it is reasonable to expect that energetic photons are not as good at seeding RREA as energetic electrons, and that electrons moving in the direction of avalanche motion are better than electrons moving opposite the avalanche.

These effects can be assessed by Monte Carlo simulation with the GEANT4 package (*Agostinelli et al.*, 2003). In order to focus only on the seeding process without losing information in the details of avalanche growth, specific time limits are imposed on the simulations. The incident particle (the putative cosmic ray secondary) is only simulated for 100 ns. This allows the incident particle enough time to interact and produce energetic secondaries but limits other effects such as energy gain or loss in the electric field. To allow for a standard small amount of avalanche growth, the energetic secondary particles produced by the incident particle, together with any other secondary particles produced, are tracked for up to 20 ns after the parent incident particle interaction. The particles are injected into an electric field 1.5 times the RREA threshold field ($E = 1.5E_{\text{RREA}}$). Sample electron production results of this process are shown in Figure 4.4.

The total number of electrons that reach the end of their allowed lifetime is taken to be a measure of the efficiency of RREA seeding of the incident particle. However, this number of electrons bears little physical insight as it depends on the time limits used and thus must be compared to the number of electrons produced under standard conditions to extract the relative seeding efficiency. The “standard” seed particle is a typical avalanche particle: a 1 MeV electron (near the energy for minimum frictional losses) traveling in the direction of avalanche growth. The number of electrons produced by this particle under the conditions of the simulation can be used as a normalization to convert other seed conditions to the effective number of 1 MeV electrons moving with the avalanche, i.e. the effective number of RREA seed particles.

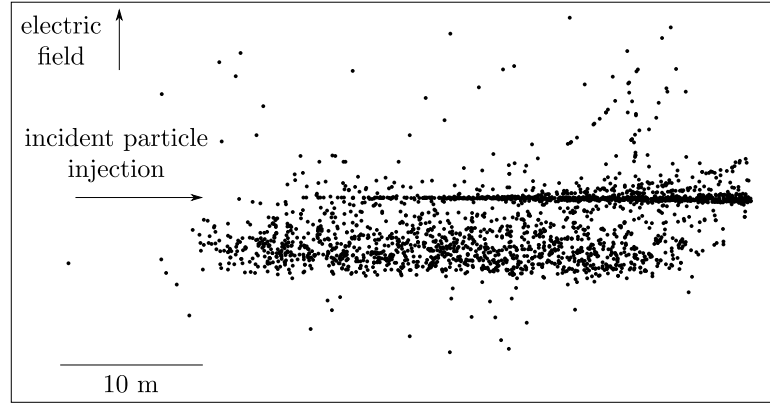


Figure 4.4: **Sample RREA seed production.** Monte Carlo simulation results showing electron positions after injection of 10 MeV electrons perpendicular to the electric field at sea level. The cloud of particles towards the bottom are RREA avalanches growing under the influence of the electric field, the electromagnetic shower produced is visible expanding to the right. The path of a positron is also visible by the occasional production of electrons as it propagates upward driven by the field.

This effective seeding is shown for various conditions in figure 4.5. Several features can immediately be identified. First, low-energy electrons do not function as seed particles. This is the fact mentioned in Section 2.2.1 that RREA requires energetic seed particles. Second, high-energy electrons, positrons, and muons all behave very similarly in this analysis. If long time limits were used, extensive showers would develop and energetic particles would behave differently, but for the purposes of the initial phase of RREA seeding similar behavior results. Third, note that low-energy positrons and muons can function as seeds. This is due to positron annihilation ($e^+ + e^- \rightarrow 2\gamma$) and muon decay ($\mu^- \rightarrow e^- + \bar{\nu}_e + \nu_\mu$). In both cases, the products have sufficiently high energy to produce RREA seed electrons. Finally, the direction of the incident particle provides a significant effect. Energetic electrons moving with the avalanche are ~ 2 times better seed particles than electrons moving against the avalanche. As cosmic ray secondary particles tend overall to travel downwards while avalanches that would produce bremsstrahlung visible from satellites tend to travel

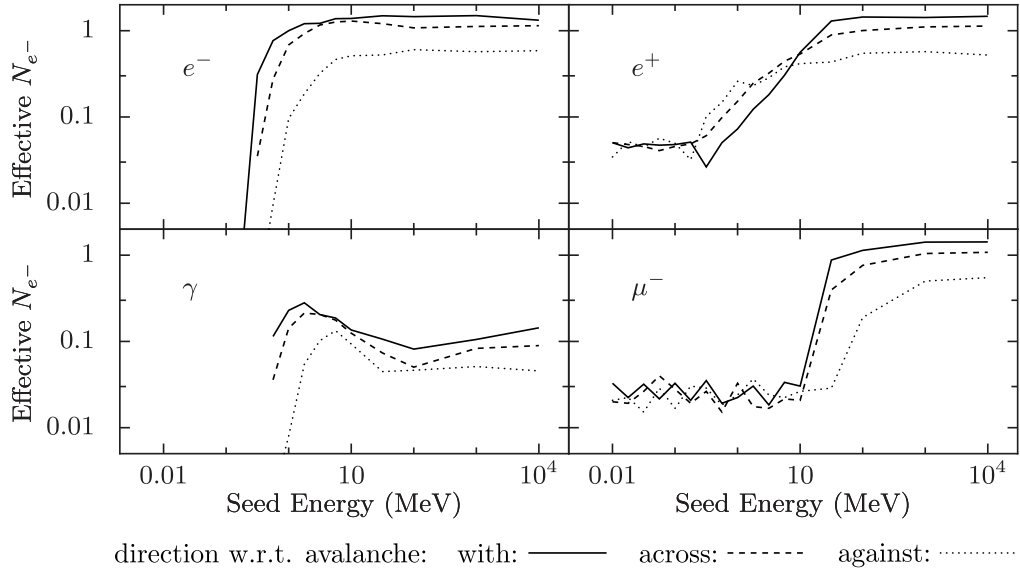


Figure 4.5: **Seeding efficiency.** Effective seeding as described in the text shown for electrons (e^-), positrons (e^+), photons (γ), and muons (μ^-) as a function of energy and direction as indicated.

upwards, this effect may be important.

4.3 Overall seed population

The results of effective seeding efficiency shown in Figure 4.5 can then be combined with the overall distributions of cosmic ray secondaries in the region of interest as shown in Figure 4.3. This calculation is a simple matter of multiplying the number of particles with given properties by the seeding efficiency numbers corresponding to those properties and calculating the sum over all properties. The result is the effective seed population size relevant to the region of interest and timescale in question, as shown in Figure 4.6.

At low altitudes, the cosmic ray secondary flux is changing rapidly due to increasing atmospheric depth, so regions of interest with large radius acquire more seed

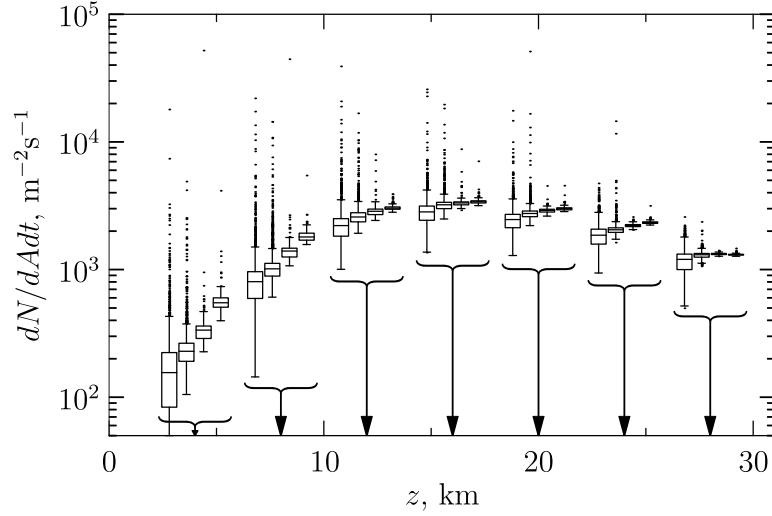


Figure 4.6: **Effective seed flux.** Effective seed flux shown as a function of altitude for the regions of interest considered here. 4 regions of interest are shown at several representative altitudes. At each altitude, the regions of interest are grouped by curly braces and from left to right are 100 m / 0.3 μ s, 300 m / 1 μ s, 1 km / 3 μ s, 3 km / 10 μ s. The results are shown for 1000 trials with box-whisker plots as described in the Figure 4.3 caption.

particles as the spherical region extends up to higher altitudes. The median seed flux peaks for altitudes around 15 km at $3 \times 10^3 \text{ m}^{-2} \text{ s}^{-1}$, corresponding to a seed population of 3×10^6 for a region of interest of size 1 km^2 present for 1 ms. The fluctuations in the seed flux depending on the particular cosmic ray primaries that contribute are large, occasionally more than an order of magnitude greater than the mean.

4.4 Implications

These analyses have direct relevance to several ideas in TGF theory, including the timescale of TGF emission and the relevance of ultra-high-energy cosmic rays (UHE-CRs).

The timescale of TGF emission is determined directly by the timescale of the

energetic electron population that emits the TGF via bremsstrahlung. The median seed flux numbers show that seed particles are always present, even for small regions of interest in short intervals of time. For example, at 15 km altitude, the 100 m radius region of interest receives approximately 10^4 effective seed particles every 100 μs . Essentially, as soon as the electric field exists, seed particles are present and RREA will occur. The timescale of RREA therefore tracks the timescale of the electric field, and if RREA growth alone is sufficient to produce detectable emissions, the TGF timescale and the electric field timescale should be similar.

The relevance of ultra-high-energy cosmic rays (UHECRs) to RREA seeding is contained in this analysis in the size of the fluctuations in the effective seed flux. As the flux of UHECR primary particles is very low (integral flux above 10^{15} eV is less than $1 \text{ m}^{-2} \text{ year}^{-1}$), the electric field must cover a large region if it is to catch a UHECR and the large numbers of secondary particles it produces. However, examination of Figure 4.6 shows that as the region of interest gets larger, the size of the fluctuations decreases. This is due to the increase in the number of lower-energy cosmic rays that intersect the region of interest as the area increases. In essence, though large areas are more likely to catch UHECRs, the increased flux of UHECRs is outweighed by the increased flux of lower-energy cosmic rays such that the fluctuations are damped out. This implies that UHECRs are not relevant in the context of seeding RREA, and that the assumptions made in particular by Gurevich of single UHECR air showers serving as seed particles are not valid without justification³ (*Gurevich and Zybin*, 2004; *Gurevich et al.*, 2004; *Gurevich et al.*, 2002, 2004b, 2003). A similar conclusion is reached by *Dwyer* (2007) by consideration of relativistic feedback limits on the size of the electric field region, a topic discussed in more detail in Section 5.5.

³Selection effects where fluctuations so rare as to be completely negligible in this analysis nevertheless dominate the observable behavior may be relevant, but such effects are not considered in existing mechanisms. These results indicate that claims of such behavior require very careful consideration.

In summary, initial RREA seed particles originate from cosmic rays, with the majority of seed particles contributed by a large population of relatively low-energy cosmic rays. The median seed flux is nontrivial, capable of seeding RREA whenever a sufficiently-large electric field is present. The fluctuations in this median seed flux are large, but not large enough to allow assumption of seed production by single ultra-high-energy cosmic ray air showers. The results described in this chapter are available in the literature in *Carlson et al.* (2008).

Chapter 5

Lightning and TGF production

The results derived in Chapters 3 and 4 pose a contradiction. The constraints on source altitude and total photon source energy from Sections 3.2.1 and 3.2.2 indicate a source of 10^{16} photons. Simulations of bremsstrahlung photon production such as those executed with GEANT4 to construct the RREA initial spectrum used in Chapter 3 indicate that production of such a population of photons requires a population of electrons ~ 10 times larger, i.e., 10^{17} total energetic electrons.

The largest seed population justifiable on the basis of the results in Chapter 4 is $\sim 10^7$. A population of 10^{17} energetic electrons as produced by RREA from a seed population of 10^7 electrons therefore requires a RREA avalanche growth factor of $\mathcal{M} \simeq 10^{10}$.

Equation 2.17, reproduced here without the parameter uncertainties, can be used to calculate the RREA avalanche growth factor \mathcal{M} :

$$\lambda(E) = \frac{7300 \text{ kV}}{E - 276 \text{ kV/m}} \quad (5.1)$$

$$\mathcal{M} = \exp \frac{L}{\lambda(E)} \quad (5.2)$$

$$= \exp \left[L \left(\frac{E - 276 \text{ kV/m}}{7300 \text{ kV}} \right) \right] \quad (5.3)$$

$$= \exp\left(\frac{U - L276 \text{ kV/m}}{7300 \text{ kV}}\right) \quad (5.4)$$

$$\mathcal{M}_{\text{max}} = \exp\left(\frac{U}{7300 \text{ kV}}\right) \quad (5.5)$$

where L is the length of the electric field region, $U = LE$ is the total available voltage, and \mathcal{M} is maximized at fixed U when $L \rightarrow 0$. As observed in Section 2.3.3, the maximum thunderstorm potential available is typically $U \simeq 100 \text{ MV}$. Equation 5.5 therefore gives $\mathcal{M}_{\text{max}} = \exp(100 \text{ MV}/7.3 \text{ MV}) \simeq 10^6$, a factor of 10^4 less than the $\mathcal{M} = 10^{10}$ required to produce an observable TGF. Though it is possible that maximum thunderstorm potentials exceed 100 MV, it is unlikely that the entire potential in the thunderstorm is focused on a region where the electric field exceeds E_{RREA} sufficiently to reach such large growth factors, especially given the assumption that $L \rightarrow 0$ in the above derivation of \mathcal{M}_{max} at sea level.

If RREA growth of seed populations produced by cosmic ray air showers is insufficient to properly account for TGF observations, new ideas are clearly required. One such idea is relativistic feedback as put forth by *Dwyer* (2003) and expanded on in *Dwyer* (2007). Relativistic feedback is discussed further in Section 5.5. This chapter puts forth and develops another idea that avoids the limitations on cosmic ray seeding while naturally providing an electric field source by consideration of lightning physics.

As discussed in Section 2.3.3, lightning involves hot conducting plasma channels (leaders) that allow charge redistribution in the cloud. The extension of the plasma channel occurs via corona discharge heating in the intensified electric field near the leader tip. The electric field intensification near the leader tip and in streamer tips in the associated corona discharge suggests that the electric field may be strong enough to itself accelerate low-energy electrons into the runaway regime (cold runaway) (*Moss et al.*, 2006; *Gurevich et al.*, 2007). These relatively low-energy runaways may then be accelerated and undergo RREA in the electric field of the leader.

5.1 Leaders as a RREA seed source

Consideration of the frictional force on energetic electrons in air as in Figure 2.3 and the associated discussion (Section 2.2.1) gives the peak frictional force and therefore the electric field necessary to overcome the peak frictional force as $E_c \simeq 25 \text{ MV/m}$. Such electric fields are impossible to sustain in air as they exceed the dielectric breakdown strength ($E_k \simeq 3 \text{ MV/m}$). Such fields can be attained, however, on short length and timescales such as those existing in the intensified fields near streamer tips.

Moss et al. (2006) discusses such electric fields in streamer tips in the context of a detailed Monte Carlo model of low-energy electron behavior in air. Including diverse relevant processes¹ allows simulation of populations of low-energy electrons in a simple model of the electric field of a streamer. The results indicate that such streamers do indeed produce runaway electrons. Calculations of the rate of runaway electron production in the streamer discharge regions associated with active extending lightning leaders give 10^{18} runaway electrons per second (*Moss et al.*, 2006, p. 32).

The same idea is explored in *Gurevich et al.* (2007) by solving the Boltzmann equation. Making suitable approximations with a crude model of the lightning leader electric field, *Gurevich et al.* (2007) arrives at a flux of runaway electrons of 10^{19} per second produced during the leader extension process.

The presence of energetic electrons in discharges can also be observed experimentally. Laboratory experiments searching for gamma-ray emission by spark discharges find such gamma-rays with energies up to 100 keV, clear evidence for the existence of electrons with energies in the runaway regime (*Rahman et al.*, 2008; *Nguyen et al.*, 2008; *Dwyer et al.*, 2008). Lightning leaders also produce such radiation as observed in experiments with natural and rocket-triggered lightning (*Dwyer et al.*, 2003; *Dwyer*

¹For example, collisional excitation of specific oxygen electronic transitions. E.g., $e + \text{O}_2 \rightarrow e + \text{O}_2(c^1\Sigma_g^+)$, one of 18 $e + \text{O}_2 \rightarrow \dots$ processes listed in Table 2 of *Moss et al.* (2006)

et al., 2004; *Howard et al.*, 2008; *Dwyer et al.*, 2005). The gamma-ray emission observed in these experiments occurs in short bursts when the discharge is most active. This result is consistent with the suggestion in *Moss et al.* (2006) that only active lightning leaders can produce runaway electrons.

These theoretical and experimental results clearly show that energetic electrons are produced by lightning leaders. The theoretical results even compare favorably with the 10^{17} runaway electrons required to produce bremsstrahlung observable as a TGF. If the runaway electron fluxes given by *Moss et al.* (2006) and *Gurevich et al.* (2007) are maintained by active leader systems for the 1 ms timescale of TGF emission, 10^{15} – 10^{16} runaway electrons will be produced.

Note also that in consideration of seed runaway electrons produced by the leader channel itself, the avalanches produced by these seeds only have a chance to grow if the leader is of negative polarity. RREA also occurs in the vicinity of positive leaders, but the seed electrons must originate away from the leader and thus require a secondary seed source, leading to the same problems of limited avalanche growth mentioned at the beginning of this chapter.

5.2 Leaders as an electric field source

Given the production of 10^{15} runaway electrons near a negative lightning leader, TGF emission still requires RREA multiplication of roughly $\mathcal{M} \simeq 100$ to produce the 10^{17} energetic electrons necessary for observable TGF production. These electrons also must be accelerated to sufficiently high energies, requiring a nontrivial voltage source. The effects of the electric field near the leader channel therefore must be considered.

The typical linear charge density of 1 mC/m on a leader channel as inferred from electric field change measurements (*Rakov and Uman*, 2003, pp. 123–126, 330–331)

suggests a simple line charge model, $E = \Lambda/(2\pi r\epsilon_0)$, where Λ is the linear charge density. However, the singularity in electric field strength at $r \rightarrow 0$ is unrealistic. Not only does the lightning channel have nonzero radius, but any charge deposited on the channel rapidly migrates away as corona and streamer discharge until the electric field falls below some critical value.

How exactly this process occurs in lightning is not well-understood. The simple model used here is to consider uniform charge density throughout a cylindrical volume of radius r_0 :

$$E(r) = \begin{cases} \frac{\Lambda}{2\pi r_0^2 \epsilon_0} r & \text{if } r < r_0 \\ \frac{\Lambda}{2\pi r \epsilon_0} & \text{if } r \geq r_0 \end{cases} \quad (5.6)$$

The radius r_0 is chosen such that the electric field never exceeds a threshold electric field strength: $r_0 = \Lambda/(2\pi\epsilon_0 E_{\text{th}})$. Here, E_{th} is taken either to be the conventional breakdown threshold E_k , the negative streamer propagation threshold E_{cr}^- , or the positive streamer propagation threshold E_{cr}^+ . Typical values of r_0 are 1–10 m. Such line charge fields limited by the maximum field strength are hereafter referred to as limited line charge fields. A sample limited line charge electric field and the corresponding electric potential are shown in Figure 5.1. Though the actual charge dynamics are certainly more complicated and the finite length and tortuosity of the lightning channel limit the validity of the infinite line charge approximation, the overall behavior of such electric fields over a range of limiting field values captures the possible behavior of the leader channel. Limited line charge fields with $E < E_k$ are representative of intense electric fields of leaders immediately after charge deposition but before charge motion away from the leader by corona and streamer discharge. This process requires a time $r_0/v_s \simeq 1\text{--}10 \mu\text{s}$.² Limited line charge fields with $E < E_{\text{cr}}^\pm$ are representative of less active stages after charges have begun to move away from the leader channel.

Similar arguments might be made for the electric fields near the leader tip with

²Recall the streamer propagation velocity $v_s \simeq 1 \text{ m}/\mu\text{s}$ from Section 2.3.2

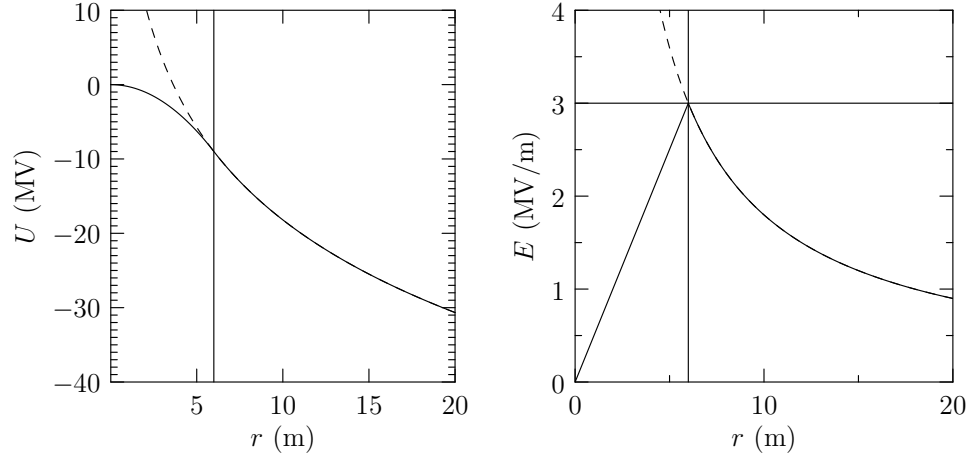


Figure 5.1: **Line charge radius limits.** Electric field and voltage limits for line charges. The effective radius of the line charge is set such that the electric field magnitude never exceeds $E_k \simeq 3 \text{ MV/m}$

assumption of a point charge at the leader tip, but the magnitude of the effective point charge on the leader tip is of order the linear charge density times the effective radius of the wire (*Jackson*, 2000, 2002)³. A typical charge accumulation near the tip is therefore $\Lambda r_0 \simeq 5 \text{ mC}$. This effective point charge contributes less to the electric field in the vicinity of the tip of the leader channel than the linear charge density along the channel near the tip, especially for the regions which contribute most to RREA multiplication.

The RREA multiplication for such electric fields can be easily calculated:

$$\mathcal{M} = \exp \left(\int_{r_a}^{r_b} \frac{dr}{\lambda(E(r))} \right) \quad (5.7)$$

where the integral in effect calculates the total number of avalanche lengths. The resulting avalanche multiplication factor for the limited electric field described above due to various linear charge densities is shown in Figure 5.2.

³The charge density on a charged conducting wire is very close to uniform. Though counterintuitive, only slight non-uniformity is necessary to remove the electric field imbalance.

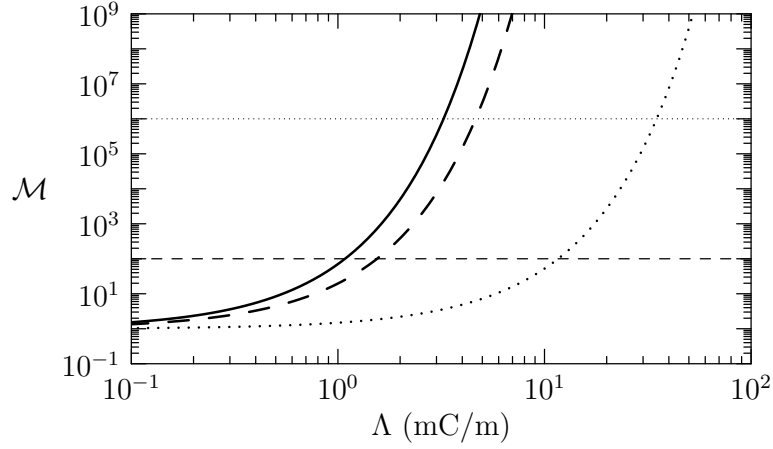


Figure 5.2: **RREA growth factor in a limited line charge field.** The overall avalanche growth factor over the region where the electric field exceeds E_{RREA} , calculated as described in the text. The horizontal dashed line shows $\mathcal{M} = 100$, while the horizontal dotted line shows $\mathcal{M} = 10^6$, the maximum avalanche growth factor allowed by the total thunderstorm potential. The solid, dashed, and dotted curves represent line charges with electric fields limited to $E < E_k$, $E < E_{\text{cr}}^-$, and $E < E_{\text{cr}}^+$, respectively.

Considering a seed source due to leader channels of 10^{15} – 10^{16} as described above, the required multiplication factor is $\mathcal{M} \simeq 10$ – 100 for this population to grow to the 10^{17} energetic electrons required to produce an observable TGF. Figure 5.2 shows this growth factor is attained for charge densities $\Lambda \gtrsim 1$ – 10 mC/m depending on the limiting electric field strength, easily within the range of values inferred from lightning observations (*Rakov and Uman*, 2003, pp. 123–126, 330–331).

5.3 TGF production by lightning current pulses

The above discussion can be put in unified context by consideration of the voltage and electric field. The typical maximum thunderstorm voltage is ~ 100 MV, while any TGF production mechanism must have sufficient voltage to produce 20 MeV

electrons. The large populations produced by RREA require an electric field stronger than E_{RREA} , while the large volumes necessary for RREA cannot support $E > E_k$. The effective voltage available and average electric field available to runaway electrons in the vicinity of limited line charge fields as described above can be estimated from Equation 5.6 simply by calculating the size and potential difference of the region where the electric field exceeds E_{RREA} . Static thunderstorm fields are seldom observed above E_{RREA} but extend up to the maximum potential of the thunderstorm. These voltages and electric fields are shown in a plot of total potential U vs. average electric field E in Figure 5.3. The region that satisfies the constraints in potential and electric field listed above is shaded in grey. Limited line charge electric fields as described above fall nicely in the allowed range, meeting the required electric field strength and producing the required voltage.

This mechanism is significantly different from previously proposed TGF production mechanisms as it occurs very near the leader channel. The nonuniform and local electric field that drives the mechanism also differs from the large-scale relatively-uniform electric fields of the QES and EMP mechanisms discussed in Sections 2.4.1 and 2.4.2. The timescale of the resulting gamma-ray emission is closely tied to the timescale of leader activity.

Lightning timescales vary from microseconds to seconds as listed in Table 5.1. Leader activity takes place on a wide range of timescales from HF pulses from leader stepping (3 mics) to dart leader processes (2 ms). The timescales that best match the TGF timescale are current pulses indicative of leader activity throughout the lightning system (return strokes, M-components, and K-changes), suggesting that large bursts of leader activity are a possible source of TGFs, consistent with the discussion in Section 5.1 where activity over a 1 ms timescale was required to produce a large seed population. This connection between current pulse timescale and TGF timescale is very useful as existing mechanisms do not fully address the TGF timescale. The

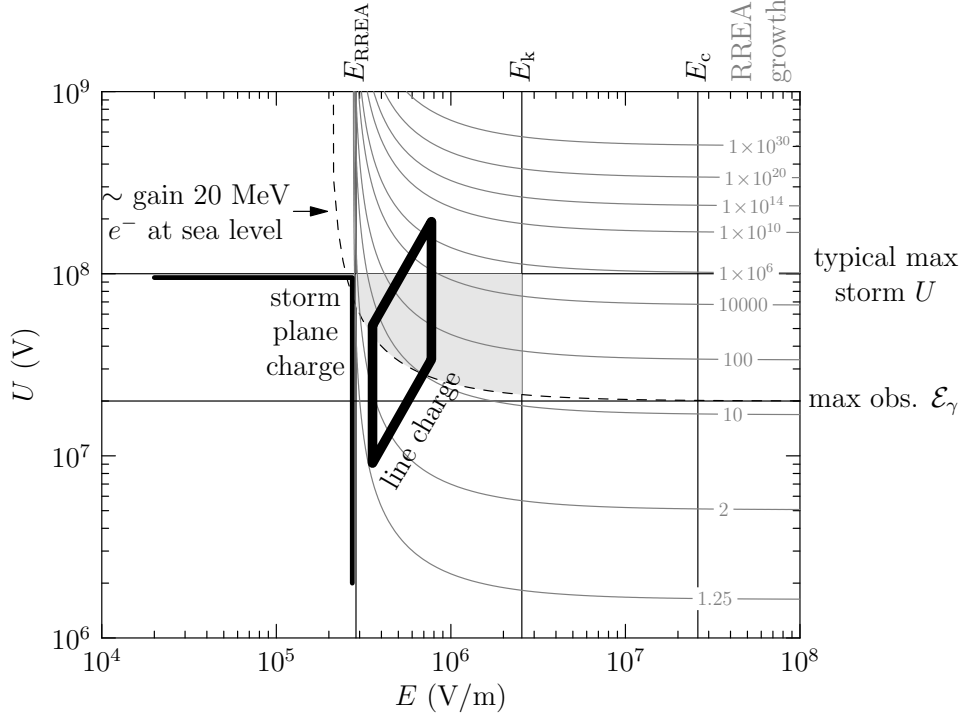


Figure 5.3: **Lightning and TGF electric field and voltage constraints.** Potential (U) vs. electric field (E) with reference voltages labeled at right and reference electric field strengths labeled above. The dashed curve shows the approximate voltage necessary to produce 20 MeV electrons accounting for friction in air at sea level (labeled “gain 20 MeV ...” at left). The region obeying both the constraints for TGF production and lightning is shaded in grey. The maximum RREA avalanche growth factor without relativistic feedback for the given electric field and voltage is shown as the grey contours. The solid line labeled “storm plane charge” represents the highest static voltage and electric fields associated with thunderstorms, while the diamond shape labeled “line charge” represents characteristic electric fields and voltages available to energetic electrons in the vicinity of a typical lightning leader with charge density 0.7–4 C/m.

process	timescale (ms)
streamer	0.001
HF pulses	0.003
leader step	0.003
narrow bipolar pulses	0.01
return stroke	0.1
M-components	1
K-changes	1
dart leader	2
continuing current	5
stepped leader growth	30
return stroke separation	50
lightning overall	100–1000

Table 5.1: **Typical lightning process timescales.** Collected from *Cooray* (2004), *Rakov and Uman* (2003).

QES mechanism provides no realistic emission timescale. The EMP mechanism does provide a timescale, but limits the emissions to the duration of the intense return stroke EMP (tens of microseconds, see *Inan and Lehtinen*, 2005), shorter than typical TGF emissions.

In summary, lightning leader channels driven to widespread activity by current pulses can supply energetic seed electrons for RREA. The electric field of the leader channel itself can drive acceleration and RREA of these seed electrons sufficient to produce observable TGFs. Combining the constraints in Figure 5.3 shows this mechanism obeys all voltage and average electric field constraints. This is the main idea of the lightning current pulse (LCP) mechanism of TGF production.

5.4 Lightning current pulse mechanism predictions

The LCP mechanism outlined above can be used to make predictions about TGF coincidence with lightning, production altitude, and initial photon directional distribution. These predictions are testable with satellite and lightning observation.

As the LCP mechanism produces TGFs with lightning leaders, an almost trivial prediction is that TGFs should never be observed without lightning. It is useful to make this an explicit prediction as it has been suggested that some TGFs can occur without lightning. At the time of this writing, however, there are no clear candidate TGF observations believed to occur without lightning. In particular, though there have been cases suggested where TGFs were observed in locations where lightning could not have occurred (i.e., over the Sahara desert, *Smith et al.*, 2007) or should have been observed had it occurred (*Cohen et al.*, 2007), these cases have since been explained either as indirect observations of electrons trapped on the geomagnetic field produced by distant TGFs (see for example the beautiful modeling results in *Dwyer et al.* (2008a) and other candidate observations in *Carlson et al.* (2009a)) or as experimental anomalies⁴. This prediction can be tested by TGF observations near lightning detector networks sensitive enough to detect even weak intra-cloud lightning activity. If a TGF is observed under circumstances convincingly devoid of lightning, other mechanisms must be considered.

Less trivially, the LCP mechanism requires active lightning leaders in order to ensure RREA seed production. Lightning leader activity is driven by currents flowing on the channel, so direct TGF production by leaders predicts that TGF emission must always be accompanied not only by lightning as a whole but by leader activity as evidenced by current flow in the leader channel network. As such currents emit

⁴Despite appearances, the case mentioned in *Cohen et al.* (2007), though presented as a TGF clearly not associated with lightning, was later retracted as an instrumental effect. The moral: when you have hundreds of events, one-in-a-hundred is actually quite frequent.

electromagnetic waves, the mechanism as described predicts a close time coincidence between TGF emission and radio emission. This is overall consistent with observations, though as mentioned in Section 1.2.4, timing uncertainty limits the accuracy of existing analyses. This prediction may also be tested with accurate timing in the sensitive coincident lightning observations necessary to detect weak intra-cloud lightning activity mentioned above.

The LCP mechanism predicts TGF production very nearby lightning activity. In particular, TGFs should be produced at effectively the same altitude as lightning discharge. Typical lightning spans a range in altitudes, often up to the upper regions of the thunderstorm but does not commonly extend above cloud-tops. The altitude of high-altitude lightning is therefore less than that of the tropopause.⁵ Tropopause height depends on the intensity of solar heating and thus on the latitude and season, but typically varies from 11–18 km over the latitude range covered by RHESSI and BATSE (*Blair and Fite*, 1957, p. 118). The altitude range predicted for TGF production by lightning in the upper regions of a thunderstorm is therefore consistent with the spectral constraints derived in Section 3.2.1 in regions of high tropopause height. High tropopause height is confined to the tropics where both the majority of lightning occurs and the majority of TGFs are observed, a fact suggested to explain the relative lack of TGFs over regions where lightning is otherwise common such as the continental United States and southeastern Australia (*Williams et al.*, 2006). The validity of the LCP mechanism can therefore be tested by searching for TGFs with spectra requiring production significantly above the tropopause, as such TGFs cannot be produced directly by lightning leaders.

As the lightning parameters used in this analysis are not extreme, it is expected

⁵The tropopause marks the boundary between the troposphere and the stratosphere. The troposphere, the “turning” or turbulent and well-mixed portion of the atmosphere is driven primarily by solar heating from below and the instabilities that result. The stratosphere, the “layered” atmosphere, is not as well-mixed and is driven primarily by heating from above due to ozone absorption of ultraviolet light from the sun. What we know as weather occurs entirely in the troposphere.

that gamma-ray emission often accompanies lightning leaders. This is consistent with observations (*Dwyer et al.*, 2003; *Dwyer et al.*, 2004; *Howard et al.*, 2008; *Dwyer et al.*, 2005). However, not all lightning produces TGFs. First note that not all lightning-induced gamma-ray emission is observable by satellites. Low-altitude emissions are heavily attenuated and emissions of relatively few photons are difficult to distinguish from noise. The mechanism we discuss here may require uncommonly large current pulses to drive sufficient activity throughout a high-altitude leader network to produce an observable TGF. Higher altitudes are also favorable due to lower atmospheric density, lower frictional losses, and correspondingly greater RREA growth rates. Also note that as the global frequency of TGFs is not known, a high rate of low-intensity gamma-ray emission events as suggested by the mechanism described above may indeed be present.

The electric fields that drive TGF production in the LCP mechanism are nonuniform and diverge away from the leader channel. The photons produced by energetic electrons driven by such electric fields also diverge away from the leader channel in a very broad beam. This broad beam is nominally consistent with the beaming constraints discussed in Sections 3.2.1 and 3.2.3. Results from *Hazelton et al.* (2009) also indicate TGF data are better fit by beams broader than those due to bremsstrahlung and RREA alone, so the broad beams naturally produced by the LCP mechanism should be considered. More detailed spectral analysis and careful TGF-lightning coincidence studies can be used to test this prediction, as such analyses may indicate narrower beams than can be produced by leader electric fields.

These predictions can all be tested with satellite and radio data. In particular, data from the Fermi Gamma-ray Burst Monitor (GBM), the AGILE satellite,⁶ the

⁶Astro-rivelatore Gamma a Immagini LEggero, an Italian Space Agency satellite.

ASIM experiment,⁷ and the TARANIS satellite⁸ could be used to provide the high precision, high energy-resolution spectra necessary to accurately measure the production altitude to confirm or refute close association with lightning. The ADELE experiment⁹ will provide clear results on the likelihood of frequent low-intensity TGF-like emissions predicted by the relatively common parameters suggested for lightning-driven TGF production. Cameras on ASIM and TARANIS, together with more modern radio data, will help accurately measure the properties of coincident lightning and the nature of the temporal and spatial association between lightning and TGF production. This knowledge will help determine the validity of the LCP mechanism of TGF production mechanism described above.

⁷The Atmosphere-Space Interactions Monitor, a European Space Agency experiment for the international space station.

⁸Named for the Celtic god of thunder and as the Tool for the Analysis of RAdiation from lightNING and Sprites, a French (CNES) satellite.

⁹The Airborne Detector for Energetic Lightning Emissions, an aircraft-borne gamma-ray detector experiment funded by the NSF.

5.5 Comparison to relativistic feedback TGF production

An alternative mechanism to LCP TGF production is the relativistic feedback mechanism in static thunderstorm electric fields as suggested by *Dwyer* (2009). Relativistic feedback as described in Section 2.2.1 also removes the restriction on the seed population by effectively allowing an initial avalanche to seed a second generation of avalanches. This requires the production of new effective seed particles by photon and positron propagation back to near the starting point of the original avalanche. As such, relativistic feedback depends on the size and shape of the electric field region. *Dwyer* (2003) gives constraints on the size and shape for uniform electric fields. For instance, a 1 MV/m electric field requires a size of at least 100 m (available potential $U \geq 100$ MV) for relativistic feedback to occur. These are shown in Figure 5.4 superimposed on the central region of Figure 5.3.

Relativistic feedback in thunderstorm conditions therefore requires relatively high electric field over a relatively long length-scale. *Dwyer* (2009) suggests these conditions may be met in a thunderstorm and that TGFs may result.

Relativistic feedback in thunderstorm electric fields as a TGF source has several key characteristics that distinguish it from LCP TGF production. Relativistic feedback does not require a lightning discharge, and therefore is a possible explanation if TGFs are produced without lightning. Thunderstorm static electric fields are typically quite uniform, so relativistic feedback predicts photon emissions with relatively narrow directional distribution. Finally, once initiated, relativistic feedback continues to grow until the electric field either naturally decays or is forced to decay by the currents produced in RREA. The characteristic timescale of the decay of the electric field under relativistic feedback process is 20 μ s, shorter than the typical TGF timescale, but is very strongly dependent on the electric field for E near E_{RREA} and can be

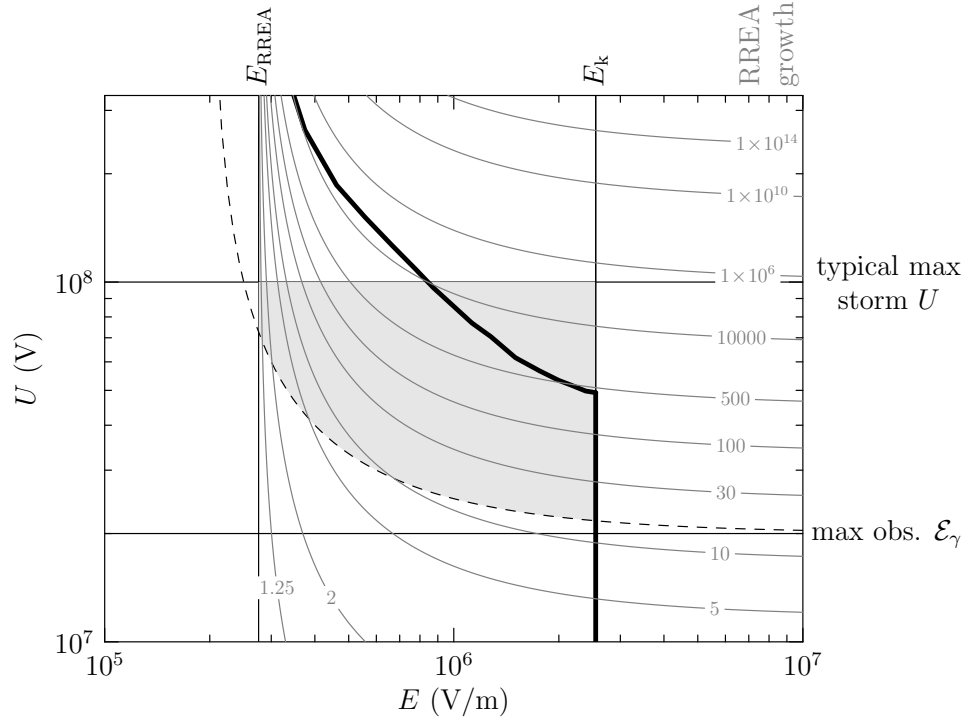


Figure 5.4: **Relativistic feedback constraints.** Central region of Figure 5.3 as before but without thunderstorm charge structures. The thick black curve is the minimum voltage and electric field required for relativistic feedback derived for uniform fields in *Dwyer* (2003). Above and to the right of this curve, the electric field is extremely unstable. Different results are found for nonuniform fields.

as high as $100\ \mu\text{s}$ (*Dwyer*, 2007). This is still slightly lower than the typical TGF timescale, but is within the realm of possibility. Note, however, that Figure 5.4 shows that relativistic feedback at fields near E_{RREA} as necessary for longer timescales also requires very high voltages.

Though the timescale is nominally too short and very high voltages and electric fields are required, relativistic feedback does cover some of the allowed region in Figure 5.4. Further studies are required to assess relativistic feedback in the uniform fields considered in *Dwyer* (2003) and *Dwyer* (2007) as a TGF production mechanism.

5.5.1 Relativistic feedback in nonuniform fields

As relativistic feedback may be relevant to thunderstorm electric fields, it may also be relevant to the nonuniform electric fields surrounding lightning leader channels. In such conditions the confinement of the electric field renders it much less likely that a photon or positron will make its way to regions favorable to the production of a second generation of avalanches. This depends on the geometry and polarity of the electric field, however, so it is useful to measure the feedback behavior of such fields.

Here GEANT4 simulations of RREA are used as the basis for a feedback measurement scheme. The limited electric field described above is used to drive RREA of a population of seed 1 MeV electrons placed in the high potential energy region of the field with their velocities pointing in the direction of avalanche growth. As RREA of this population proceeds, the total number of electrons produced is recorded. Secondary particles produced by electrons are tracked without limitation, including bremsstrahlung photons and positrons resulting from pair production. However, electrons produced by photons or positrons are classified as second-generation seed particles and are recorded and removed from the simulation. The result of such simulations is the number of electrons produced in the first generation avalanche and the positions and momenta of seed particles for the next generation. The potential avalanche growth of these possible second-generation seed particles is then calculated with Equation 5.7 integrated along the path of the avalanche that would result. The sum of these avalanche multiplication factors for all of the possible second-generation seed electrons is an estimate of the possible size of the second generation. The quotient of this estimate of the second generation population with the measured first generation population size is a measure of the feedback factor Γ . If $\Gamma < 1$, the second generation is smaller than the first and the overall activity of the system should decay away with time, while if $\Gamma > 1$ the second generation is bigger than the first generation, and relativistic feedback effects must be considered.

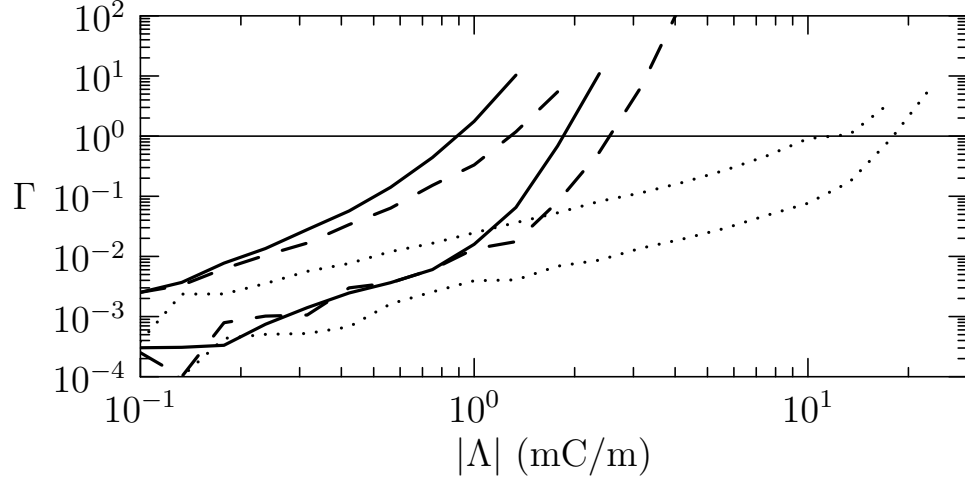


Figure 5.5: **Relativistic feedback in limited line-charge fields.** Relativistic feedback factor vs. line charge density for a limited line charge electric field. Solid curves represent limited line charge fields with $E < E_k$, dashed lines represents $E < E_{cr}^-$, and dotted lines represent $E < E_{cr}^+$. The upper of each pair of curves is associated with positive charge densities.

Feedback factor simulations for electric fields due to limited line charges are shown in Figure 5.5. For small charges and confined fields, the feedback factor is much less than unity, and feedback can be neglected. For line charges with radius set by $E < E_k$, negative line charge densities $|\Lambda| \gtrsim 2 \text{ mC/m}$ and positive line charge densities $\Lambda \gtrsim 1 \text{ mC/m}$ give $\Gamma > 1$ and feedback is expected to develop. For line charges with radius set by $E < E_{cr}^-$, feedback does not develop as readily and requires a negative density $|\Lambda| \gtrsim 3 \text{ mC/m}$ or a positive density $\Lambda \gtrsim 1.5 \text{ mC/m}$, while line charges limited by $E < E_{cr}^+$ require charge densities $\Lambda \gtrsim 10 \text{ mC/m}$ for positive line charges and $|\Lambda| \gtrsim 20 \text{ mC/m}$ for negative line charges.

The greater relevance of relativistic feedback for positive leaders is a result of the position of the high-potential-energy region for seed electrons as shown in Figure 5.6. For negative leaders, relativistic electron avalanches must start near the leader channel and travel away. Any photons produced by the energetic electrons will also be beamed

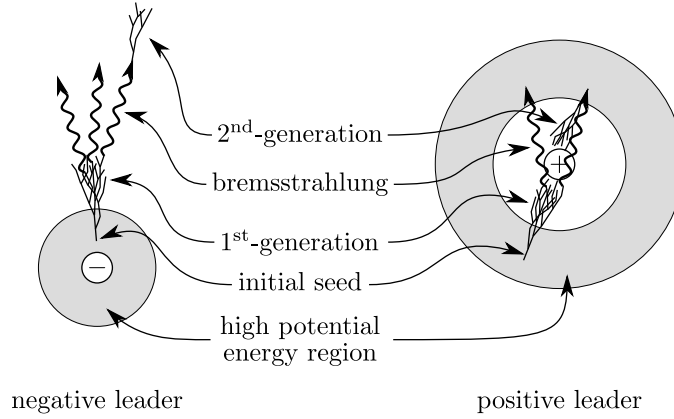


Figure 5.6: **Photon feedback and charge polarity.** Cross sectional diagram of relativistic feedback mediated by energetic photons near positive and negative leaders. Photon feedback in electric fields of negative line charges typically produce second generations away from the high-potential-energy region, while positive line charge electric fields allow for such photons to reenter the high-potential-energy region more easily.

away from the leader and thus into low potential energy regions where they are unlikely to seed significant second generation avalanches. Avalanches in the electric field of positive leaders must start away from the leader and grow toward the leader channel. Photons produced by such avalanches will be emitted toward the leader channel and after passing the leader channel itself may travel back into the high potential energy region.

This result shows that the negative leaders required by the LCP mechanism are less likely to show relativistic feedback. Positive leaders, by contrast, cannot directly produce seed electrons in the high potential energy region and thus are not candidates for LCP TGF production, but may be more likely to show relativistic feedback.

Thus, if the linear charge densities are sufficiently high and concentrated sufficiently close to the leader channel, relativistic feedback will develop and its effects must be considered. If such high charge densities occur, relativistic feedback will act to decrease the field below E_{RREA} on a timescale of 10–100 μs . The amount of

energy released as energetic bremsstrahlung in this process is unknown and requires detailed study with a full self-consistent mechanism of RREA, relativistic feedback, the relativistic currents, and conductivity enhancements that result.

5.6 Summary

The maximum RREA growth factor together with the maximum allowed energetic seed particle population are not sufficient to account for observable TGFs. This realization leads to the suggestion of negative lightning leader channels as the key driving force behind TGF production, providing both RREA seed source and driving electric field. Evidence for the seed source is seen in experiments and total seed flux derived in the literature for active leader channels is consistent with TGF production if the leaders are driven to activity by current pulses for the ~ 1 ms TGF timescale. Estimates of the electric field near negative leader channels give sufficient avalanche multiplication of the seed flux if the linear charge density $|\Lambda| > 1\text{--}10$ mC/m (depending on the effective radius of the line charge), within range of values observed in experiments. The total voltage and electric field constraints shown in Figure 5.3 are satisfied by this mechanism, leading to the suggestion of lightning current pulse (LCP) TGF production. Relativistic feedback may also be relevant, especially for positive leader channels, though further analysis is required. TGFs may therefore be produced by active leader channels driven by current pulses. The core idea of LCP TGF production is available in the literature in *Carlson et al.* (2009b).

Chapter 6

Lightning TGF production model

The analyses in Chapter 5 suggest that the electric fields of negative lightning leaders, together with RREA seed production by active leaders driven by lightning current pulses can drive TGF production, dubbed the lightning current pulse (LCP) TGF production mechanism. The results of Chapter 5 indicate that the LCP TGF production mechanism satisfies the electric field and voltage constraints. The LCP mechanism may produce the overall energy required if sufficient leader activity occurs in the timescale of TGF emission as suggested by the timescale of large current pulses in leader channels.

The key question is whether or not the current pulses in leader systems actually are capable of driving TGF production, and if so what currents are required. This chapter describes a model of the LCP TGF production mechanism. Lightning current pulse propagation is modeled by the method of moments. This model is used to determine temporal and spatial dependence of the electric field over volumes near the leader. This electric field is then used to drive GEANT4 simulations of RREA. The properties of the resulting RREA including the energy spectra and photon directional distributions are derived and compared to the constraints on TGF production discussed in Chapters 3 and 5.

6.1 Lightning electric field model

The electric field surrounding a lightning leader is a combination of the ambient thunderstorm electric field (\mathbf{E}_s) and the electric field due to charges on and currents flowing along the leader channel (\mathbf{E}_l). The total electric field $\mathbf{E}_t = \mathbf{E}_s + \mathbf{E}_l$ determines the flow of charges on the resistive leader channel. The time evolution of the system of charges and currents is also affected by the development of the channel. Sudden extensions and connections of the channel with regions of positive or negative charge lead to current pulses. Such pulses are proposed as associated with the leader activity driving RREA seed production and TGF emission in the LCP mechanism discussed in Chapter 5. A full model of the behavior of the currents and charges on the lightning channel is therefore useful for consideration of TGF production by such currents.

Such models can be constructed in several ways, depending on the phenomenon of interest. Complete reviews can be found in *Rakov and Uman* (1998) and *Baba and Rakov* (2007). Existing modeling efforts treat a range of processes, from the plasma physics of the leader channel to electromagnetic processes involved in current flow. Plasma physics models strive to treat the leader by solving the gas dynamics equations involving conservation of energy, momentum, and mass, together with the equation of state of the plasma and energy input from applied currents. Electromagnetic models treat the leader as an abstract resistive or conducting channel and solve Maxwell’s equations together with Ohm’s law, allowing determination of the currents and electromagnetic fields. Higher level models are also possible, involving further approximations such as treatment of the channel as a transmission line (solving the telegrapher’s equations) and “engineering models” that merely assume properties grossly consistent with observed lightning discharges.

Here, the electric field produced by the lightning channel as a driver of energetic

electron physics requires an electromagnetic model of the lightning channel. Electromagnetic models solve Maxwell's equations by a variety of techniques. One approach is by finite-difference methods (for instance, *Noda and Yokoyama, 2002*), which convert Maxwell's equations to a set of matrix equations describing the evolution of the charges, currents, and electromagnetic fields on a grid spanning the volume of interest. As lightning leaders have very tortuous structure, accurate representation of the fields near the channel requires a very fine grid with correspondingly large memory requirements for full 3-dimensional simulation domains. The approach used here instead uses the method of moments, which converts Maxwell's equations in retarded-time integral form into a system of matrix equations involving segments of the channel (*Rao, 1999, Chapter 2*). This conversion reduces the memory requirements and allows for treatment of detailed 3-dimensional channel structures.

The starting point for the electromagnetic model constructed herein is the electric field integral equation which gives the electric field at any point in terms of the charges and currents present in the system (EFIE, eq. 6.55 *Jackson, 1999, pp. 247*):

$$\mathbf{E}_t(\mathbf{x}, t) = \frac{1}{4\pi\epsilon_0} \int d^3x' \left\{ \frac{\hat{\mathbf{R}}}{R^2} [\rho(\mathbf{x}', t')]_{\text{ret}} + \frac{\hat{\mathbf{R}}}{cR} \left[\frac{\partial \rho(\mathbf{x}', t')}{\partial t'} \right]_{\text{ret}} - \frac{1}{c^2 R} \left[\frac{\partial \mathbf{J}(\mathbf{x}', t')}{\partial t'} \right]_{\text{ret}} \right\} \quad (6.1)$$

Where ρ is the volume charge density, \mathbf{J} is the current density, $\mathbf{R} = \mathbf{x} - \mathbf{x}'$, $R = |\mathbf{R}|$, $\hat{\mathbf{R}} = \mathbf{R}/R$, and the subscript “ret” indicates that the term in brackets is to be evaluated at the retarded time $t' = t - R/c$. The EFIE can be most readily derived from the retarded-time integral solutions for the electric scalar potentials Φ and the magnetic vector potential \mathbf{A} , but the details are not illustrative (see *Jackson, 1999, pp. 246–7*).

The electric field and the current are related by Ohm's law:

$$\mathbf{J} = \sigma \mathbf{E}_t \quad (6.2)$$

Note that this simple form of Ohm's law ignores the effects of magnetic fields. This assumption is justified by the relatively low velocity of the electrons that carry the bulk of the charge in a lightning stroke together with the high collision frequency for such electrons at altitudes characteristic of lightning.

Together with the equation of charge conservation,

$$\frac{\partial \rho}{\partial t} + \nabla \cdot \mathbf{J} = 0 \quad (6.3)$$

Equations 6.1 and 6.2 provide a full system of integro-differential and partial differential equations describing the time evolution of charges and currents in a resistive or conducting system.

6.1.1 Method of moments simulation

It remains to solve the system of Equations 6.1, 6.2 and 6.3 in the context of lightning. Due to the difficulty of solving integral equations, let alone integro-partial-differential equations, approximations and simplifications must be made. Here the thin wire approximation and the method of moments are used. The approach used here is similar to and motivated by the approach in *Miller et al.* (1973).

The thin wire approximation treats Equation 6.1 as a line integral over the leader channel instead of a volume integral. This simplification is accomplished by assuming that the currents flow purely in the direction of the leader and that the charges and currents reside at the center of the leader while the electric field is evaluated at the surface of the channel. This assumption allows the replacement of R with $L = \sqrt{R^2 + a^2}$, effectively preventing any quantity from being evaluated at points closer than a distance a away from the center of the channel. This approximation is justified if the channel is sufficiently longer than its radius, typically by at least a factor of 4. This condition is clearly applicable to lightning channels linear on a scale

of 100 m with radius $a \simeq 1\text{--}10$ m.

Application of the thin wire approximation allows integration over the transverse dimensions of the wire, giving:

$$\mathbf{E}_l(\mathbf{x}, t) = \frac{1}{4\pi\epsilon_0} \int ds' \left\{ \frac{\hat{\mathbf{R}}}{L^2} [\Lambda(s', t')]_{\text{ret}} + \frac{\hat{\mathbf{R}}}{cL} \left[\frac{\partial \Lambda(s', t')}{\partial t'} \right]_{\text{ret}} - \frac{\hat{\mathbf{s}}}{c^2 L} \left[\frac{\partial I(s', t')}{\partial t'} \right]_{\text{ret}} \right\} \quad (6.4)$$

where s' is a linear position coordinate along the leader, $\hat{\mathbf{s}}$ is a unit vector in the direction parallel to the channel, Λ is the linear charge density, and I is the current in the channel. Charge conservation and Ohm's law similarly become

$$\frac{\partial \Lambda}{\partial t} + \frac{\partial I}{\partial s} = 0 \quad (6.5)$$

$$IR_l = \mathbf{E}_t \cdot \hat{\mathbf{s}} \quad (6.6)$$

where R_l is the resistance per unit length of the channel, $\mathbf{E}_t = \mathbf{E}_s + \mathbf{E}_l$, \mathbf{E}_l is evaluated as in Equation 6.4 and \mathbf{E}_s is the applied electric field due to thunderstorm charges not on the leader channel. Ohm's law (Equation 6.6) can then be applied to the electric field integral equation to close the system and give an equation for $I(s, t)$ in terms of an integral of Λ and I . The quantity Λ can in turn be calculated as an integral of I ,

$$\Lambda(s, t) = - \int_{-\infty}^t \frac{\partial}{\partial s} I(s, \xi) d\xi \quad (6.7)$$

leaving an equation for I in terms of past and present values of I , integrals of I , and derivatives of I .

The method of moments then exploits the linearity of the integro-differential operator in Equation 6.4 to convert it into an algebraic equation. The method of moments proceeds by breaking the charges and currents into segments. The discretization scheme used here is shown schematically in Figure 6.1. The charge distribution is

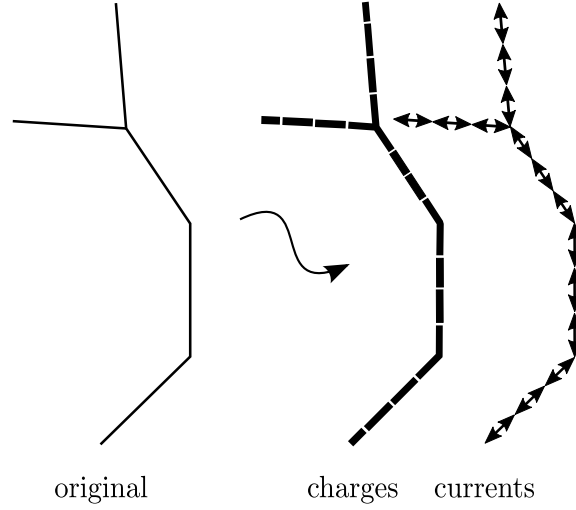


Figure 6.1: **Method of moments discretization scheme.** Current and charge distributions on the original channel are divided into segments as shown.

broken up into groups of short linear segments, while the current distribution is broken up into simple linear segments. The segment length must be $l \gtrsim 4a$ as required by the thin wire approximation applied over each segment, with segment lengths near this lower limit generally desirable to allow high spatial and temporal resolution.

The linear charge densities and currents are assumed to be constant over each charge segment, allowing the integral in Equation 6.4 to be evaluated in terms of the unknown charge and current values on the segments. The EFIE is thereby converted into a purely algebraic equation. Note also that the geometric portions of the integral are thus independent of the state of the system and therefore need only be calculated once. This evaluation is carried out at the center of one of the current segments, thereby giving the current on that segment in terms of past values of the currents on other segments in one large linear equation.

Repetition of this procedure on the other current segments produces a system of linear equations. This system of equations can be solved to find the values of the currents at the next time-step dt later. In practice the system of equations is

nearly diagonal as most of the contributions to the electric field are due to the known past history of the system. Linear interpolation in time is used to evaluate these past charge and current values. However, if the geometry of the system is such that certain charges and currents fall less than a distance of $c dt$ apart, the value of one current at the next time-step depends on the unknown value of another current at the same time-step. The evaluation of the contribution of one current to the other therefore requires interpolation involving unknown values and produces off-diagonal components in the system of equations. In particular, as the current and charge segments are offset, the adjacent charge values are often separated from the currents that feed them by less than $c dt$. The necessary interpolation improves the stability of the system effectively by providing immediate feedback about the effect of the current in question on the charges it connects, but requires solution of an approximately tridiagonal system of linear equations.

The solution of the system of equations gives the next set of currents in the system. Note that the matrix that describes the equations of this scheme depends only on the geometry of the system and thus is not time dependent. Any matrix inversions involved in the solution to the system necessary at each time-step can thus be calculated only once at the start of the simulation and reused thereafter, though in practice it can be faster to repeatedly invert the sparse matrices involved than to repeatedly multiply dense matrices. Simple integration of currents in and out of the charge segments then gives the corresponding set of charge values. Repeating the process gives the time evolution of the current and charge values in the system. Each step in the simulation therefore involves an integral over past values of the charges and currents to calculate the electric field, construction of a matrix equation incorporating the channel resistance and any dependence of the electric field on the unknown currents, solution of the resulting linear system to determine the unknown currents, and integration of the currents to determine the unknown charges.

The system is implemented computationally as approximately 700 lines of Haskell, a purely functional programming language featuring garbage collection and an optimizing native-code compiler. The Haskell functions make use of the HMatrix¹ bindings to the GNU Scientific Library,² BLAS,³ LAPACK⁴, and custom bindings to CXSparse for sparse matrix operations.⁵ Geometric and interpolation factors are pre-calculated and used repeatedly.

Though written in a high-level language, the results are sufficiently fast that further optimization has not been necessary for systems with fewer than a few thousand current segments. As the bulk of the computation time is spent calculating sums over past current and charge states in the electric field integral, large performance gains could be obtained by splitting the workload among many processors on a multi-processor machine. Further performance gains could be obtained by vectorizing the code for execution on a graphics processor. Graphical output is provided by simple OpenGL code. Electric field output is supported on Cartesian grids covering regions of interest. The scheme described is stable if the conditions of the thin wire approximation are met. High frequency noise sometimes appears but can be removed with a simple averaging procedure as discussed in *Smith* (1990).

The code has been validated by comparison to results given in *Poggio et al.* (1973) for a thin wire antenna excited by an electric field pulse at its center. The current induced at the center of the antenna is shown in Figure 6.2. The results are in good agreement with the possible exception of the high-frequency components which dissipate slightly more quickly in the current pulse simulation than in the results from *Poggio et al.* (1973).

The simulation has also been validated in the context of lightning return strokes

¹<http://hackage.haskell.org/package/hmatrix>

²<http://www.gnu.org/software/gsl/>

³<http://www.netlib.org/blas/>

⁴<http://www.netlib.org/lapack/>

⁵<http://www.cise.ufl.edu/research/sparse/CXSparse/>

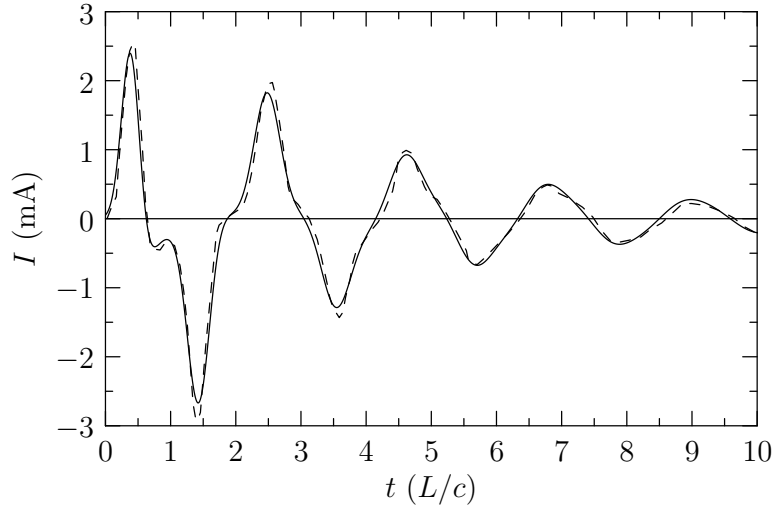


Figure 6.2: **Current pulse simulation for straight antenna.** Simulation of current at the center of a thin straight wire of radius 1 m as excited by a localized Gaussian electric field pulse at the center ($E = 11 \text{ V/m} \exp(-a^2 t^2)$ where $a = 1.5 \times 10^9 \text{ s}^{-1}$). The current pulse simulation results (solid) are compared to results for the identical situation described in *Poggio et al. (1973)* (dashed).

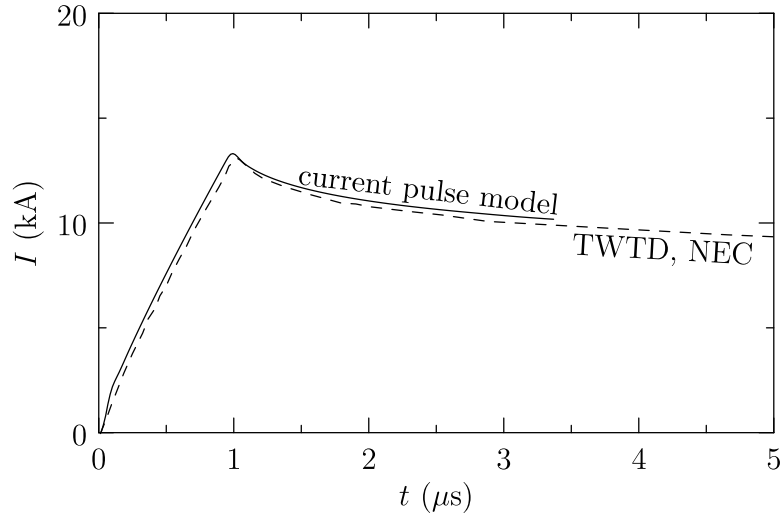


Figure 6.3: **Current pulse simulation comparison to NEC2, TWTD.** Simulation of current at ground level on a perfectly conducting vertical channel over a perfectly conducting ground driven by a δ -gap electric field source with a $1 \mu\text{s}$ rise-time as described in *Baba and Rakov (2007)*.

against results from the Numerical Electromagnetics Code (NEC2) and the Thin Wire Time Domain (TWTD) code shown in *Baba and Rakov* (2007). These results are shown in Figure 6.3. Some rescaling of the results is required due to the use of a larger radius wire in the current pulse simulation than that used in the NEC2 and TWTD simulations, but overall agreement is very good.

Figure 6.4 shows a sample of the output of the model for a simulated lightning return stroke. The channel shown and its image are allowed to relax in a vertical ambient electric field to approximate a lightning channel over conducting ground. The channel and its image are then connected to represent the connection of the leader with ground and allow simulation of the subsequent return stroke. The electric field evaluated over a plane that intersects the channel extending out toward the viewer is represented in Figure 6.4 by arrows. The simulated return stroke intensifies the electric field near the tip of the channel as shown in Figure 6.5. This intensification drives leader activity, seed runaway electron production, and RREA growth.

Overall the results of the current pulse model described herein agree well with those of existing models of current pulse behavior and provides a good platform from which to calculate the electric fields near leader channels and thus the dynamic effects of current and charge rearrangements.

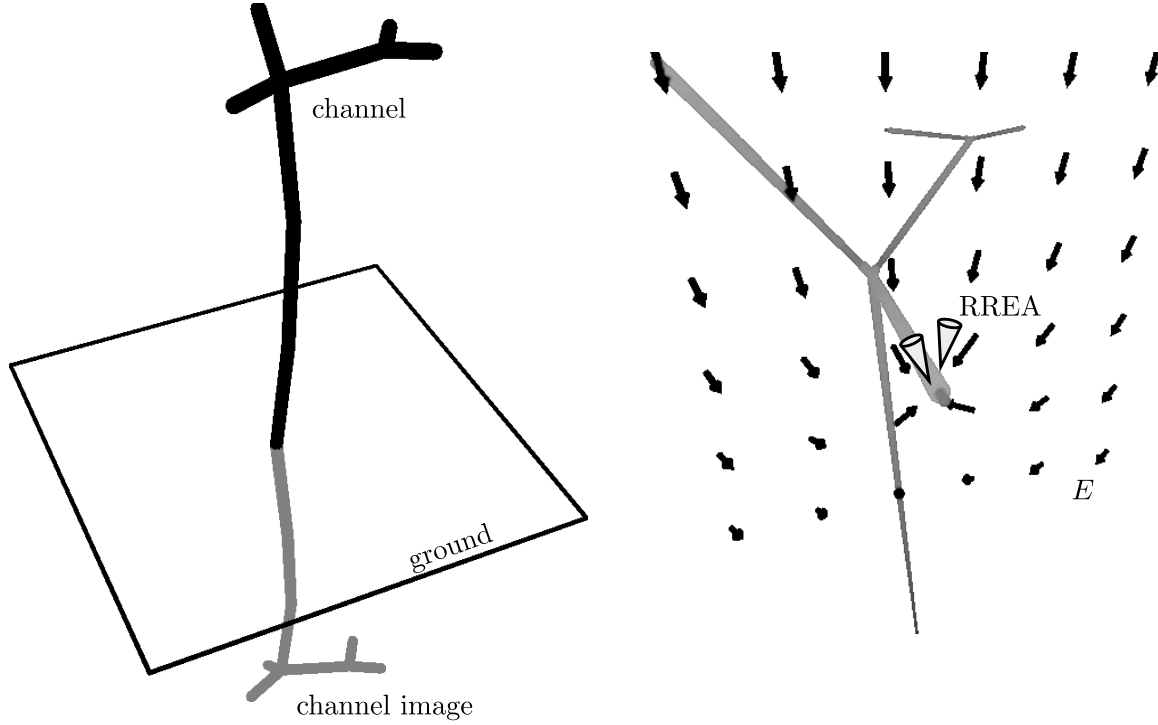


Figure 6.4: **Realistic lightning channel simulation.** Left: a possible lightning channel. From ground to top the channel is ~ 1 km tall. Right: the upper portions of the channel. The segment that extends toward the viewer is cut by a plane where the electric field \mathbf{E}_t is represented by the arrows. In the simulations, the current pulse due to connection of the channel with its image drives RREA near the tip of the channel as indicated. Graphics generated by OpenGL.

6.2 RREA in realistic lightning electric fields

The electric fields calculated in the results of the current pulse model described above can drive RREA. If the current pulse is sufficiently intense as is the case in Figure 6.5, the electric field increases far above the threshold for runaway relativistic electron avalanche (E_{RREA}) and can accelerate runaway electrons to high energies and drive RREA growth. In this section, the fields thus calculated are used to drive GEANT4 simulations of RREA such that the properties of the resulting energetic particles can be simulated.

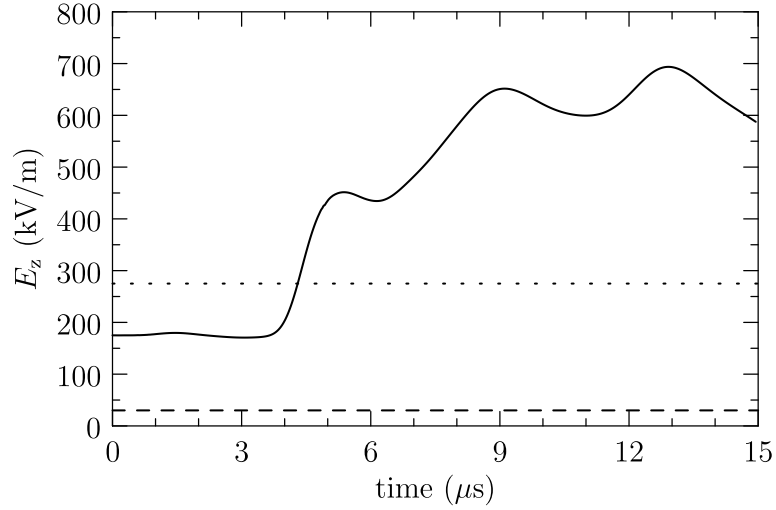


Figure 6.5: **Electric field intensification.** The electric field magnitude near the tip of the leader channel as a function of time as a return stroke current pulse arrives. The geometry for the lightning channel is the same as that shown in Figure 6.4. The dashed line shows the ambient thunderstorm field strength, while the dotted line shows E_{RREA} . In this case, the current pulse that arrives drastically increases the electric field, pushing it above E_{RREA} .

The electric field from the current pulse model is provided over a Cartesian grid covering a region of interest at successive time-steps. This output is then used in a linear interpolation scheme to give the electric field at arbitrary points and times inside the region of interest. This space- and time-dependent electric field is used by GEANT4 to determine particle trajectories and energy changes. The properties of the RREA that results are recorded by a system similar to that described in Section 5.5.

Sample results for the system shown in Figures 6.4 and 6.5 when seeded with 10^4 1-MeV electrons near the tip of the channel as shown in Figure 6.4 are given in Figures 6.6 and 6.7. Relativistic feedback is suppressed as in Section 5.5 but was determined to be insignificant for this case and therefore does not significantly affect the results displayed in Figures 6.6 and 6.7.

Figure 6.6 shows the directional distribution of bremsstrahlung photons emitted

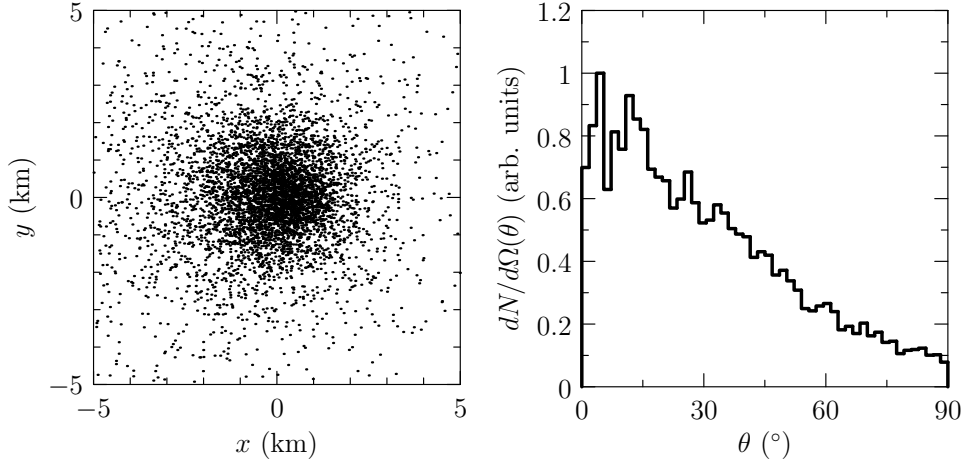


Figure 6.6: **Directional distribution of emissions from current pulse model.** Left: position of photons emitted as they cross a plane 2 km above electron injection in the electric field near a leader channel. The dispersion is almost entirely due to photon directional dispersion. The offset and asymmetry is due to the electric field used. Right: zenith angle distribution in solid angle.

from RREA driven by the current pulse model. The photons produced are emitted in a broad beam from a relatively confined source, consistent with the requirement of relatively broad initial directional distributions derived in Chapter 3.

The energy distribution of photons emitted is shown in Figure 6.7. The spectrum changes drastically upon arrival of the current pulse and intensification of the electric field. The energy spectrum is time-dependent, so comparisons to the constraints derived in Chapter 3 are also time-dependent, but the spectra that result are typical of the spectra that result from energetic electron populations produced by RREA (as found in *Lehtinen et al.*, 1999). The maximum total voltage available in the electric field determines the maximum electron and photon energies attained, so the photon spectrum produced by the current pulse model is dependent on the magnitude and duration of the current. The requirement to produce sufficiently energetic electrons suggests a constraint on the current pulse behavior necessary to produce TGFs.

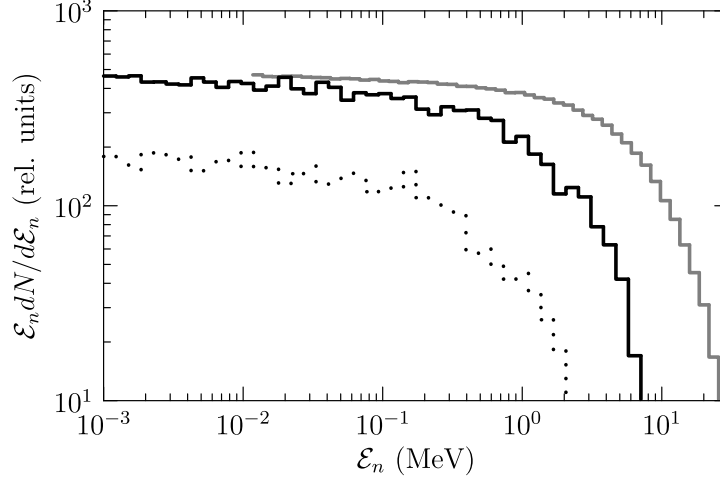


Figure 6.7: **Photon energy spectra intensification from current pulse model.** Dotted curve: before current pulse. Solid black curve: after current pulse. Overall flux and maximum energy increase dramatically. Solid grey curve: shape of bremsstrahlung initial photon spectrum used in Chapter 3. The sample current pulse in question does not produce sufficiently energetic electrons to produce the highest-energy photons observed in a TGF.

6.3 TGF production requirements

The model described above gives the electric field near a leader channel and its time evolution. The GEANT4 simulations of RREA produced by this electric field suggest that photon emissions require intense current pulses in order to generate appreciable emissions. This requirement is in agreement with the results of Section 5.2 and Figure 5.3 where only sufficiently large charge densities are found to have enough available voltage to produce 20 MeV electrons and photons.

The requirements on the current pulse amplitude can be derived semi-analytically from consideration of the charge densities resulting from current pulse propagation together with simulations of such current pulses on leader channels.

The overall behavior can be derived from conservation of charge along a wire:

$$\frac{\partial \Lambda}{\partial t} + \frac{\partial I}{\partial s} = 0 \quad (6.8)$$

With $\partial \Lambda \rightarrow \Lambda_0$, $\partial t \rightarrow dt$, $\partial I \rightarrow I_0$, and $\partial s \rightarrow c dt$, the typical charge density associated with a current pulse of magnitude I_0 is $\Lambda_0 = I_0/c$. The characteristic charge magnitudes obtained from Figure 5.3 are of order $\Lambda_0 \simeq 1 \text{ mC/m}$, giving $I_0 \simeq \Lambda_0 c = 300 \text{ kA}$. This result suggests we can expect large currents, but this crude analysis does not include existing charge or the influence of the thunderstorm electric field.

More rigorous results can be obtained by use of the current pulse model. First, consider the static situation where charges have been allowed to relax in an applied electric field. A conducting channel under these circumstances accumulates a positive charges on one side and negative charges on the other as shown in Figure 6.8. The charge density attained near the ends of the wire is approximately 0.5 mC/m for a 1 km wire in a 50 kV/m electric field. The scale of the simulation shown in Figure 6.8 is comparable to that present in segments of leader channels. As such, higher electric fields are required to boost the equilibrium charge density further into the allowed region of Figure 5.3, so 50 kV/m can be taken as a lower limit on the electric field strength.

The current pulse magnitude necessary to boost the charge density near the end of such a conducting channel can also be assessed with the current pulse model. Simulations of the time evolution of the charge density on an initially-uncharged straight wire embedded in an electric field show that the actual current magnitude necessary to boost the charge density near the tip of a leader channel into the allowed region in Figure 5.3 is nearly always $I_0 \gtrsim 40 \text{ kA}$. A representative simulation is shown in Figure 6.9. Current pulse magnitudes $I_0 \simeq 40 \text{ kA}$ produce a charge density

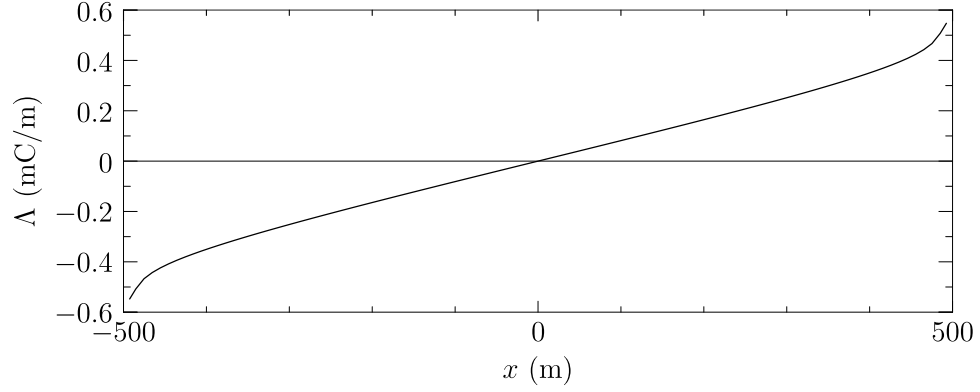


Figure 6.8: **Charge density on a conducting wire in an electric field.** Shown for a 1 km long wire 1 m in radius embedded in a 50 kV/m electric field along the direction of the wire.

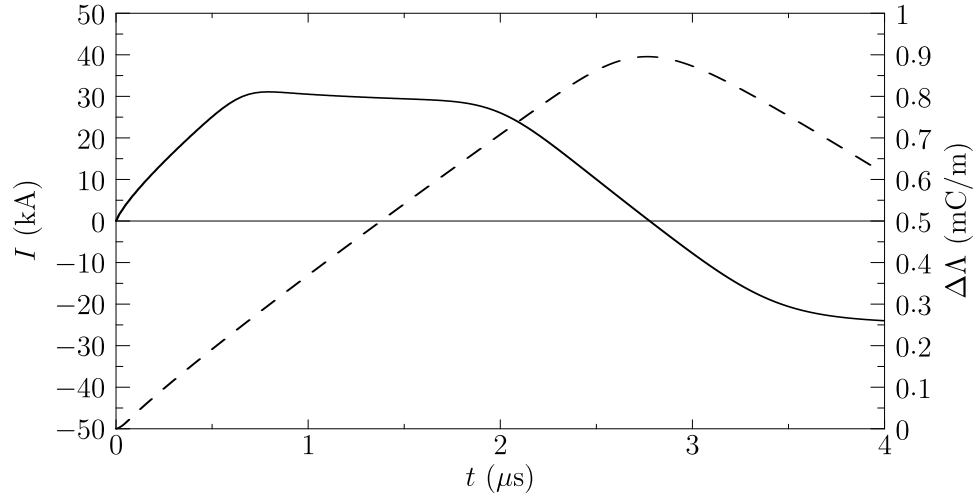


Figure 6.9: **Channel current and resulting charge enhancement.** The current flowing in a channel (solid line, left y -axis) is shown together with the resulting charge density enhancement (dashed line, right y -axis) near the end of the channel as a function of time. Here, $I_0 \simeq 30$ kA gives $\Delta\Lambda \simeq 0.9$ mC/m.

enhancement near the end of the wire $\Delta\Lambda \simeq 1$ mC/m.

Together with an ambient electric field $E_s \gtrsim 50$ kV/m, a current pulse of $I_0 \gtrsim 40$ kA will push the region near the tip of the leader channel into the grey region of

Figure 5.3 allowed for TGF production. Such current pulses also drive activity at the leader tip due to the intensified electric field, setting the stage for RREA growth as described in Chapter 5.

Though $E_s \gtrsim 50 \text{ kV/m}$ is common in thunderstorms, the frequency of appropriate current pulses with $I_0 \gtrsim 40 \text{ kA}$ is unknown. Return stroke current magnitudes are often greater than 40 kA , and such current pulses may drive TGF-like gamma-ray emissions. However, true TGF emission observable by satellite can only result from such current pulses along leader channels at 15–20 km altitudes. At such altitudes, the reduced atmospheric density reduces the electric field requirements for RREA, resulting in more efficient avalanche growth at a given electric field. However, current pulses at such altitudes are likely produced by intra-cloud (IC) lightning. As IC lightning does not connect with ground, there are fewer sudden voltage changes of the type shown in Figure 2.8 and IC lightning current pulses are typically less than 10 kA (Figure 5.14 *Betz et al.*, 2009, p. 131). However, the peak currents of narrow bipolar pulses, a class of impulsive IC discharge, are occasionally above 30 kA (*Eack*, 2004), suggesting such high-current events may occur. The durations of narrow bipolar events are much shorter than the TGF timescale, however. These considerations suggest that the relative rarity of TGFs (1 in 10^4 lightning discharges as discussed in Section 1.2.3) may result from the rarity of high-amplitude 1-ms current pulses at 15–20 km altitudes. Better estimates of the distribution of current pulse amplitudes and durations at 15–20 km altitudes can directly address this question.

6.3.1 Discussion

The current pulse mechanism as described in Chapter 5, translated into a method of moments simulation of lightning electric fields together with GEANT4 simulations of the resulting RREA, thus provides a reasonable model for TGF production. The source lightning is required to occur in an electric field $E_s \gtrsim 50 \text{ kV/m}$, and while

there is no requirement on the quantity of charge moved in the discharge, the current pulses that stimulate leader activity, RREA seed production, and RREA must have a magnitude of $I_0 \gtrsim 40 \text{ kA}$ and a duration similar to the TGF timescale. This mechanism compares favorably with the QES and EMP TGF production mechanisms described in Section 2.4.1 and 2.4.2 which required either extremely large charge motions or current pulses with $I_0 > 400 \text{ kA}$.

The RREA driven by the electric field surrounding lightning leader channels as shown in Figures 6.6 and 6.7 is emitted in a broad beam and with a spectrum characteristic of RREA and bremsstrahlung as discussed in Section 3.2.1. The RREA growth factors available in such electric fields, together with RREA seed production by lightning leaders is sufficient to produce observable TGFs.

The model thus described therefore provides a picture of TGF production from lightning behavior to photon emission to satellite observation. The mechanism does not provide a complete picture, however. One limitation is the uncertainty in the behavior of the lightning channel. In particular, the effective radius of the lightning channel is a parameter in the current pulse simulation corresponding to the different values of the maximum electric field considered to limit the radius of the line charges in Chapter 5. In reality, this radius varies with time and depends on the history of the current flowing in the channel. This dependence can significantly affect the electric field near the channel and may also affect the behavior of current pulses on the channel. A short review of efforts to study the behavior of the leader channel in detail can be found in Section II of *Rakov and Uman* (1998). Another parameter used in the current pulse simulation is the resistance per unit length of the channel, a parameter that also in principle varies with time and history of the channel. Such nonlinear resistance is easily added to the simulations described above, can affect the speed of current pulse propagation, and may significantly complicate the overall dynamics of the lightning discharge (*De Conti et al.*, 2008). The effects of RREA on the

development of the lightning channel and the behavior of the resulting electric fields is also not treated in the model described above and may be significant, especially if relativistic feedback is important as discussed in Section 5.5.

Chapter 7

Conclusions

This dissertation discusses a new mechanism by which terrestrial gamma-ray flashes (TGFs) might be produced by lightning. The mechanism is arrived at as a result first of studies of the available satellite data (Chapter 3) that indicate TGFs are produced at 15–20 km altitudes, lower than predicted by previous mechanisms. The low production altitude requires a total source energy of 1–10 kJ of energetic photons as produced by bremsstrahlung from a population of 10^{17} electrons. In Chapter 4, studies of the seeds available to initiate RREA give 10^7 as the maximum feasible number of seed particles. The maximum avalanche multiplication factor available to thunderstorms is roughly $\mathcal{M} = 10^6$, thereby producing a maximum of 10^{13} energetic electrons.

The discrepancy between the number of electrons that can be produced by simple RREA of seed particles available in the thunderstorm environment and the number required for TGF production motivates the study of TGF production by lightning in Chapter 5. Results indicate that lightning is indeed capable of TGF production through the action of active negative leaders. Such leaders are capable not only of producing a large population of seed particles but also of driving RREA and acceleration of these seed particles to high energies. This suggests lightning current

pulse-driven TGF production, the LCP TGF production mechanism. This mechanism is developed further in Chapter 6, where a model of lightning current pulses is constructed and used to derive the properties of photon emission and the lightning properties required to produce observable TGFs. The lightning is required to occur in an ambient electric field of at least 50 kV/m and involve current pulses at cloud altitude of magnitude $I_0 \gtrsim 40$ kA and duration ~ 1 ms. The likelihood of such current pulses is uncertain as intra-cloud lightning is not well-understood, but some results indicate the requirements are not unreasonably extreme. The mechanism and model thus put forth provide a reasonably complete picture of TGF production by lightning, though the detailed physics of lightning discharge is not yet included in the model.

7.1 Suggestions for future work

Experimentally, new data not yet analyzed from satellites such as Fermi, AGILE, TARANIS, and ASIM may shed new light on the physics of TGFs. Analysis of such data as described in Chapter 3 can validate or refute the predictions made of TGF emission by lightning in Chapter 5. Better average energy spectra and higher-resolution energy spectra of individual TGFs can further determine the production altitude and initial beaming of TGF photons. Correlations between TGF data and lightning data with accurate timing, lightning geolocation, and lightning parameter determination can provide better information not only on relative position of source and satellite but can also help describe the properties of TGF-producing lightning.

Theoretically, the main uncertainties remaining in the physics of TGFs are the role of relativistic feedback and the effects of RREA on the lightning discharge. Relativistic feedback can also possibly circumvent the limitations on simple avalanche growth and seed particle populations, especially for positive leader channels. As the effects of relativistic feedback in confined electric fields surrounding lightning and in

realistic thunderstorm electric fields has not yet been well studied, examination of relativistic feedback in the context of TGF production could be very useful. A full model of RREA and relativistic feedback, together with the capability to model the effects of RREA and relativistic feedback on the driving electric field, is required to successfully address this issue. Inclusion of a model of lightning electric fields such as the current pulse model described here would allow studies of how RREA and relativistic feedback relate to lightning discharge. Such a self-consistent model of TGFs as may be produced by lightning and thunderstorm electric fields, with or without relativistic feedback, would be quite valuable.

Use of the understanding gained from such studies of TGFs also provides an opportunity to examine the implications of TGFs for atmospheric physics as a whole. If energetic processes such as RREA are commonly associated with lightning as the results of Chapter 5 indicate, the chemical effects could be of great interest. The radiological implications may even be relevant as TGFs and TGF-like emissions have been suggested to provide a significant radiation dose to a sufficiently-unlucky aircraft (*Dwyer et al.*, 2008b).

The lightning current pulse model described here also forms a solid basis for future research. The detailed microphysics of the leader channel can be modeled and included as time- and history-dependent radius and resistance parameters. The formation and decay of the lightning channel with time can also be included by introducing new uncharged leader channel segments or removal of existing inactive channel segments. The resulting full time-dependent lightning model would be more useful for lightning studies than existing time-independent fractal lightning models (e.g., *Krehbiel et al.*, 2008). A full time-dependent lightning model would allow for studies of the development of intra-cloud components of lightning as well as the resulting radio emissions and their effects such as so-called “sferic bursts” (*Marshall et al.*, 2007). Such a complete physically-motivated model and comparison of its

results to observations, for instance with lightning mapping arrays, would further overall understanding of lightning.

Bibliography

- Abraham, J., et al. (2008), Correlation of the highest-energy cosmic rays with the positions of nearby active galactic nuclei, *Astroparticle Phys.*, *29*(3), 188–204, doi: DOI:10.1016/j.astropartphys.2008.01.002.
- Agostinelli, S., et al. (2003), G4—a simulation toolkit, *Nucl. Inst. & Meth.*, *506*(3), 250–303.
- Anthony, P. L., et al. (1997), Bremsstrahlung suppression due to the Landau-Pomeranchuk-Migdal and dielectric effects in a variety of materials, *Phys. Rev. D*, *56*, 1373–1390, doi:10.1103/PhysRevD.56.1373.
- Baba, Y., and V. A. Rakov (2007), Electromagnetic models of the lightning return stroke, *J. Geophys. Res.*, *112*(D11), D04,102, doi:10.1029/2006JD007222.
- Babich, L. P., R. I. Il'kaev, I. M. Kutsyk, K. I. Bakhov, and R. A. Roussel-Dupré (2004a), Self-consistent calculation of upward atmospheric discharge developing in the mode relativistic runaway electron avalanches, *Geomag. Aeron.*, *44*(2), 231–242.
- Babich, L. P., R. I. Il'kaev, I. M. Kutsyk, A. Y. Kudryavtsev, R. A. Roussel-Dupré, and E. M. Symbalisty (2004b), Analysis of atmospheric gamma ray bursts based on the mechanism of generation of relativistic electron avalanches, *Geomag. Aeron.*, *44*(2), 243–251.

- Bell, T. F., V. P. Pasko, and U. S. Inan (1995), Runaway electrons as a source of Red Sprites in the mesosphere, *Geophys. Res. Lett.*, *22*, 2127–2130, doi:10.1029/95GL02239.
- Berger, M., J. Hubbell, S. Seltzer, J. Chang, J. Coursey, R. Sukumar, and D. Zucker (1998), Xcom: Photon cross sections database, *Tech. rep.*, National Institute of Standards and Technology.
- Betz, H., T. C. Marshall, M. Stolzenburg, K. Schmidt, W. P. Oettinger, E. Defer, J. Konarski, P. Laroche, and F. Dombai (2008), Detection of in-cloud lightning with VLF/LF and VHF networks for studies of the initial discharge phase, *Geophys. Res. Lett.*, *35*, 23,802, doi:10.1029/2008GL035820.
- Betz, H., U. Schumann, and P. Laroche (Eds.) (2009), *Lightning: Principles, Instruments and Applications*, Springer Verlag.
- Blair, T. A., and R. C. Fite (1957), *Weather Elements*, Prentice Hall, Englewood Cliffs, NJ.
- Carlson, B. E., N. G. Lehtinen, and U. S. Inan (2007), Constraints on terrestrial gamma ray flash production from satellite observation, *Geophys. Res. Lett.*, *34*, L08,809, doi:10.1029/2006GL029229.
- Carlson, B. E., N. G. Lehtinen, and U. S. Inan (2008), Runaway relativistic electron avalanche seeding in the Earth’s atmosphere, *J. Geophys. Res.*, *113*, A10,307, doi:10.1029/2008JA013210.
- Carlson, B. E., N. G. Lehtinen, and U. S. Inan (2009a), Observations of terrestrial gamma-ray flash electrons, in *COUPLING OF THUNDERSTORMS AND LIGHTNING DISCHARGES TO NEAR-EARTH SPACE: Proceedings of the Workshop*,

- vol. 1118, edited by N. B. Crosby, T.-Y. Huang, and M. J. Rycroft, pp. 84–91, AIP, doi:10.1063/1.3137717.
- Carlson, B. E., N. G. Lehtinen, and U. S. Inan (2009b), Terrestrial gamma-ray flash production by lightning current pulses, *J. Geophys. Res.*, *in press*.
- Carlson, B. E., et al. (2005), Search for correlated high energy cosmic ray events with CHICOS, *J. Phys. G. Nucl. Partic.*, *31*, 409–416, doi:10.1088/0954-3899/31/5/011.
- Christian, H., et al. (1999), The lightning imaging sensor, in *Proceedings of the 11th International Conference on Atmospheric Electricity*, pp. 746–749, NASA.
- Cohen, M. B., U. S. Inan, and G. Fishman (2006), Terrestrial gamma ray flashes observed aboard the Compton Gamma Ray Observatory/Burst and Transient Source Experiment and ELF/VLF radio atmospherics, *J. Geophys. Res.*, *111*, D24,109, doi:10.1029/2005JD006987.
- Cohen, M. B., U. S. Inan, R. K. Said, and D. M. Smith (2007), Terrestrial gamma-ray flashes and very low frequency data, *IUGG General Assembly, Perugia, Italy*.
- Cohen, M. B., U. S. Inan, R. K. Said, and D. M. Smith (2009), Terrestrial gamma-ray flashes and updated very low frequency measurements, manuscript in preparation for Geophysical Research Letters.
- Coleman, L. M., and J. R. Dwyer (2006), Propagation speed of runaway electron avalanches, *Geophys. Res. Lett.*, *33*, L11,810, doi:10.1029/2006GL025863.
- Cooray, V. (2004), *The lightning flash*, Institution of Electrical Engineers, London.
- Cummer, S. A., and U. S. Inan (2000), Modeling ELF radio atmospheric propagation and extracting lightning currents from ELF observations, *Radio Sci.*, *35*, 385–394, doi:10.1029/1999RS002184.

- Cummer, S. A., and W. A. Lyons (2004), Lightning charge moment changes in U.S. High Plains thunderstorms, *Geophys. Res. Lett.*, *31*, 5114, doi:10.1029/2003GL019043.
- Cummer, S. A., Y. Zhai, W. Hu, D. M. Smith, L. I. Lopez, and M. A. Stanley (2005), Measurements and implications of the relationship between lightning and terrestrial gamma ray flashes, *Geophys. Res. Lett.*, *32*, L08,811, doi:10.1029/2005GL022778.
- De Conti, A., S. Visacro, N. Theethayi, and V. Cooray (2008), A comparison of different approaches to simulate a nonlinear channel resistance in lightning return stroke models, *J. Geophys. Res.*, *113*(D12), D14,129, doi:10.1029/2007JD009395.
- Dwyer, J. (2003), A fundamental limit on electric fields in air, *Geophys. Res. Lett.*, *30*(20), 2055.
- Dwyer, J., Z. Saleh, H. Rassoul, D. Concha, M. Rahman, V. Cooray, J. Jerauld, M. Uman, and V. Rakov (2008), A study of X-ray emission from laboratory sparks in air at atmospheric pressure, *J. Geophys. Res.*, *113*, D23,207.
- Dwyer, J., et al. (2003), Energetic radiation produced during rocket-triggered lightning, *Science*, *299*(5607), 694–697.
- Dwyer, J. R. (2007), Relativistic breakdown in planetary atmospheres, *Phys. Plasmas*, *14*(4), 042,901, doi:10.1063/1.2709652.
- Dwyer, J. R. (2009), Relativistic positron/x-ray feedback and thundercloud electric fields, *AGU Chapman Conference on the Effects of Thunderstorms and Lightning in the Upper Atmosphere*.
- Dwyer, J. R., and D. M. Smith (2005), A comparison between Monte Carlo simulations of runaway breakdown and terrestrial gamma-ray flash observations, *Geophys. Res. Lett.*, *32*, L22,804, doi:10.1029/2005GL023848.

- Dwyer, J. R., B. W. Grefenstette, and D. M. Smith (2008a), High-energy electron beams launched into space by thunderstorms, *Geophys. Res. Lett.*, *35*, L02,815, doi:10.1029/2007GL032430.
- Dwyer, J. R., D. M. Smith, B. W. Grefenstette, and B. J. Hazelton (2008b), The high-energy radiation dose received aboard aircraft exposed to a terrestrial gamma-ray flash, *AGU Fall Meeting, San Francisco*.
- Dwyer, J. R., et al. (2004), A ground level gamma-ray burst observed in association with rocket-triggered lightning, *Geophys. Res. Lett.*, *31*, 5119, doi:10.1029/2003GL018771.
- Dwyer, J. R., et al. (2005), X-ray bursts associated with leader steps in cloud-to-ground lightning, *Geophys. Res. Lett.*, *32*, 1803, doi:10.1029/2004GL021782.
- Eack, K. B. (2004), Electrical characteristics of narrow bipolar events, *Geophys. Res. Lett.*, *31*, 20,102, doi:10.1029/2004GL021117.
- Eidelman, S., et al. (2004), Review of Particle Physics, *Phys. Lett. B*, *592*, 1–1109, doi:10.1016/j.physletb.2004.06.001.
- Fishman, G. J., and C. A. Meegan (1995), Gamma-Ray Bursts, *Ann. Rev. Astron. Astrophys.*, *33*, 415–458, doi:10.1146/annurev.aa.33.090195.002215.
- Fishman, G. J., et al. (1994a), The first BATSE gamma-ray burst catalog, *Astrophys. J. Suppl.*, *92*, 229–283, doi:10.1086/191968.
- Fishman, G. J., et al. (1994b), Discovery of intense gamma-ray flashes of atmospheric origin, *Science*, *264*(5163), 1313–1316.
- Franz, R. C., R. J. Nemzek, and J. R. Winckler (1990), Television Image of a Large Upward Electrical Discharge Above a Thunderstorm System, *Science*, *249*, 48–51.

- Gallimberti, I., G. Bacchiega, A. Bondiou-Clergerie, and P. Lalande (2002), Fundamental processes in long air gap discharges, *Comptes Rendus Physique*, *3*(10), 1335–1359.
- Goldstein, H., C. Poole, and J. Safko (2002), *Classical Mechanics*, Addison Wesley.
- Grefenstette, B. W., D. M. Smith, J. R. Dwyer, and G. J. Fishman (2008), Time evolution of terrestrial gamma ray flashes, *Geophys. Res. Lett.*, *35*, L06,802, doi:10.1029/2007GL032922.
- Gurevich, A., K. Zybin, and Y. Medvedev (2007), Runaway breakdown in strong electric field as a source of terrestrial gamma flashes and gamma bursts in lightning leader steps, *Phys. Lett. A*, *361*(1-2), 119–125.
- Gurevich, A. V., and K. P. Zybin (2004), High energy cosmic ray particles and the most powerful discharges in thunderstorm atmosphere, *Phys. Lett. A*, *329*, 341–347, doi:10.1016/j.physleta.2004.06.094.
- Gurevich, A. V., G. M. Milikh, and R. A. Roussel-Dupré (1992), Runaway mechanism of air breakdown and preconditioning during a thunderstorm, *Phys. Lett. A*, *165*, 463–468, doi:10.1016/0375-9601(92)90348-P.
- Gurevich, A. V., R. Roussel-Dupré, and K. P. Zybin (1998), Kinetic equation for high energy electrons in gases, *Phys. Lett. A*, *237*(4–5), 240–246, doi:10.1016/S0375-9601(97)00868-2.
- Gurevich, A. V., L. M. Duncan, Y. V. Medvedev, and K. P. Zybin (2002), Radio emission due to simultaneous effect of runaway breakdown and extensive atmospheric showers, *Phys. Lett. A*, *301*, 320–326, doi:10.1016/S0375-9601(02)00900-3.

- Gurevich, A. V., L. M. Duncan, A. N. Karashtin, and K. P. Zybin (2003), Radio emission of lightning initiation, *Phys. Lett. A*, *312*, 228–237, doi:10.1016/S0375-9601(03)00511-5.
- Gurevich, A. V., Y. V. Medvedev, and K. P. Zybin (2004), New type discharge generated in thunderclouds by joint action of runaway breakdown and extensive atmospheric shower, *Phys. Lett. A*, *329*, 348–361, doi:10.1016/j.physleta.2004.06.099.
- Gurevich, A. V., Y. V. Medvedev, and K. P. Zybin (2004a), Thermal electrons and electric current generated by runaway breakdown effect [rapid communication], *Phys. Lett. A*, *321*, 179–184, doi:10.1016/j.physleta.2003.10.062.
- Gurevich, A. V., K. P. Zybin, and Y. V. Medvedev (2006), Amplification and nonlinear modification of runaway breakdown, *Phys. Lett. A*, *349*, 331–339, doi:10.1016/j.physleta.2005.09.074.
- Gurevich, A. V., et al. (2004b), Experimental evidence of giant electron-gamma bursts generated by extensive atmospheric showers in thunderclouds, *Phys. Lett. A*, *325*, 389–402, doi:10.1016/j.physleta.2004.03.074.
- Hazelton, B., B. Grefenstette, D. Smith, J. Dwyer, X. Shao, S. Cummer, T. Chronis, E. Lay, and R. Holzworth (2009), Spectral dependence of terrestrial gamma-ray flashes on source distance, *Geophys. Res. Lett.*, *36*(1), L01,108.
- Hedin, A. E. (1991), Extension of the MSIS thermosphere model into the middle and lower atmosphere, *J. Geophys. Res.*, *96*, 1159–1172, doi:10.1029/90JA02125.
- Howard, J., M. A. Uman, J. R. Dwyer, D. Hill, C. Biagi, Z. Saleh, J. Jerauld, and H. K. Rassoul (2008), Co-location of lightning leader x-ray and electric field change sources, *Geophys. Res. Lett.*, *35*, 13,817, doi:10.1029/2008GL034134.

- Inan, U. S., and N. G. Lehtinen (2005), Production of terrestrial gamma-ray flashes by an electromagnetic pulse from a lightning return stroke, *Geophys. Res. Lett.*, *32*, L19,818, doi:10.1029/2005GL023702.
- Inan, U. S., S. C. Reising, G. J. Fishman, and J. M. Horack (1996), On the association of terrestrial gamma-ray bursts with lightning and implication for sprites, *Geophys. Res. Lett.*, *23*(9), 1017–1020, doi:10.1029/96GL00746.
- Inan, U. S., M. B. Cohen, R. Said, D. M. Smith, and L. I. Lopez (2006), Terrestrial Gamma-ray Flashes and Lightning Discharges, *Geophys. Res. Lett.*, *33*, L18,802, doi:doi:10.1029/2006GL027085.
- International Commission on Radiation Units and Measurements (1984), Stopping powers for electrons and positrons, *ICRU Rep.*, *37*.
- Jackson, J. (1999), *Classical Electrodynamics*, John Wiley & Sons.
- Jackson, J. D. (2000), Charge density on thin straight wire, revisited, *Amer. J. Phys.*, *68*, 789–799, doi:10.1119/1.1302908.
- Jackson, J. D. (2002), Charge density on a thin straight wire: The first visit, *Amer. J. Phys.*, *70*, 409–410, doi:10.1119/1.1432973.
- Klebesadel, R. W., I. B. Strong, and R. A. Olson (1973), Observations of Gamma-Ray Bursts of Cosmic Origin, *Astrophys. J. Lett.*, *182*, L85, doi:10.1086/181225.
- Koch, H. W., and J. W. Motz (1959), Bremsstrahlung Cross-Section Formulas and Related Data, *Rev. Mod. Phys.*, *31*, 920–955, doi:10.1103/RevModPhys.31.920.
- Krehbiel, P., J. Rioussset, V. Pasko, R. Thomas, W. Rison, M. Stanley, and H. Edens (2008), Upward electrical discharges from thunderstorms, *Nat. Geosci.*, *1*(4), 233–237.

- Lee, A., E. D. Bloom, and V. Petrosian (2000), Properties of Gamma-Ray Burst Time Profiles Using Pulse Decomposition Analysis, *Astrophys. J. Suppl.*, *131*, 1–19, doi:10.1086/317364.
- Lehtinen, N. G. (2000), Relativistic runaway electrons above thunderstorms, Ph.D. thesis, Leland Stanford Junior University.
- Lehtinen, N. G., M. Walt, U. S. Inan, T. F. Bell, and V. P. Pasko (1996), γ -ray emission produced by a relativistic beam of runaway electrons accelerated by quasi-electrostatic thundercloud fields, *Geophys. Res. Lett.*, *23*(19), 2645–2648, doi:10.1029/96GL02573.
- Lehtinen, N. G., T. F. Bell, V. P. Pasko, and U. S. Inan (1997), A two-dimensional model of runaway electron beams driven by quasi-electrostatic thundercloud fields, *Geophys. Res. Lett.*, *24*, 2639, doi:10.1029/97GL52738.
- Lehtinen, N. G., T. F. Bell, and U. S. Inan (1999), Monte Carlo simulation of runaway MeV electron breakdown with application to red sprites and terrestrial gamma ray flashes, *J. Geophys. Res.*, *104*(A11), 24,699–24,712, doi:10.1029/1999JA900335.
- Lehtinen, N. G., U. S. Inan, and T. F. Bell (2001), Effects of thunderstorm driven runaway electrons in the conjugate hemisphere: Purple sprites and ionization enhancements, *J. Geophys. Res.*, *106*(A12), 28,841–28,856, doi:10.1029/2000JA000160.
- Leo, W. (1994), *Techniques for nuclear and particle physics experiments*, 2 ed., Springer-Verlag, New York.
- MacGorman, D. R., and W. D. Rust (1998), *The Electrical Nature of Storms*, Oxford University Press, New York.
- Marshall, R. A., U. S. Inan, and W. A. Lyons (2007), Very low frequency sferic bursts,

- sprites, and their association with lightning activity, *J. Geophys. Res.*, *112*(D11), 22,105, doi:10.1029/2007JD008857.
- Marshall, T. C., and M. Stolzenburg (2001), Voltages inside and just above thunderstorms, *J. Geophys. Res.*, *106*(D5), 4757–4768, doi:10.1029/2000JD900640.
- Marshall, T. C., M. Stolzenburg, C. R. Maggio, L. M. Coleman, P. R. Krehbiel, T. Hamlin, R. J. Thomas, and W. Rison (2005), Observed electric fields associated with lightning initiation, *Geophys. Res. Lett.*, *32*, 3813, doi:10.1029/2004GL021802.
- Milikh, G., and J. A. Valdivia (1999), Model of gamma ray flashes due to fractal lightning, *Geophys. Res. Lett.*, *26*(4), 525, doi:10.1029/1999GL900001.
- Miller, E. K., A. J. Poggio, and G. J. Burke (1973), An Integro-Differential Equation Technique for the Time-Domain Analysis of Thin Wire Structures. I. The Numerical Method, *J. Comp. Phys.*, *12*, 24, doi:10.1016/0021-9991(73)90167-8.
- Moss, G., V. Pasko, N. Liu, and G. Veronis (2006), Monte Carlo model for analysis of thermal runaway electrons in streamer tips in transient luminous events and streamer zones of lightning leaders, *J. Geophys. Res.*, *111*, A02,307.
- Motz, J. W., H. A. Olsen, and H. W. Koch (1969), Pair Production by Photons, *Rev. Mod. Phys.*, *41*, 581–639, doi:10.1103/RevModPhys.41.581.
- Nagano, M., and A. A. Watson (2000), Observations and implications of the ultrahigh-energy cosmic rays, *Rev. Mod. Phys.*, *72*, 689–732.
- Nemiroff, R. J., J. T. Bonnell, and J. P. Norris (1997), Temporal and spectral characteristics of terrestrial gamma flashes, *J. Geophys. Res.*, *102*(A5), 9659–9666, doi:10.1029/96JA03107.

- Nguyen, C. V., A. P. J. van Deursen, and U. Ebert (2008), Multiple x-ray bursts from long discharges in air, *J. Phys. D. Appl. Phys.*, *41*(23), 234,012, doi:10.1088/0022-3727/41/23/234012.
- Noda, T., and S. Yokoyama (2002), Thin wire representation in finite difference time domain surge simulation, *IEEE Trans. Power Deliver.*, *17*(3), 840–847, doi:10.1109/TPWRD.2002.1022813.
- Pasko, V. P., U. S. Inan, Y. N. Taranenko, and T. F. Bell (1995), Heating, ionization and upward discharges in the mesosphere due to intense quasi-electrostatic thundercloud fields, *Geophys. Res. Lett.*, *22*, 365–368, doi:10.1029/95GL00008.
- Peskin, M., and D. Schroeder (1995), *An introduction to quantum field theory*, Westview press.
- Poggio, A. J., E. K. Miller, and G. J. Burke (1973), An Integro-Differential Equation Technique for the Time-Domain Analysis of Thin-Wire Structures. II. Numerical Results, *J. Comp. Phys.*, *12*, 210, doi:10.1016/S0021-9991(73)80012-9.
- Rahman, M., V. Cooray, N. Ahmad, J. Nyberg, V. Rakov, and S. Sharma (2008), X rays from 80-cm long sparks in air, *Geophys. Res. Lett.*, *35*.
- Raizer, Y. P. (1997), *Gas Discharge Physics*, Springer.
- Rakov, V., and M. Uman (1998), Review and evaluation of lightning return stroke models including some aspects of their application, *IEEE Trans. Electromagn. C.*, *40*(4), 403–426.
- Rakov, V., and M. Uman (2003), *Lightning: Physics and Effects*, Cambridge Univ. Press, Cambridge.
- Rao, S. (1999), *Time domain electromagnetics*, Academic Press.

- Rison, W., R. J. Thomas, P. R. Krehbiel, T. Hamlin, and J. Harlin (1999), A GPS-based three-dimensional lightning mapping system: Initial observations in central New Mexico, *Geophys. Res. Lett.*, *26*, 3573–3576, doi:10.1029/1999GL010856.
- Roussel-Dupré, R. A., A. V. Gurevich, T. Tunnel, and G. M. Milikh (1994), Kinetic theory of runaway breakdown, *Phys. Rev. E*, *49*, 2257–2271, doi:0.1103/PhysRevE.49.2257.
- Ruina, J., L. Alvarez, W. Donn, R. Garwin, R. Giacconi, R. Muller, W. Panofsky, A. Peterson, and F. W. Sarles (1980), Ad hoc panel on the september 22 event, *Tech. rep.*, Office of Science and Technology Policy, available at <http://www.gwu.edu/~nsarchiv/NSAEBB/NSAEBB190/09.pdf>.
- Said, R. (2009), Accurate and efficient long-range lightning geo-location using a vlf radio atmospheric waveform bank, Ph.D. thesis, Leland Stanford Junior University.
- Sciutto, S. J. (2002), *AIRES User's Manual and Reference Guide, version 2.6.0*, available online at <http://www.fisica.unlp.edu.ar/auger/aires/>.
- Smith, D. M. (2006), personal communication.
- Smith, D. M. (2009), personal communication.
- Smith, D. M., L. I. Lopez, R. P. Lin, and C. P. Barrington-Leigh (2005), Terrestrial gamma flashes observed up to 20 MeV, *Science*, *307*(5712), 1085–1088, doi:10.1126/science.1107466.
- Smith, D. M., J. R. Dwyer, B. W. Grefenstette, B. J. Hazelton, Y. Yair, J. Bor, E. H. Lay, and R. H. Holzworth (2007), Unusual RHESSI TGFs: electron beams and others, *AGU Fall Meeting, San Francisco*.

- Smith, P. (1990), Instabilities in time marching methods for scattering: Cause and rectification, *Electromagnetics*, 10(4), 439–451.
- Sokolsky, P. (1989), *Introduction to Ultrahigh Energy Cosmic Ray Physics*, Addison-Wesley, New York.
- Stanley, M. A., X.-M. Shao, D. M. Smith, L. I. Lopez, M. B. Pongratz, J. D. Harlin, M. Stock, and A. Regan (2006), A link between terrestrial gamma-ray flashes and intracloud lightning discharges, *Geophys. Res. Lett.*, 33, L06,803.
- Stolzenburg, M., and T. C. Marshall (2008), Charge Structure and Dynamics in Thunderstorms, *Space Sci. Rev.*, 137, 355–372, doi:10.1007/s11214-008-9338-z.
- Symalisty, E. M. D., R. A. Roussel-Dupré, and V. A. Yukhimuk (1998), Finite volume solution of the relativistic Boltzmann equation for electron avalanche rates, *IEEE Trans. Plasma Sci.*, 26(5), 1575–1582, doi:10.1109/27.736065.
- Thomas, R. J., P. R. Krehbiel, W. Rison, T. Hamlin, J. Harlin, and D. Shown (2001), Observations of VHF source powers radiated by lightning, *Geophys. Res. Lett.*, 28, 143–146, doi:10.1029/2000GL011464.
- Williams, E., et al. (2006), Lightning flashes conducive to the production and escape of gamma radiation to space, *J. Geophys. Res.*, 111, D16,209.
- Wilson, C. T. R. (1924), The electric field of a thundercloud and some of its effects, *Proc. Roy. Soc. London*, 37, 32D–37D.
- Wolfendale, A. W. (Ed.) (1973), *Cosmic rays at ground level*, Institute of Physics, London.
- Wood, T. G. (2004), Geo-location of individual lightning discharges using impulsive VLF electromagnetic waveforms, Ph.D. thesis, Leland Stanford Junior University.

- Wood, T. G., and U. S. Inan (2002), Long-range tracking of thunderstorms using spheric measurements, *J. Geophys. Res.*, *107*, 4553, doi:10.1029/2001JD002008.
- Yair, Y. (2008), Charge Generation and Separation Processes, *Space Sci. Rev.*, *137*, 119–131, doi:10.1007/s11214-008-9348-x.